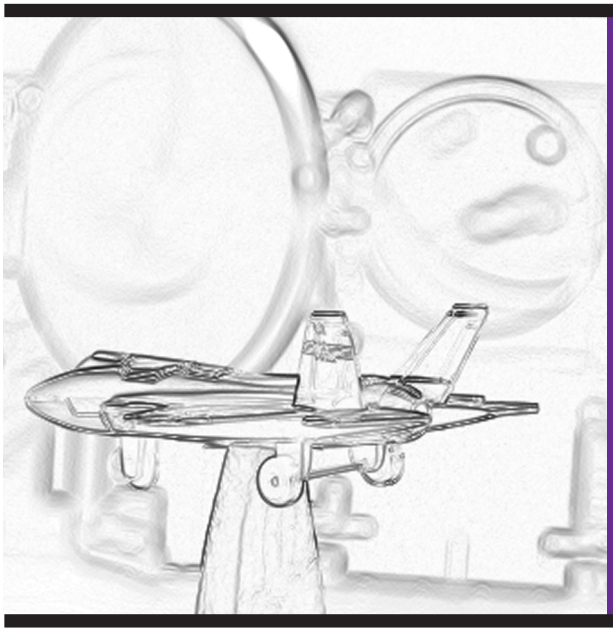

Terahertz Technology for Defense and Security-Related Applications

Krzysztof Iwaszczuk

Ph. D. Thesis

August 2012

DTU Fotonik
Department of Photonics Engineering

Technical University of Denmark

Terahertz Technology for Defense and Security-Related Applications

by

Krzysztof Iwaszczuk

A thesis submitted in partial fulfillment for the degree of Doctor of Philosophy

in the

DTU Fotonik
Department of Photonics Engineering

August 2012

Abstract

This thesis deals with chosen aspects of terahertz (THz) technology that have potential in defense and security-related applications.

A novel method for simultaneous data acquisition in time-resolved THz spectroscopy experiments is developed. This technique is demonstrated by extracting the sheet conductivity of photoexcited charge carriers in semi-insulating gallium arsenide. Comparison with results obtained using a standard data acquisition scheme shows that the new method minimizes errors originating from fluctuations in the laser system output and timing errors in the THz pulse detection. Furthermore, a new organic material, BNA, is proved to be a strong and broadband THz emitter which enables spectroscopy with a bandwidth twice as large as conventional spectroscopy in the field.

To access electric fields allowing exploration of THz nonlinear phenomena, field enhancement properties of tapered parallel plate waveguides are investigated. A new method for imaging of the electric field distribution inside a parallel plate waveguide is developed and used to measure frequency-resolved field reflection coefficients. Field enhancement factors higher than 20 are demonstrated and record-high field strengths of > 1.4 MV/cm are reached. A good agreement between two independent methods of field measurement and a numerical time-domain simulation is shown.

Finally, and extensive study of THz radar cross sections (RCS) of scale models of airplanes is carried out. Angle- and frequency-resolved RCS of aircraft fighters F-16 and F-35 are measured. The scaling law allows for translating THz RCS results to the microwave regime. 2D cross section images of the airplanes are reconstructed. Range resolution of 0.27 mm and cross range resolution of 0.19 mm is reached. Properties of flexible absorbing metamaterials for the THz stealth technology are investigated and significant reduction of the RCS is shown.

Resume

Denne afhandling omhandler udvalgte aspekter af terahertz (THz) teknologi med potentiale i forsvars- og sikkerheds-relaterede applikationer.

En ny metode til samtidig dataopsamling i tidsopløst THz spektroskopi eksperimenter er blevet udviklet. Denne teknik demonstreres ved bestemmelse af fladekonduktiviteten af fotogenererede ladningsbrere i semi-isolerende gallium arsenid. En sammenligning med resultater opnået ved hjælp af en standard dataopsamlingsprocedure viser at den nye metode minimerer fejl stammende fra fluktuationer i laser systemet og timing fejl i THz puls detektionen. Ydermere er det vist at et nyt organisk materiale, BNA, virker som en kraftig og bredbåndet THz kilde, som muliggør spektroskopi med en båndbredde der er dobbelt så stor som i konventionel spektroskopi indenfor dette felt.

For at få adgang til elektriske feltstyrker som tillader udforskning af ikke-linere THz fnomener, undersøges feltforstrkningsegenskaberne for tilspidsede parallel-plade-bølgeledere. En ny metode til visualisering af det elektriske felt inde i en parallel-plade-bølgeleder er udvikles, og anvendes til at måle frekvensopløste feltreflektionskoefficienter. Feltforstrkningsfaktorer større end 20 demonstreres og rekordhøje feltstyrker > 1.4 MV/cm opnaas. En god overensstemmelse findes mellem to uafhængige metoder til bestemmelse af feltstyrke og en numeriske tidsdomne simulation.

Til sidst gennemføres en omfattende undersøgelse af THz radar cross sections (RCS) for modelfly. Vinkel- og frekvens-opløste RCS måles for F-16 og F-35 model jagerfly. Skaleringsloven tillader at THz RCS kan omsttes til mikrobølgeområdet. 2D tværsnitsbilleder rekonstrueres for flyene. En Range-opløsning på 0.27 mm opnås og en cross-range-opløsning på 0.19 mm opnås. Egenskaberne for fleksible absorberende metamaterialer til THz-stealth-teknologi undersøges og en signifikant reduktion af RCS påvises.

Preface

This Ph.D. thesis is the summary of the work conducted during my employment as Ph.D. student at the Technical University of Denmark (DTU) in the period September 2008 until September 2011, under supervision of Professor Peter Uhd Jepsen from DTU and Senior Scientist Henning Heiselberg from Danish Defense Acquisition and Logistics Organization.

Most of the results presented in this thesis are obtained at DTU Fotonik - Department of Photonics Engineering, Technical University of Denmark. During the 3 year-long Ph.D. project I spent 4.5 months at the external stay at the Rensselear Polytechnic Institute (RPI) in Troy, USA, where I visited Prof. Xi-Cheng Zhang. All the experimental results presented in the chapter 4 were obtained in the laboratories in the Center for THz Research at RPI. Numerical simulations from that chapter were performed by Andrei Andryieuski from DTU Fotonik.

The near-perfect metamaterial absorbers, investigated in the chapter 5, were designed and manufactured at Boston University by Xin Zhang, Kebin Fan, Andrew C. Strikwerda and Prof. Richard D. Averitt.

This Ph.D. project was partially financed by DTU Fotonik, Technical University of Denmark (1/3), Forsvarets Materieltjeneste - Danish Defense Acquisition and Logistics Organization (1/3) and Photonics Academy Denmark (1/3). My external scientific stay at the Rensselear Polytechnic Institute received external financial support from Idella Foundation. Expenses connected to travels for international conferences were co-financed by Otto Mønsted Fond.

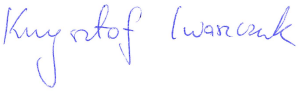

Krzysztof Iwaszczuk
Kgs. Lyngby, September 14th, 2011

Contents

List of Figures

Chapter 1

Introduction

1.1 Brief introduction to THz

Terahertz (THz) waves, or submillimeter/far-infrared waves (sometimes also called T-rays), refer to electromagnetic radiation in the frequency range from 0.1 to 30 THz. This part of the spectrum is situated between microwaves on the long waves side, and infrared on the short wave edge of its range, as shown in Fig. 1.1. The boundaries between spectrum ranges are not strictly defined, and highly depend on such aspects as generation and detection methods. The THz frequency range lays on the borderline of electronic world, where radio and microwave radiation is easily generated using electron based devices, and photonic world, where optical techniques are successfully applicable. Unfortunately the efficiency of the electronic devices rapidly decreases in the THz range, and also optical methods are inefficient. Due to its inaccessibility for many years the THz frequency range used to be referred as a 'THz gap'. Development in THz generation and detection methods over the past 25 years makes term 'THz gap' inadequate. Especially THz time-domain spectroscopy is already well established scientific technique, capable of

providing information about investigated objects unobtainable by other methods [1, 2].

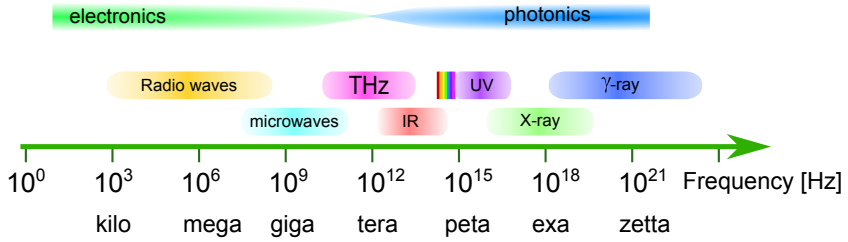

FIGURE 1.1: The electromagnetic spectrum. The terahertz region is situated between microwaves and infrared (IR). The visible part of the spectrum is shown between the infrared and ultraviolet (UV) regions.

Terahertz technology is an extremely active field of science with the number of publications increasing rapidly. Fig. 1.2 shows result of the search on Web of Science for journal articles with 'terahertz' or 'THz' in the title. In the last 20 years the number of publications in this field has increased nearly by a factor of 100 and judging by the exponential growth it is going to continue increasing for at least next couple of years.

This high interest in the THz science has its origins in unique properties of the THz radiation. The frequency of 1 THz corresponds to one trillion oscillation per second, or one oscillation per picosecond. In the equivalent units 1 THz is:

$$1 \text{ THz} \equiv 300\mu\text{m} \equiv 4.14 \text{ meV} \equiv 33.3 \text{ cm}^{-1} \equiv 47.6 \text{ K}.$$

THz waves have low photon energies (4.14 meV for 1 THz, which is 1 million times weaker than X-ray) and do not cause harmful photoinoization in biological tissues [3, 4]. For that reason THz radiation is considered completely safe for potential sensing and imaging techniques. THz waves can penetrate through many optically opaque nonpolar dielectrics, such

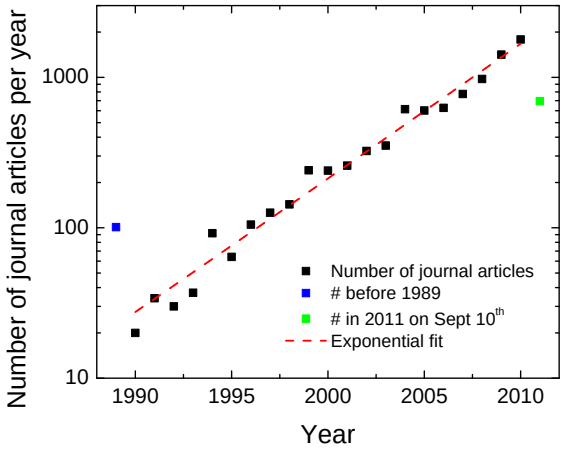

FIGURE 1.2: Number of journal publications per year in the THz field. Data obtained as a search result on Web of Science for 'terahertz' or 'THz' in the publication title.

as paper, textile, plastic or ceramic with low attenuation. The THz frequency range hosts low frequency crystalline lattice vibrations - phonon modes, hydrogen-bonding stretches and other intermolecular vibrations and rotational transitions of molecules in many chemical and biological materials, including many explosives and drugs. The wealth of unique spectroscopic signatures in the THz energy range for all states of matter (gasses, liquids, solid-state and even plasma), makes THz ideal for spectroscopic purposes. Because of its spectroscopic properties combined with ability to image under covers or containers and non-ionising photon energies, THz waves are considered highly competitive for non-destructive and noninvasive sensing.

The electromagnetic radiation at THz frequencies interacts strongly with systems that have characteristic lifetimes in the picosecond range and energy transitions in the meV range. To the long list of such systems one can account bound electrical charges [5], free charge plasma [6], excitons [7], phonons [8], molecular crystals [9], and relaxations in liquids [10].

Subpicosecond broadband THz transients are an excellent tool to study dynamics of ultrafast processes in semiconductors [11–14], which understanding is crucial for development of new electronic devices. Except of purely scientific applications of THz technology, numerous practical applications start to emerge. THz techniques have high potential in such opto-electronic areas as industrial control, pharmaceutics, medical diagnostics, security applications, high-speed wireless communication and art conservation [1, 15–17].

There are several milestones that have made THz spectroscopy well established scientific technique. As the first one, Fourier transform infrared (FTIR) spectroscopy developed in 1950's should be mentioned [18, 19]. FTIR combines interferometry and broadband infrared detectors to achieve frequency resolution. Together with implementation of fast Fourier transform (FFT) algorithm and first computers, FTIR became a standard analytical method in the far- and mid-infrared range. The next important development in the THz range started in 1960's with invention of maser and laser, which led to the invention of various THz gas lasers (e.g. CO_2 pumped methanol laser at 2.5 THz [20]).

A major development, which is also based on a fundamentally different approach to the THz spectroscopy, came with the discovery of ultrafast mode-locked lasers. The pioneering work was done in 1970s by D. H. Auston at Bell Laboratories [21], who used photoconductive dipole antennas to generate far-infrared radiation. The first THz time domain spectroscopy setup (THz-TDS) based on optical excitation of photoconductive dipole antennas was developed in 1989 by D. Grischkowsky *et al.* [22]. The development of photoconductive switches was closely connected to the invention of Ti:saphire laser in 1991 [23, 24]. The development of ultrafast laser amplifiers initiated nonlinear THz generation and detection techniques. The difference frequency generation (DFG) between two ruby lasers was fist demonstrated by Faries *et al.* [25], and then DFG from a single laser pulse in lithium niobate $LiNbO_3$ [26], spanning frequency range from 0.05 to 0.5 THz was shown. 1995 brought

free space electro-optic sampling (FEOs), developed by three independent groups [27–29]. Introduction of zinc telluride (ZnTe) [30] solved initial problems with poor phase matching. In the first decade of XXI century THz air photonic generation [31] and detection [32–34], by four wave mixing in laser generated two-color-plasma, was invented. At the same time optical rectification by tilted wavefront excitation of $LiNbO_3$ opened doors for studying THz nonlinear phenomena using table top systems [35, 36].

So far THz systems rarely leave laboratories, even though there are already few companies that offer commercial THz devices. Several factors strongly restrict popularity of THz systems. Probably the most important is a low speed of acquiring data. At current fastest THz systems can obtain up to few hundred of THz waveforms per second. That number is already sufficient for a single point measurements, but is at least two orders of magnitude too low for application in the serial large scale industrial or security imaging. Next restriction is the high cost of THz systems, which mainly comes from the high price of femtosecond laser, used for THz generation and detection. Other obstacles for THz technology come from the big size of THz systems, their poor insensitivity for changing working conditions and short propagation length of THz radiation in the atmospheric air due to water vapor absorption [37]. Several techniques have potential to overcome some of the described problems. For example asynchronous optical sampling (ASOPS) developed by Yasui *et al.* [38] and Janke *et al.* [39] has a chance to speed up acquisition rate, while multimode semiconductor laser diodes (MMSLDs) [40] combined with THz quasi time domain spectroscopy [41] can reduce prices of THz systems.

Stand-off detection of explosives is highly desirable for security purposes. The transmitted and reflected THz spectra of most explosives and related compounds contain unique THz absorption fingerprints characterizing crystalline lattice vibrational modes [42, 43]. Due to its ability to penetrate many optically opaque materials [44], THz technology offers potentially best solution in detecting explosives and related compounds

(ERCs). But the task is so complex and difficult that so far there is none commercial system in use in real life situation, as for example security scanning at airports. The list of issues that has to be addressed before such system will be built is long. It is enough just to mention: low speed of obtaining spectra, short range of detection, influence of surface quality of a real-life explosive and influence of the package material. It also seems that building a library of the THz absorption spectra of different ERCs is a step needed before THz techniques will become popular. In this thesis we have not investigated directly THz properties of explosives nor methods of their detection. Instead we've focused on two other issues: improving the acquisition scheme for time resolved THz spectroscopy and field enhancement by tapered parallel plate waveguides.

THz time-domain spectroscopy is undoubtedly powerful technique, but all the spectra obtained by THz-TDS are static and no information about sample dynamics is present. At the same time subpicosecond THz transients, which are synchronized to optical femtosecond pulse trains, open possibility for studying dynamical properties of picosecond nonequilibrium processes in the THz frequency range. In the first part of this thesis we focus on obtaining more accurate time resolved THz spectroscopy data, which is done by introducing new simultaneous reference and differential waveform acquisition. It is shown that the application of the new method minimizes errors in spectrally resolved photoconductivity originating in laser instabilities and pulse timing jitter. In recent years high power-table top THz sources became available [36]. THz electric fields with amplitude over 1 MV/cm will allow for investigation of yet poorly-understood anharmonic interactions between different phonon modes in molecular crystals including explosives and related compounds. Nonlinear interactions and energetic coupling between lattice vibrations will not only open a new big block of fundamental science, but will also provide additional information about the investigated sample and its environment. In this perspective new simultaneous reference and differential waveform acquisition method presented in this thesis is

a step towards time-resolved high field THz-pump THz-probe interactions and particularly THz 2D spectroscopy [45]. To access the range of nonlinear THz interactions, THz electric fields exceeding 1 MV/cm are needed. In this thesis we investigate properties of tapered parallel plate for enhancing THz field strength to reach required levels. For that purpose we developed a novel non-invasive broadband method of imaging the THz electric field inside parallel plate waveguide. We experimentally demonstrate field enhancement factors over 20 and peak electric fields exceeding 1.4 MV/cm. Measured values agree well with numerical time domain simulations.

In the last part of this thesis we consider another topic, highly relevant for defence applications, namely the measurement of the radar cross section (RCS). RCS measurements is a standard technique, particularly important for military purposes, including detection and identification of aircrafts, ships and other targets. In case of large size massive objects, such as full-size airplanes or ships, RCS measurements are complicated, time consuming, and expensive. In this analysis we apply the scaling law and basing on values measured in the low THz range (0.1-2 THz) we obtain values that would be measured at typical radar frequencies. Scaling factor between THz waves and radar microwaves results in sizes of scale models on the order of centimeters, which are easy to manufacture by a rapid prototyping systems such as computer numerically controlled 3D milling machines or a 3D printers. Furthermore, we investigate properties of flexible metamaterials for reduction of RCS and potential use in THz stealth measurements.

1.2 Organization of thesis

This thesis is organized as follows:

Chapter 2 starts with basic description of the ultrafast laser amplifier systems that have been used while performing experiments reported in

this thesis. Next a brief review of THz generation techniques is presented with emphasis on optical rectification in nonlinear organic crystal BNA and the generation of milijoule terahertz pulses by tilted-pulse-front excitation in $LiNbO_3$. The following part gives a short summary of different methods of detecting THz radiation. The free-space electro-optic sampling is discussed in detail.

In chapter 3 we describe THz time domain spectroscopy techniques. Basic concepts in time resolved THz spectroscopy are presented. Drude model of conductivity is introduced, which is the most simple but also best understood model of conductivity in semiconductor sample. As a next part of the chapter we present in detail experimental setup for simultaneous reference and differential waveform acquisition in time-resolved terahertz spectroscopy. Subsequently setup calibration methods are described. The chapter ends with results obtained for GaAs sample, which is chosen as a test sample.

Chapter 4 begins with a short review of existing structures for guiding THz waves. Particular attention is placed upon parallel plate waveguide and its properties for dispersionless propagation of TEM mode. Next we discuss air biased coherent detection of THz radiation and give a detailed presentation of the experimental setup for non-invasive method for characterization of the propagating electric field inside a tapered parallel-plate waveguide. Frequency resolved reflection coefficients for the waveguide tip are extracted. Field enhancement properties of a TP-PWG are discussed. Analytical and numerical approaches are compared and based on differences diffraction losses are estimated. We show that THz electric fields exceeding 1.4 MV/cm with 20 μm waveguide output gap are possible to be achieved. Results are verified using two different methods and agree well with numerical predictions.

Chapter 5 deals with terahertz radar cross section measurements. Chapter starts with an introduction to radar techniques. A definition of radar cross section is given and scattering properties of simple scatterers like conducting sphere, cylinder and plate are discussed. Thereafter a short

review of terahertz computed tomography is given. Following we present in detail the experimental setup that was used for performing radar cross section measurements with a setup calibration discussion. Next we present polar and azimuthal time- and frequency resolved RCS plots of F-16 and F-35 fighter aircraft models rotated on a pedestal. The time domain sub-ps resolution allows for sub-mm range resolution and also allows for identification of scattering points. The shape of the models and positions of scattering parts are retrieved by the filtered back projection algorithm.

In chapter 6 a summary of the work presented in this thesis is given. Conclusions are drawn and the outlook for future is presented.

Chapter 2

Terahertz pulses

This chapter starts with a basic description of the laser systems that have been used to obtain experimental results presented in this thesis. Thereafter different sources of THz radiation are discussed, with particular attention to optical rectification in nonlinear organic crystal BNA and generation of high-power terahertz pulses by tilted-pulse-front excitation in $LiNbO_3$. Such interesting phenomena as a strong redshift of near-infrared spectrum transmitted through BNA or saturation of efficiency of generation in $LiNbO_3$ are reported. Different methods of detecting THz radiation are also presented, with focus on free-space electro-optic sampling, which has been used intensively through out this thesis.

2.1 Laser system

The work presented in this thesis would not have been possible if not for the development of ultrafast laser systems and particulary high power ultrafast laser amplifiers. Experiments performed in this thesis have been done using two regenerative laser amplifier systems: Spectra-Physics

Spitfire and Hurricane also from Spectra-Physics. The first one will be described in more detail below. A regenerative amplifier is a device which is used for strong amplification of optical pulses, where multiple passes through the gain medium are achieved by placing the gain medium in an optical resonator [46]. An optical switch, in most cases realized as an electro-optic modulator and a polarizer, is used to control the number of round trips in the resonator. Number of passes through the gain medium can be very high, which results in a very high gain (several tens of decibels). The achieved optical peak intensities can become very high, so to avoid nonlinear pulse distortion and even destruction of the gain medium, chirped-pulse amplification (CPA) [47] has become a standard technique. In CPA a femtosecond-long pulse from the oscillator is chirped and temporally stretched to a much longer duration by the use of a grating pair (stretchers based on a long fibers and prisms are also used) before passing through the amplifier medium. This reduces the peak power to a level where the unwanted phenomena are avoided. After the gain medium, a dispersive compressor (typically a grating pair) removes the chirp and temporally compresses the pulses to a duration comparable to the input pulse duration. CPA has allowed for the construction of table-top amplifiers, which can generate pulses with mJ energies and femtosecond durations, leading to terawatt peak powers.

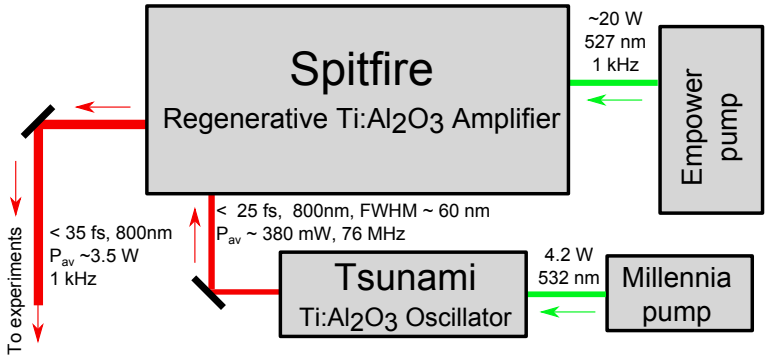

FIGURE 2.1: Ultrafast amplifier laser system in the DTU TERAWATT LAB.

Spectra-Physics Spitfire laser system, presented in the Fig. 2.1, combines four essential parts: "Millennia Pro" pump, "Tsunami" Ti:sapphire oscillator, "Empower" pump and "Spitfire" regenerative Ti:sapphire amplifier. Millennia Pro is a high-power CW green diode-pumped solid state laser working at 1064 nm. The Millenia itself is pumped by two 808 nm diode lasers located in the power supplier. Lasing at 1064 nm is achieved in a neodymium yttrium vanadate (Nd:YVO_4) crystal. The 4.2 W output beam at 532nm from Millenia pro is generated by frequency doubling in nonlinear crystal Lithium triborate (LBO) and is used to pump Ti:sapphire crystal in the Tsunami oscillator laser [24]. Tsunami delivers sub-25 fs pulses at the central wavelength of 800 nm. The central wavelength and the spectral bandwidth are adjusted by a use of a slit-prism pair. For optimal operation a bandwidth of 60 nm in FWHM is used (depicted in the Fig. 2.2(a)). Tsunami delivers pulses at a repetition rate of 76 MHz with average power of 380 mW. This ultrafast oscillator is used as a seed for Spitfire regenerative Ti:saphire amplifier. The Ti:Al_2O_3 crystal in Spitfire is pumped using Empower pump, which is a Q-switched Neodymium-doped yttrium lithium fluoride (Nd:YLF) laser. The output wavelength of 527 nm is achieved by frequency doubling in nonlinear LBO crystal of 1053 nm light from a Nd:YLF solid state laser, which is pumped by a series of 808 nm diode lasers. Strong ns-long pulses are generated by Q-switching [48], giving average optical powers up to 20W at the repetition rate of 1kHz. In the Spitfire incoming ~ 5 nJ femtosecond pulses from Tsunami are first stretched up to ns duration, then amplified to 3.8 mJ energy and in the end compressed to sub 35 fs duration. A very high pulse energy of 3.5 mJ combined with sub 35 fs pulse duration results in ultra high peak power intensity of approximately 100 GW (what is already considered as a terawatt range). Figure 2.2(a) shows a typical spectrum of pulses from Spitfire. The 34nm-in-FWHM-broad spectrum translated into an ultra short pulses in time domain. Fig. 2.2(b) shows autocorrelation of Spitfire laser pulse measured using Spectra-Physics PulseScout autocorrelator. Autocorrelation is a standard technique for measuring temporal duration of short laser pulses [49, 50]. In the autocorrelator

incident pulses are split into two equal portions. One of the pulses is sent to a variable delay and then mixed in a non-collinear configuration with the other pulse in a nonlinear crystal. By changing time delay between pulses the intensity of generated second harmonic can be mapped out. Basing on the width of the autocorrelation, temporal duration of the pulse itself can be calculated. Assuming that the incoming pulse has a Gaussian shape, 60.5 fs in FWHM of autocorrelation corresponds to 43 fs-long pulse (factor of 1.414 [51]).

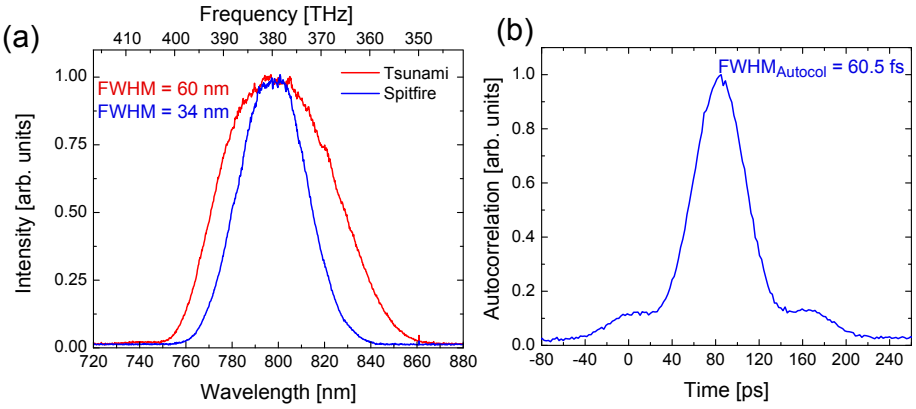

FIGURE 2.2: (a) Output spectra from Tsunami and Spitfire. (b) Autocorrelation of the generated 3.5 mJ laser pulse. Large pedestal is an indication of a significant third and forth order phase dispersion.

2.2 Generation of terahertz radiation

Various ways of generating THz radiation have been developed through the years. One could risk a statement by saying that everything can be used to generate THz waves (probably one of the most surprising processes that lead to THz emission is peeling adhesive tape [52]).

Historically, the oldest sources of THz radiation are thermal sources. Invention of maser and laser in 1960's brought important development for THz generation. Namely powerful CO_2 lasers were used for pumping

THz molecular lasers, which for THz emission were using transitions between different rotational energy levels. CO_2 pumped methanol laser, which gives emission at 119 μm is still in use in some laboratories [20, 53]. The main disadvantage of those THz emitters is that the THz detection is based on the detection of the intensity instead of direct electric field, which will be discussed in the chapter 3.1. More recent development in continuous wave THz sources are the quantum cascade lasers (QCLs) [54]. From the microwave side of spectrum THz radiation can be generated using backward-wave oscillators (BWO), gyrotrons and sum-frequency mixed Schottky [55] and Gunn [56] diodes. The main problem with sources based on the electronic approach is that their efficiency quickly rolls off with increasing frequency.

Free electron laser (FEL) with energy-recovering linear accelerators is the most powerful source in the THz range [57, 58] and until recently it was the only one that was able to generate terahertz pulses that have at least 1 μJ of energy. Free-electron lasers as the lasing medium use relativistic electron beam, which propagates through spatially varying magnetic field [59]. The magnetic field causes the electrons to oscillate and emit photons, whose wavelength can be tuned from microwave to X-ray area by adjusting the energy of the electron beam or the magnetic field strength. Extremely high costs and big sizes of FELs facilities severely restrict their application.

If all the THz systems were counted, photoconductive switches would probably emerge as the most popular type. THz generation by optical excitation of photoconductive dipole antennas was pioneered in 1970s by D. H. Auston [21] and further developed in the 1980s [60–62]. In a semiconductor material of a photoconductive switch, photons from a femtosecond laser pulse with sufficiently high energy can excite electrons into the conduction band. The metallic electrodes supply external bias electric field to the semiconductor in the photoconductive gap between electrodes. Bias field accelerates generated free carriers, creating microscopic current transient. Due to different channels of recombination, free carriers finally recombine, causing currents to vanish. In this

way current impulses, lasting on the order of few hundred femtoseconds, are generated. Dynamics of those ultrashort transient currents is a source of the THz radiation. The short carrier lifetime ($\sim$ 100 fs) of the emitter semiconductor material is beneficial for the high bandwidth of generated radiation. For that reason materials with high number of recombination centers and a fast capture time, as radiation-damaged silicon-on-sapphire [63], low-temperature grown GaAs [64, 65] or ion-implanted InGaAs [66, 67] can be used.

2.2.1 Optical rectification

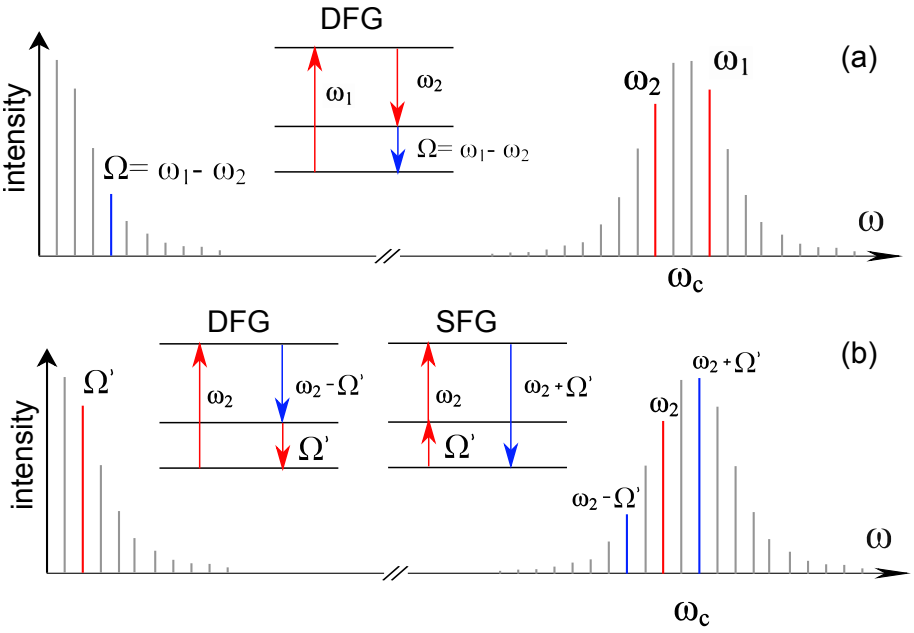

FIGURE 2.3: Photon picture of (a) difference-frequency generation (DFG) of THz frequencies and (b) DFG and sum-frequency generation (SFG) of sidebands to the pump frequencies.

One of frequently used table-top methods of generating relatively high-power THz sources is optical rectification (OR) in nonlinear materials

[68]. Below we will present it in more detail on example of N-benzyl-2-methyl-4-nitroaniline (BNA) crystal. Optical rectification is a difference frequency mixing process and occurs in media with large second order susceptibility χ^2. For ultrashort laser pulses (typically fs pulses from Ti:sapphire laser) that have large bandwidth, as shown in Fig. 2.2(a), the frequency components are differentiated with each other to produce bandwidth from ideally 0 to several THz. The photon picture of the difference-frequency generation (DFG) is shown in the Fig. 2.3(a). A femtosecond laser pulse with a spectrum centered at ω_c contains a comb of frequencies, spaced by $\Delta\omega$ due to the constant repetition rate of the laser. Two NIR photons ω_1 and ω_2 ($\omega_2 < \omega_1$) interact with each other in the nonlinear crystal. As the result photon ω_1 is annihilated and two new photons are created: second ω_2 and a new Ω with energy $\hbar(\omega_1 - \omega_2)$. Frequency of the Ω photon lays in the THz range. Due to the interaction the spectrum on the NIR pump beam shifts in the direction of longer wavelength (so called redshift). When the population of THz photons gets big enough, a different DFG process can take also place - Fig. 2.3(b). This time one NIR photon ω_2 interacts with the THz photon Ω'. As a result ω_2 is annihilated and its energy is used for creation of a second Ω' photon and a NIR photon of energy $\hbar(\omega_2 - \Omega')$. This process also leads to the increase of THz energy and a redshift of NIR pump. An opposite process called sum frequency generation (SFG) can also take place, in which energy is transferred from THz wave to the NIR pulse.

The efficiency of described processes of DFG and SFG is govern by several factors. The most important one is the value of the second order susceptibility χ^2. Phase matching between the optical and terahertz beams also plays a crucial role for efficient optical rectification. Collinear matching between group velocity and the terahertz phase velocity in such crystals as ZnTe and GaP is achievable for pump wavelengths of around 800nm and 1μm, respectively. Energies of up to 1.5μJ in single-cycle terahertz pulses have been obtained from large aperture ZnTe crystal [69].

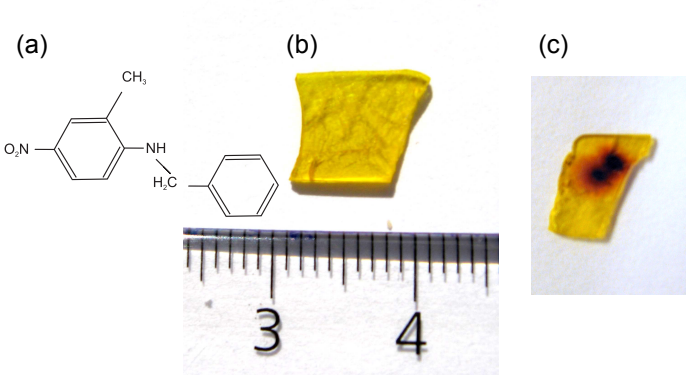

FIGURE 2.4: (a) Molecular formula of BNA crystal. (b) Photo of freshly cleaved BNA 1.3 mm-thick (010) crystal (c) BNA crystal with visible signs of optical degradation due to 800-nm pump irradiation.

Recently, strong interest is placed upon new organic nonlinear crystals (NLO), such as 4-dimethyl-mino-N-methyl-4-stilbazolium tosylate (DAST) [70], 2-methyl-4-nitroaniline (MNA) [71], 2-(α-methylbenzyl-amino)-5-nitropyridine (MBANP) [72] and N-benzyl-2- methyl-4 -nitroaniline (BNA) [73, 74]. Those crystals posses very high second order nonlinearities with lower dielectric constants, than their inorganic counterparts. Except for high nonlinearities, NLO are required to have sufficient size to be subjected to mechanical processing, such as cutting and polishing. Those two characteristics are in opposition: large optical nonlinearities can be easily achieved in a lower-symetry structures, which usually result in small and fragile crystals. On other hand centrosymmetric structure is energetically more stable, and organic molecules are likely to condense in that structures. BNA crystal, which molecular formula is shown in Fig. 2.4(a), was developed to overcome these difficulties. Large BNA crystals, shown in Fig. 2.4(b), were grown with a vertical Bridgman method. The second order nonlinear coefficients of BNA (d_{333} = 234 pm/V and d_{322} = 16 pm/V [75, 76]) are high and allow for more efficient THz generation than the most commonly used ZnTe. The values of the refractive indices of BNA allow for generation of THz radiation in the collinear phase matching configuration for pump wavelength of

around 800nm [77, 78]. BNA exhibits a linear dependence (Fig. 2.5(a)) of generated electric field versus pump power up to the point when signs of damage are apparent at a fluence of ~ 1 mJ/cm^2 (Fig. 2.4(c)). BNA has a orthorhombic lattice structure, space group symmetry $Pna2_1$ and point symmetry *mm2*. Because second order nonlinearity d is a tensor, related to the crystallographical symmetry of BNA crystal, the crystal must be oriented correctly to the laboratory reference frame to maximize THz conversion efficiency. Figure 2.5(b) shows the dependence of the generated THz field on the BNA crystal angle orientation, which is measured in the setup presented in the Fig. 2.5(c). Electric field components parallel and perpendicular to the generation beam polarization are detected. Pair $\lambda/2$-polarizer changes polarization of the pump beam between parallel and perpendicular with respect to the direction of THz detection. The lines in the Fig. 2.5(b) are a best fit to theoretically predicted dependencies $E_{THz} \propto \cos^3 x$ for the parallel and $E_{THz} \propto \cos x \sin^2 x$ for the perpendicular field components.

THz generation in BNA is so efficient that a clear redshift of the pump beam due to the energy transfer to the THz beam is visible. Figure 2.6 shows pump beam spectra at (a) 2 μJ and (b) 130 μJ excitation level for two different polarizations of incoming pump beam with respect to the BNA crystallographical orientation. For the first orientation, the pump beam is polarized in the direction that gives minimal THz emission, while the second orientation is optimal for THz emission. At a low pump fluence both spectra look identical. For the 130 μJ excitation energy, the mean optical wavelength shifts by 2.6 nm in the direction of long waves. Based on the redshift it is calculated that the energy conversion efficiency is $3.3 \cdot 10^{-3}$. Unfortunately, part of the generated THz radiation gets reabsorbed by the BNA before it couples out from the crystal, which has a high absorption coefficient of nearly 70 cm^{-1} at 1 THz [74]. Including also reflections in the crystal, we can calculate energy of freely propagating THz pulses to be 44 nJ.

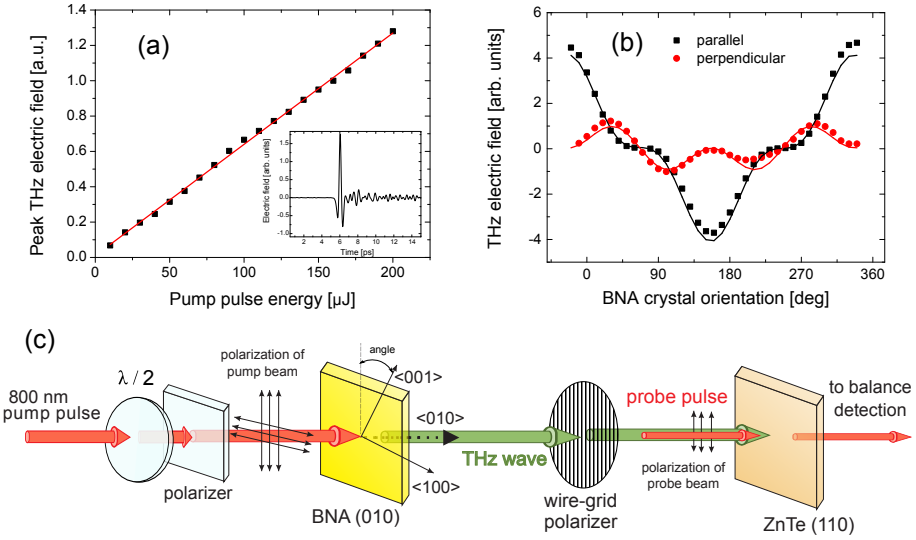

FIGURE 2.5: (a) The peak of THz electric field as a function of NIR pump power. The inset shows the time waveform of the generated THz electric field.(b)Detected parallel and perpendicular THz electric field components as a function of the azimuthal angle of the 1.3 mm BNA source crystal. The lines are a fit to $E_{THz} \propto \cos^3 x$ for the parallel and $E_{THz} \propto \cos x \sin^2 x$ for the perpendicular field components.(c) Simplified schematic of BNA orientation used to obtain the angle dependent data. Pair $\lambda/2$-polarizer changes polarization of the pump beam between parallel and perpendicular with respect to the direction of THz detection.

2.2.2 Generation of high-power terahertz pulses by tilted-pulse-front excitation

As it has been mentioned before, the efficiency of the THz generation in optical rectification critically depends on matching between the group velocity v^{gr}_{NIR} of the ultrashort light pulse and the phase velocity v^{ph}_{THz} of the THz radiation. Velocity matching is obtained if the condition

$$v^{gr}_{\mathrm{NIR}} = v^{ph}_{\mathrm{THz}} \tag{2.1}$$

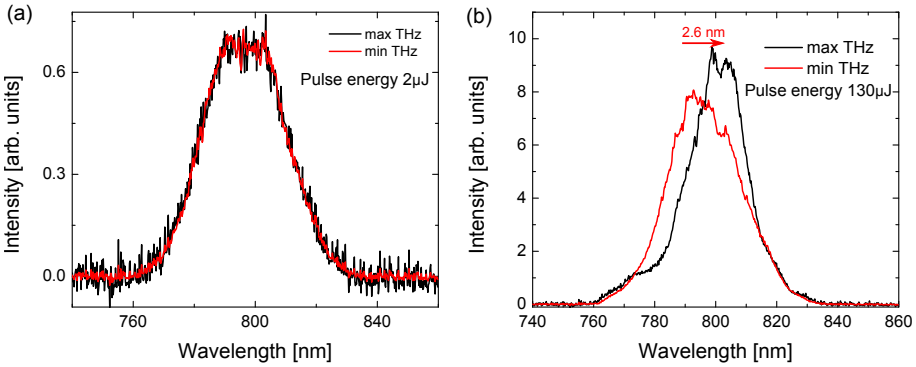

FIGURE 2.6: Redshift in BNA. Spectra of NIR probe transmitted through BNA crystal for (a) 2 μJ (b) 130 μJ incident 800 nm pump pulses. Pair $\lambda/2$-polarizer is used to change energy of the incident pump beam and to switch between polarizations of the pump beam, that give highest and lowest THz generation. The mean value of the wavelength shifts by 2.6 nm into red.

is fulfilled. For such materials as ZnTe, GaP, DAST or BNA, velocity matching of the terahertz phonon-polariton wave can be achieved in a collinear configuration. The nonlinear coefficients of such materials as ZnTe or GaP are significantly smaller than nonlinear coefficients of nonlinear organic crystals as DAST or BNA. Unfortunately, nonlinear organic crystals have a low damage threshold and optical pumping with very intense laser pulses is not recommended. A solution to this problem is to use high dielectric ferroelectrics such as lithium niobate ($LiNbO_3$) or lithium tantalate ($LiTaO_3$), which have nonlinearities comparable with NLO and can sustain higher pump fluences. Unfortunately for those materials, the difference between group refractive index n^{gr}_{NIR} of the NIR pump and the phase refractive index n^{ph}_{THz} of the THz radiation is big (correspondingly 2.23 and 5.16 for $LiNbO_3$ [79]), which does not allow for efficient THz generation in a collinear configuration. Velocity matching in those materials is possible by tilting the optical pulse front [35, 36, 79, 80]. Proper choice of the tilt angle γ, shown in Fig. 2.7(b), allows to equalize phase velocity of the THz pulse with a projection of the NIR

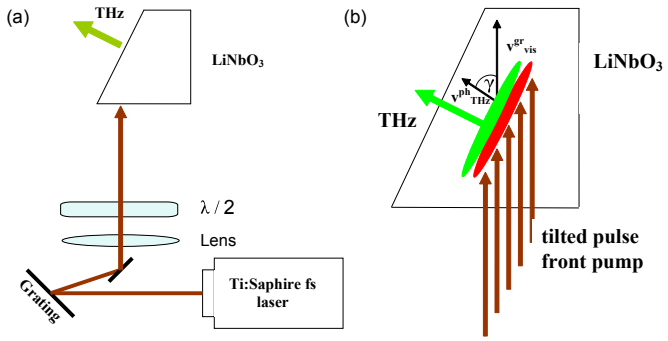

FIGURE 2.7: THz generation in $LiNbO_3$ in a tilted wavefront configuration.

pulse onto the direction of the THz beam according to equation:

$$v_{\mathrm{NIR}}^{gr} \cdot \cos\gamma = v_{\mathrm{THz}}^{ph}. \tag{2.2}$$

For $LiNbO_3$ the tilt angle is $\sim 63°$. Figure 2.7(a) shows a possible experimental setup used for the THz generation by femtosecond laser pulses with tilted pulse fronts. The wavefront of the optical pulse is tilted using diffraction grating and then imaged onto the $LiNbO_3$ surface using a lens [81]. The tilt angle of the NIR pump wavefront in the configuration presented on the figure 2.7(a) is given by:

$$\tan\gamma = \frac{mF\lambda}{n_{\mathrm{NIR}}^{gr} d} \frac{1}{\cos\beta}, \tag{2.3}$$

where F is the imaging demagnification factor, β is the angle of diffracted light, d is a period of the grating and m diffraction order. By combining Eq. 2.3, with a diffraction grating equation:

$$d\,(\sin\alpha + \sin\beta) = m \cdot \lambda, \tag{2.4}$$

where α is the incidence angle onto the grating, the required α and β angles can be calculated. For example: if a 2000 l/mm grating is used, and the demagnification factor $F = 2$, then $\alpha = 66.6°$ and $\beta = 43°$.

Particular tilted wavefront setups used in this thesis, will be discussed in more detail in chapters 5.3 and 4.4. Highest ever reported THz pulse energies obtained using this method were 10μJ and corresponding terahertz electric field at the focus of a parabolic mirror was calculated to be 250kV/cm [80]. In those experiments Ti:sapphire amplifier system delivering 10mJ pulses at a 10Hz repetition rate was used. Figure 2.8(a) shows the energy of the THz pulses generated in $LiNbO_3$ in a tilted wavefront configuration as a function of incident pump pulse energy. Unlike optical rectification in BNA which shows perfect quadratic dependence of the generated THz power vs. excitation pulse power (what corresponds to a linear dependence of the peak electric field and has been presented in the Fig. 2.5(a)), THz generation in $LiNbO_3$ shows linear dependence above saturation threshold. This change from quadratic to linear increase of the generated THz energy has its origins in the free carrier absorption inside $LiNbO_3$ caused by multiphoton absorption at the pump wavelength [82] and results in a saturation of THz generation efficiency, as depicted in Fig. 2.8(b).

It has been theoretically predicted and observed [82] that the shortest pump pulses do not necessarily give highest THz conversion efficiency. High material and angular dispersion inside $LiNbO_3$, makes NIR pulses of 350 fs duration in their time-bandwidth limited form most favorable for high power THz efficiency. Unfortunately, NIR pulses from the Spectra-Physics Spitfire laser system, that has been mostly used in this thesis, are 35 fs long, which yields nearly 8 times lower power conversion efficiency than for 350 fs pulses.

2.3 Detection of terahertz radiation

There are several ways to detect THz radiation. Historically the oldest detection methods are based on thermal effects. THz light is absorbed in the material and lead to the increase of temperature, which can be sensed by such devices as bolometers [83], Golay cells [84] and pyrodetectors[85]

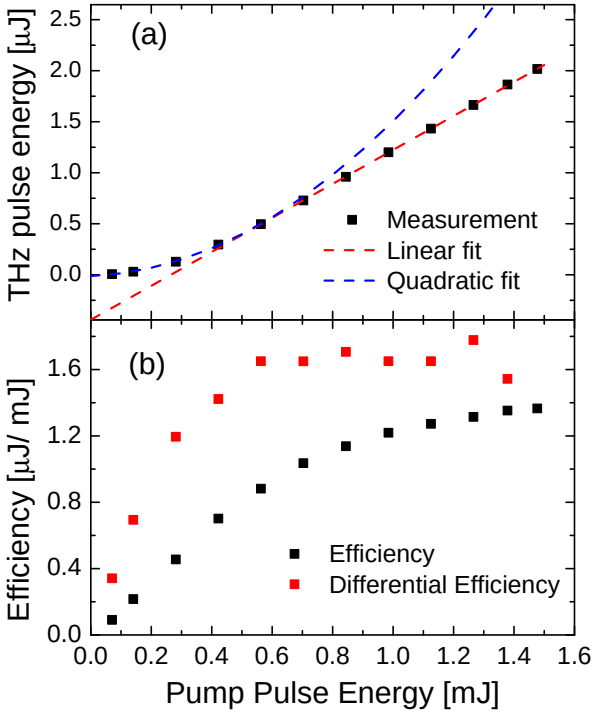

FIGURE 2.8: (a) The energy of the THz pulses generated in $LiNbO_3$ in a tilted wavefront configuration as a function of incident pump pulse energy. Dashed lines shows best linear and quadratic fits to experimental data. (b) Absolute $P_{\mathrm{THz}}/P_{\mathrm{NIR}}$ and differential $dP_{\mathrm{THz}}/dP_{\mathrm{NIR}}$ efficiency of THz generation in $LiNbO_3$.

and related to the intensity of the THz wave. Because being dependent on heating processes, response times of those devices are slow, sensitivity is low and they often require cryogenic cooling. A newer class of detectors comes from electronic approach and include Schottky diode mixers [86], high electron mobility transistors and many other.

The very commonly used way of detecting THz transients is using photoconductive switches [87–89]. THz detection in this scheme is a reverse

process to the THz generation using photoconductive antennas. Portion of the laser beam that is used for THz generation is split off and sent to the detector. The femtosecond laser pulse excites free carriers in the photoconductive gap of the detector semiconductor material. This time, instead of connecting electrodes to the bias circuit, they are connected to a current preamplifier. The electric field of the THz pulse drives photocurrent which is measured by the preamplifier. The photocurrent in the antenna is a convolution of the electric field and the transient photoconductivity excited by the gating pulse. If the transient photoconductivity is much faster than the dynamics of the electric field, then the measured current is directly proportional to the THz electric field. The bandwidth of detection is mainly limited by the trapping and recombination time of photoconductivity, and for that reason radiation-damaged silicon-on-sapphire [63], low-temperature grown GaAs [64, 65]or ion-implanted InGaAs [66, 67] are used.

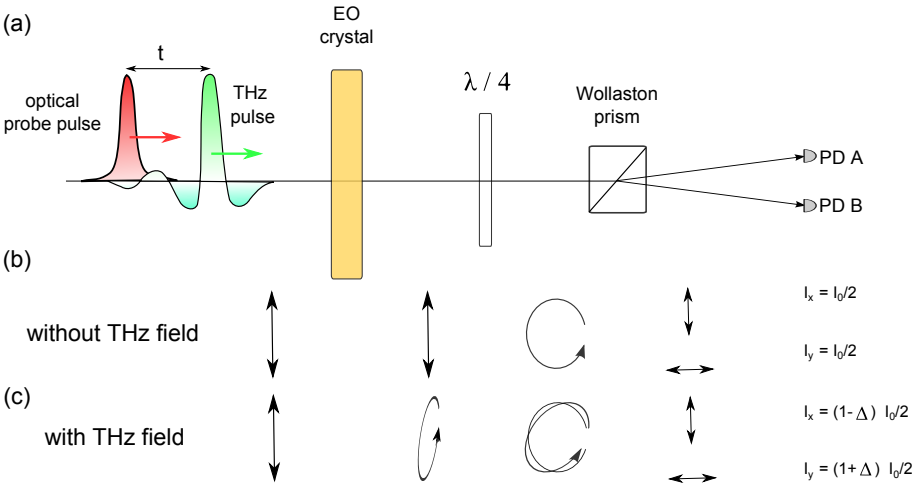

FIGURE 2.9: (a) Schematic confriguration of electrooptic sampling. Polarization of NIR probe beam are shown (b) without and (c) with THz electric field.

The other frequently used method of detecting THz pulses is free-space electro-optic sampling (FEOS) [27–29], which uses the Pockels effect

in an electro-optic (EO) crystal. Because FEOS is the method used through this thesis, it will be described in more detail. A schematic setup of the FEOS is presented in Fig. 2.9. In the absence of THz field, a linearly polarized NIR gating pulse travels through EO crystal unaffected, then it passes through a $\lambda/4$ plate where its linear polarization is changed into circular. The orthogonal polarization components are split by a Wollaston prism and sent to photodiodes (PD) A and B. Signal from photodiodes is sent to the lock-in amplifier, which subtracts the incoming signals. Because the probe beam after the $\lambda/4$ plate has circular polarization, the signal (current, which can be also converted into voltage) is identical and lock-in amplifier returns zero-reading. When the THz transient overlaps in time with the NIR gating pulse, the gating pulse experience phase retardation and its polarization is changed into elliptical. The phase retardation Γ between different components of the gating pulse is proportional to the strength of the THz pulse and can be expressed by

$$\Gamma = \frac{\omega n_0^3 r_{41} L}{c} E_{THz} \tag{2.5}$$

where n_0 is the refractive index at the optical frequency, r_{41} is the electrooptic coefficient ($\sim$4 pm/V for ZnTe [90] and $\sim$ 0.88 pm/V for GaP [91]), L is the thickness of the EO crystal, ω frequency of NIR probe and E_{THz} is the value of the THz electric field. This time the polarization of the gating beam after the $\lambda/4$ plate is not exactly circular and the photodiodes A and B do not show the same signal any more. Photocurrents at photodiodes A and B are

$$I_A = \frac{I_0}{2}\left(1 - \sin\Gamma\right), \tag{2.6}$$

$$I_B = \frac{I_0}{2}\left(1 + \sin\Gamma\right). \tag{2.7}$$

The modulation depth of photocurrents is directly proportional to the THz electric field:

$$\frac{\Delta I}{I_0} = \frac{I_B - I_A}{I_0} = \sin\Gamma = \sin\left(\frac{\omega n_0^3 r_{41} L}{c} E_{THz}\right), \tag{2.8}$$

which gives the expression for the THz electric field:

$$E_{THz} = \arcsin\left(\frac{\Delta I}{I_0}\right)\frac{c}{\omega n_0^3 r_{41} L} \approx \frac{\Delta I}{I_0}\frac{c}{\omega n_0^3 r_{41} L}. \tag{2.9}$$

For weak THz fields (i.e. $\frac{\Delta I}{I_0} < 0.5$), measured THz electric field is directly proportional to the photocurrent modulation. The phase retardation Γ also depends on the orientation of the crystal and directions of polarization of the THz radiation and the NIR laser pulse. For $\bar{4}3m$ zincblende structure crystals, such as ZnTe, the optimum angles between the THz and the probe beam polarizations are 0° or 90° [92, 93]. By varying time difference t between THz beam and NIR gate the entire THz waveform can be mapped in time. To improve signal-to-noise ratio the lock-in amplifier is locked to the frequency of optical chopper, which modulates the THz generation beam at a first subharmonic frequency (500Hz) of the laser system (1kHz). This detection scheme is characterized by excellent S/N ratios, which in most cases exceed 1000. Two reasons behind high S/N ratio are the coherent detection that rejects incoherent background radiation and a very short sampling time given by ultrashort gating pulse duration. ZnTe and GaP are the two most commonly use EO crystals. Other crystals, such as GaSe, InP, GaAs, DAST, BNA as well as some polymers and liquids have also been used. The detection bandwidth is limited by the phase matching between the THz transient and the NIR gating pulse. Other type of limitation comes from absorptive phonons in the crystals (such as T0 phonon in ZnTe at 5.3 THz and phonon at ∼11 THz in GaP [94]). By application of very thin EO crystals (e.g. $\sim 10\mu$m ZnTe), which minimizes influence of phase mismatch, the detection bandwidth can be increase even to over 100 THz [95–97]. Note that the detection of the magnetic field of the THz pulse is also possible in similar method [98, 99].

In recent years several detection methods based on air photonics have been developed [33, 100]. Due to its extreme broadband responsivity air biased coherent detection (ABCD) [34, 101] is gaining big popularity.

ABCD method will be described in detail in chapter 4.3. THz radiation-enhanced emission of fluorescence (REEF) [102] and terahertz enhanced acoustics (TEA) [103] are interesting examples of other methods based on interaction of intense femtosecond pulses with THz transients inside laser-induced plasma.

Chapter 3

Simultaneous reference and differential waveform acquisition in time-resolved terahertz spectroscopy

Time-resolved terahertz spectroscopy (TRTS) is a relatively new and powerful experimental technique for studying subpicosecond dynamics of photoexcited charge carriers in semiconductors [13, 14, 104] and other materials [11, 105]. To extract the frequency-resolved conductivity of a photoexcited sample, two THz transients are necessary: a reference scan, $E_{ref}(t)$, of the unexcited sample and a scan of the pumped sample, $E_{pump}(t)$. The most common data acquisition scheme is to separately measure $E_{ref}(t)$ with a blocked pump beam or at negative pump-probe delay times. Next step is to measure a differential THz scan, $\Delta E(t)$ and calculate $E_{pump}(t) = E_{ref}(t) + \Delta E(t)$. In this procedure two scans are taken separately and some false spectral features can be introduced if in between scans the output (power, pulse shape) of the laser system changes. In this chapter we present a new method of data acquisition in

which both scans are taken simultaneously. This approach is not only twice as fast, but also eliminates spurious errors in the spectroscopy arising from experimental conditions changing during data acquisition.

The chapter will begin with a brief introduction to time-domain terahertz spectroscopy and time-resolved terahertz spectroscopy. Then we will present and discuss the Drude model for conductivity, which is the most simple but also best understood model of conductivity in semiconductor sample. In the next part of the chapter we will in detail present the experimental setup and write about calibration methods. The chapter will end with results obtained for GaAs sample, which was chosen as a test sample.

3.1 Time-domain terahertz spectroscopy

Terahertz time-domain spectroscopy (THz-TDS) is a method of determining optical properties of investigated sample. High signal to noise ratio of photoconductive switches and THz emitters and detectors based on nonlinear phenomena makes those devices well suited for spectroscopic purposes. More over, since the electric field of THz transient is directly mapped in time (instead of intensity), both amplitude and phase information are coherently measured. This field information allows for direct determination of the complex refractive index (or equivalently complex dielectric function or complex conductivity) without a necessity to use Kramers-Kronig relations.

The real beauty of THz spectroscopy lays in the wealth of spectroscopic signatures in the THz energy range for all states of matter: gasses, liquids, solid-state and even plasma [2, 106]. Rotational excitations of small gas molecules have energies in the THz range and thus TDS-THz spectroscopy can be used to identify various gases [107, 108]. In liquids the THz spectrum is dominated by relaxation of either permanent dipoles in polar liquids or collision-induced dipole moments in nonpolar liquids.

So far water and its mixtures is probably the most extensively studied liquid in the THz range [109–111]. In the case of simple dielectrics THz spectroscopy allows for simple and accurate determination of the refractive index and absorption coefficient [87]. THz-TDS techniques have also been used for investigating such systems as insulators [112], inorganic and organic semiconductors [87], metals [113], doped semiconductors [114], quantum wells [115] and many others.

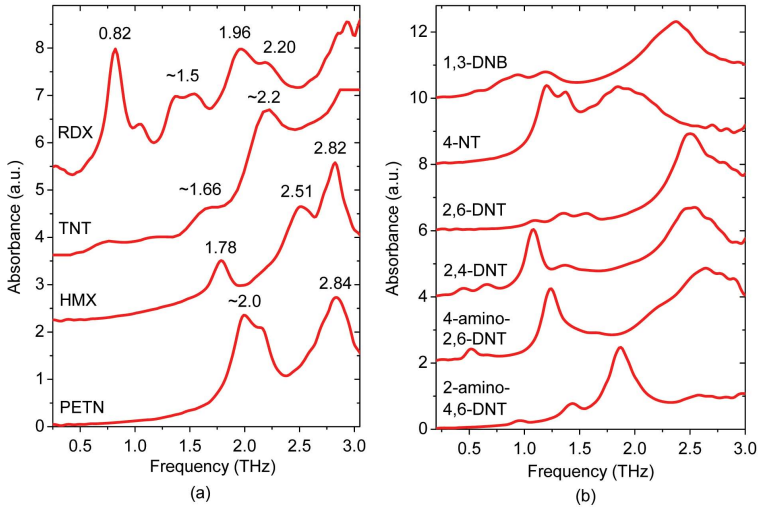

FIGURE 3.1: (a) THz absorption spectra of RDX, TNT, HMX and PETN obtained with THz-TDS. (b) THz absorption spectra of explosive related compounds obtained using THz-TDS. The spectra have been vertically shifted for clarity. [16]

The THz range hosts low frequency crystalline lattice vibrations - phonon modes, hydrogen-bonding stretches and other intermolecular vibrations of molecules in many materials. For purposes of this thesis the most important fact is probably that the transmitted and reflected spectra of explosives and related compounds (ERCs) contain THz absorption fingerprints characterizing these THz vibrational modes [42, 43, 116, 117].

Fig. 3.1 shows measured THz absorption spectra of hexahydro-1,3,5-trinitro-1,3,5-triazine (RDX), 2,4,6-trinitrotoluene (TNT), tetramethylene tetranitramine (HMX), pentaerythritol tetranitrate (PETN) and explosive related compounds: 1,3-dinitro-benzene (1,3-DNB), 4-nitrotoluene (4-NT), 2,6-dinitro-toluene (2,6-DNT), 2,4-DNT, 4-amino-2,6-DNT and 2-amino-2,6-DNT. Most of these THz absorption fingerprints are from the lattice vibrational modes of solid-state explosive materials. Absorption fingerprint in a broad range from 0.05 - 0.6 THz of such explosive as DNT has been also measured in its gas-phase [118].

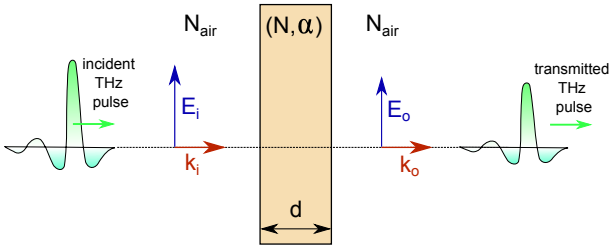

FIGURE 3.2: THz transmission through a sample of a thickness d and a real refractive index N and an absorption coefficient α.

Below we will show how to determine the frequency dependent refractive index $N(\omega)$ and the absorption coefficient of a sample $\alpha(\omega)$ in a transmission configuration of a THz-TDS system. For simplicity we assume that the THz radiation is incident at a normal angle to the sample surface - Fig. 3.2.

Two measurements are necessary to extract the refractive index and the absorption coefficient of a sample. The first one is a reference pulse E_{ref}, which is taken without the sample in the spectrometer.

$$\tilde{E}_{ref}(\omega) = \tilde{E}_i(\omega) \cdot e^{-\alpha_{air}(\omega)d/2} \cdot e^{-i\omega N_{air}(\omega)d/c}, \tag{3.1}$$

where $\tilde{E}_i(\omega)$ is the incident THz transient, $N_{air}(\omega)$ is the real part of the refractive index of air and $\alpha_{air}(\omega)$ is the absorption coefficient of air (here $N_{air}(\omega)$ is here is assumed to be 1 and $\alpha_{air}(\omega)$ is assumed to be 0). The second measurement $\tilde{E}_{samp}(\omega)$ is done when the sample is

placed in the THz path inside the spectrometer.

$$\tilde{E}_{samp}(\omega) = \tilde{t}_{12}\tilde{t}_{21}\tilde{E}_i(\omega) \cdot e^{-\alpha(\omega)d/2} \cdot e^{-i\omega N(\omega)d/c}, \tag{3.2}$$

where $\tilde{t}_{12}$ and $\tilde{t}_{21}$ are the Fresnel transmission coefficients. In the case of an air-sample interface, $\tilde{t}_{12} = \frac{2}{1+\tilde{n}}$, where $\tilde{n}$ is the complex refractive index of the sample ($\tilde{n}(\omega) = N(\omega) - i\kappa(\omega) = N(\omega) - ic/2\omega \cdot \alpha(\omega)$). For the sample-air interface $\tilde{t}_{21} = \frac{2\tilde{n}}{\tilde{n}+1}$. Taking the ratio between $\tilde{E}_{samp}(\omega)$ and $\tilde{E}_{ref}(\omega)$ one gets the complex transmission function $\tilde{T}(\omega)$

$$\tilde{T} = \frac{\tilde{E}_{samp}}{\tilde{E}_{ref}} = \frac{4\tilde{n}(\omega)}{[1+\tilde{n}(\omega)]^2} \cdot e^{-\alpha(\omega)d/2} \cdot e^{-i\omega[N(\omega)-1]d/c} = \left|\tilde{T}(\omega)\right| \cdot e^{-i\Phi(\omega)}. \tag{3.3}$$

In the case when the sample thickness is comparable to or larger than the THz wavelength, the phase shift arising from the Fresnel coefficient is much smaller than the phase shift originating from the wave propagation through the sample and the real part of the sample refractive index can be expressed by:

$$N(\omega) \simeq 1 + \frac{c}{\omega d}\Phi(\omega). \tag{3.4}$$

Once the refractive index $N(\omega)$ is determined, one can calculate the absorption coefficient of the sample using

$$\alpha(\omega) = -\frac{2}{d} \cdot \ln\left[\left|\tilde{T}(\omega)\right| \frac{[1+N(\omega)]^2}{4N(\omega)}\right]. \tag{3.5}$$

The amplitude $\left|\tilde{T}(\omega)\right| = \frac{\left|\tilde{E}_{samp}(\omega)\right|}{\left|\tilde{E}_{ref}(\omega)\right|}$ and phase $\Phi(\omega) = \theta_{samp} - \theta_{ref}$ of the complex transmission function are obtained from the ratio of the Fourier transforms of $E_{samp}(t)$ and $E_{ref}(t)$.

3.2 Time-resolved terahertz spectroscopy

Time-domain THz spectroscopy allows only for measurement of static optical functions. But already in the mid 1980's people realized that subpicosecond THz transients, which are synchronized to optical femtosecond pulse trains, open possibility for pump-probe experiments that could provide a way to study dynamical properties of picosecond nonequilibrium processes in the THz frequency range [119]. This technique is know as time-resolved terahertz spectroscopy (TRTS) or transient THz spectroscopy. It is a non-contact method capable of determining the evolution of the frequency-dependent photoconductivity with a temporal resolution better than 200 fs. TRTS is a time-domain technique, where the spectral information is obtained by Fourier transform of near-single-cycle transients following interaction with a sample, usually by transmission. TRTS has a huge impact on our understanding of ultrafast phenomena in systems such as: inorganic [12, 13, 104, 120, 121] and organic [122] bulk semiconductors and insulators [112], liquids [123], superconductors [124–126]. In recent years the research focus in ultrafast phenomena studied with TRTS methods has been placed on nanostructures, such as nanocrystals [14, 127], quantum wells [128], quantum dots [129–131], carbon nanotubes [127, 132], conjugated polymer/nanorod composites [133] and many other [11, 105].

The physical picture of TRTS spectroscopy on photoexcited semiconductors is based on interaction between THz wave and excited free carriers in the conduction (electrons) and valence (holes) band. The THz electric field accelerates carriers, which next scatter and dissipate energy gained from the THz wave. This energy transfer from THz transient to the free carriers causes decrease in the THz field strength. Absorption of THz radiation depends both on the carrier density n and on the mobility μ of carriers through conductivity of the sample $\sigma = en\mu$. The mobility μ of the carrier, describes how quickly a given carrier can move through a metal or semiconductor, when pulled by an electric field. In many

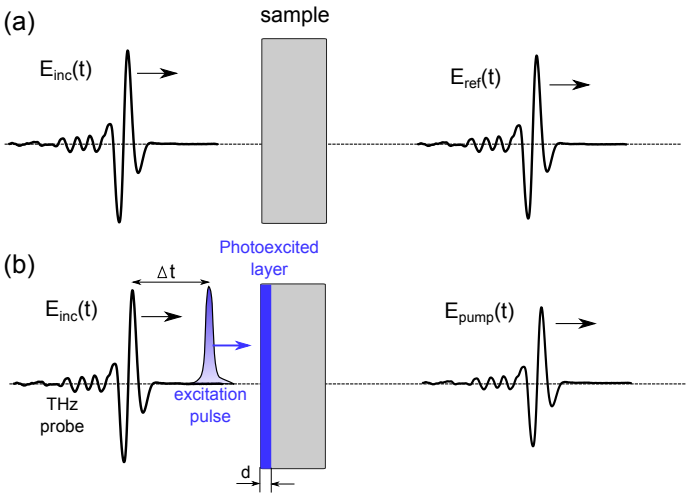

FIGURE 3.3: THz transmission through (a) unexcited and (b) photoexcited sample.

materials the mobility of holes is much lower then the mobility of electrons ($400\ cm^2/(Vs)$ for holes and $8500\ cm^2/(Vs)$ for electrons in GaAs at room temperature [134]), so the THz absorption will be dominated by absorption by electrons in the conduction band. In those materials TRTS will probe mostly dynamics of photoexcited electrons.

The complex transmission function $\tilde{t}$ through a thin conducting film placed between two media with real refractive indices is know as the Tinkham equation [135]:

$$\tilde{t} = \frac{2Y_1}{Y_1 + Y_2 + d\tilde{\sigma}}, \tag{3.6}$$

where d is the thickness of the film, $\tilde{\sigma}$ is its complex conductivity, Y_1 and Y_2 are admittances of the surrounding materials. Substituting $Y_1 = 1/Z_0$ for free space or air and $Y_2 = N/Z_0$ for the dielectric substrate with refractive index N we find

$$\tilde{t}(\omega) = \frac{2}{N + 1 + Z_0 d\tilde{\sigma}(\omega)} \tag{3.7}$$

where $Z_0 = 377\Omega$ is free space impedance. This equation is valid as long as $d \ll \lambda/n$, that is as long the wavelength inside the conducting film (with refrative index n) is longer than the film thickness and all internal reflections and interferences can be neglected. Values of n high enough to make the expression invalid can be obtained in metallic thin films but for semiconductors investigated in this thesis Eq. 3.7 is valid. The next limitation for applicability of Eq. 3.7 is that the temporal changes of conductivity $\tilde{\sigma}$ have to be slower than the THz pulse duration. If the transmission function of the unexcited dielectric slab (substrate) $\tilde{t}_{subs} = \frac{2}{N+1}$ is treated as a reference, then a transmission $\tilde{T}(\omega)$ through the photoexcited slab (thin film with pump induced photoconductivity $\Delta\tilde{\sigma}(\omega)$) is in the form:

$$\tilde{T}(\omega) = \frac{\tilde{E}_{pump}(\omega)}{\tilde{E}_{ref}(\omega)} = \frac{N+1}{N+1+Z_0 d\Delta\tilde{\sigma}(\omega)}. \tag{3.8}$$

In case the thickness d of the photoexcited film cannot be determined, it may be convenient to use sheet photoconductivity $\Delta\tilde{\sigma}_s$ defined as $\Delta\tilde{\sigma}_s(\omega) = d \cdot \Delta\tilde{\sigma}(\omega)$.

Two scans are needed to extract the frequency dependent photoconductivity: a reference scan $E_{ref}(t)$ and a pumped scan $E_{pump}(t)$. The reference scan is taken with blocked pump beam or at the negative pump-probe delay time, when the THz probe pulse does not experience pump pulse. The pumped scan $E_{pump}(t)$ carries the information about the photoexcitation - Fig. 3.3. However in most TRTS systems the differential $\Delta E(t)$ waveform is mapped and then $E_{pump}(t)$ is calculated by $E_{pump}(t) = E_{ref}(t) + \Delta E(t)$ (Fig. 3.4), instead of measuring directly $E_{pump}(t)$, . The measurement of $\Delta E(t)$ is done by moving the optical chopper from the THz generation beam to the optical pump beam to improve signal to noise ratio of the analyzed data. In Chap. 3.4 we present a novel method that allows for simultaneous reference $E_{ref}(t)$ and differential waveform $\Delta E(t)$ acquisition.

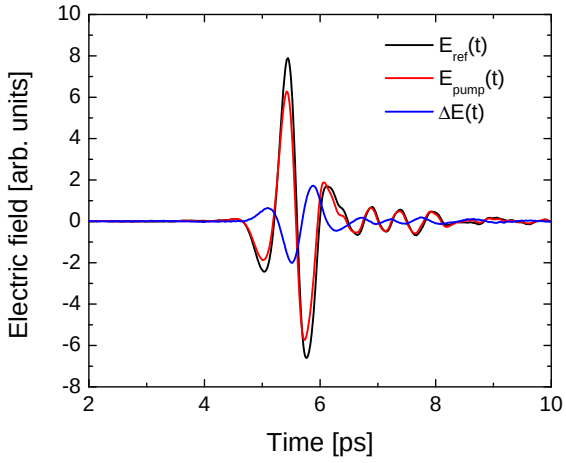

FIGURE 3.4: Reference $E_{ref}(t)$, pump $E_{pump}(t)$ and differential $\Delta E(t)$ waveforms for time-resolved spectroscopy on semi-insulating GaAs, photoexcited with 400 nm light 30 ps after excitation at room temperature. The pump fluence is 25 μJ/cm^2.

By a simple manipulation of Eq. 3.8 in the polar coordinates the complex sheet conductivity $\Delta\tilde{\sigma}_s = \Delta\sigma_s' + i\Delta\sigma_s''$ can be split into real and imaginary parts:

$$\Delta\sigma_s'(\omega) = \frac{N+1}{Z_0}\left[\frac{1}{|T(\omega)|}\cos\left[\Phi(\omega)\right] - 1\right] \tag{3.9}$$

$$\Delta\sigma_s''(\omega) = -\frac{N+1}{Z_0}\left[\frac{1}{|T(\omega)|}\sin\left[\Phi(\omega)\right]\right] \tag{3.10}$$

The amplitude $\left|\tilde{T}(\omega)\right| = \frac{\left|\tilde{E}_{pump}(\omega)\right|}{\left|\tilde{E}_{ref}(\omega)\right|}$ and phase $\Phi(\omega) = \theta_{pump} - \theta_{ref}$ of the complex transmission function are obtained from the ratio of the Fourier transforms of $E_{pump}(t)$ and $E_{ref}(t)$. By changing the time delay Δt between the photoexcitation pulse and the THz probe pulse, the dynamics of the photoconductivity can be mapped out.

3.3 Drude conductivity

Linear response of charge carriers to an applied electric field can be fully described by a complex conductivity function $\tilde{\sigma}(\omega) = \sigma'(\omega) + i \cdot \sigma''(\omega)$. Several models have been developed to describe conductivity in semiconductors. Even though many of those models have been created before quantum mechanics, they are still able to describe complicated problems in a rather accurate way. The simplest and the most commonly used is the Drude model [136], in which carriers are considered free to respond to the electric field. In addition to acceleration by an external field, mobile carriers undergo collisions with scattering centers described by a characteristic scattering time τ. The collisions are assumed to be instantaneous, elastic and randomly changing momentum of the carrier. The frequency dependent complex conductivity of a conductor according to Drude model is described by [136]:

$$\tilde{\sigma}(\omega) = \sigma'(\omega) + i \cdot \sigma''(\omega) = \frac{\sigma_{dc}(\omega)}{1 - i\omega\tau}. \tag{3.11}$$

DC conductivity σ_{dc} is expressed using scattering time τ, carrier density n and effective mass of the carrier m^* by:

$$\sigma_{dc} = \frac{ne^2\tau}{m^*} = \omega_p^2 \epsilon_0 \tau, \tag{3.12}$$

where the plasma frequency ω_p is defined as $\omega_p^2 = ne^2/\epsilon_0 m^*$. The Drude model also gives expression for the mobility of carriers $\mu = \frac{e\tau}{m^*}$, from which we see that the heavier the effective mass m^* of a carrier the lower the mobility.

Equation 3.11 can be seperated into real and imaginary parts

$$\sigma'(\omega) = \sigma_{dc} \frac{1}{1 + (\omega\tau)^2}, \tag{3.13}$$

$$\sigma''(\omega) = \sigma_{dc} \frac{\omega\tau}{1 + (\omega\tau)^2}. \tag{3.14}$$

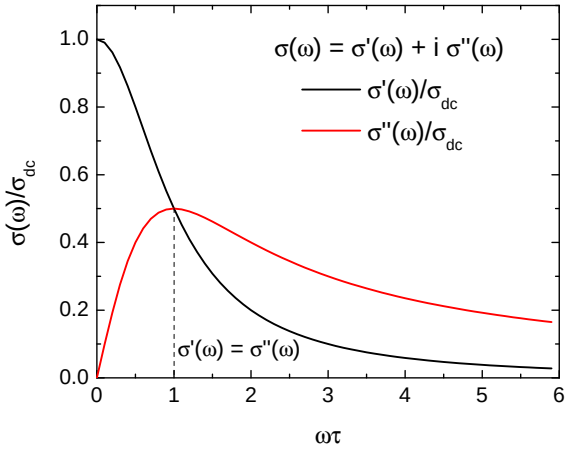

FIGURE 3.5: Real and imaginary parts of complex conductivity in the Drude model.

Figure 3.5 shows the real and imaginary parts of the complex Drude conductivity normalized by DC conductivity σ_{dc} as a function of the product $\omega\tau$. The most feature-rich area of the plot is in the vicinity of $\omega\tau = 1$, where $\sigma'(\omega) = \sigma''(\omega)$. For typical semiconductors, the scattering time τ is on the order of tens to few hundreds of femtoseconds, so the characteristic frequency where $\omega\tau \sim 1$ is placed in the terahertz region. For that reason, if one is able to measure the complex conductivity function of semiconductor in the THz range and one assumes that the response is given by only one type of carrier, one can accurately extract carrier concentration, mobility and scattering time.

3.4 Experimental Setup

Figure 3.6(a) shows the schematic representation of the time-resolved terahertz spectroscopy setup. A regenerative Ti:sapphire femtosecond laser amplifier is delivering 45 fs, 2.8 mJ pulses with center wavelength

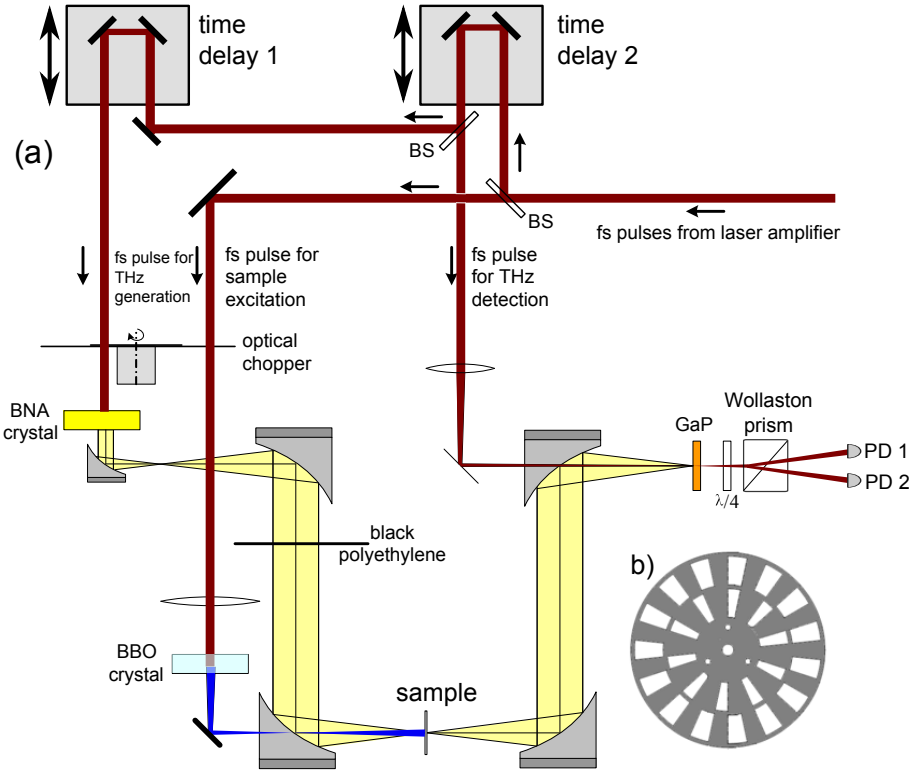

FIGURE 3.6: (a) Schematic of the simultaneous reference and differential waveform acquisition TRTS setup. (b) 2 frequency chopper blade.

of 800 nm at a 1 kHz repetition rate. The laser output is split into three portions: a source beam for THz pulse generation, a pump beam for excitation of the sample and a gating beam for THz detection by free space electro-optic sampling. Terahertz waves are generated by optical rectification in 1.4 mm-thick [010] N-benzyl-2-methyl-4-nitroaniline (BNA) crystal [73, 74], which in detail is presented in chapter 2.2.1. The 800 nm light transmitted through the BNA crystal is blocked by a black polyethylene sheet, transmissive to the THz pulse. Off-axis parabolic mirrors are used to expand the THz beam and next to collimate and focus it to a $\sim$ 1 mm-diameter spot on the sample. The transmitted THz

pulse is then collimated and re-focused onto a [110] GaP crystal (300 μm-thick) for free space electro-optic detection of the THz transients. GaP is chosen for detection over the more efficient ZnTe to allow higher bandwidth detection, as the first phonon is at ∼11 THz whereas ZnTe has its first phonon at ∼5.3 THz [94]. The usable bandwidth of such a system extends from 0.1 to nearly 6 THz - Fig. 3.7(b) and is over two times broader than a similar setup with THz generation based on optical rectification in ZnTe. The highest THz electric fields obtained in this setup are on the order of ∼ 5 kV/cm so we do not expect to observe any nonlinear phenomena. The setup was enclosed in a plexiglass box and purged with dry N_2 to avoid water absorption lines. Both the 800 nm probe beam and the pump beam were focused through small holes in the centers of off-axis parabolic mirrors for collinear detection and excitation of the sample at normal incidence. The pump beam was frequency doubled to 400 nm by β-BaB_2O_4 (BBO) crystal to ensure that the ∼ 15 nm penetration depth of the pump beam in semi-insulating gallium arsenide (SI GaAs) creates a film thin enough to fulfil the thin film approximation [137]. The sample is mounted on the back of a 1.5 mm-diameter aperture to aid in pump/probe overlap. The pump beam spot is approximately 3 mm in diameter, ∼3 times larger than the THz spot which ensured uniform excitation [138]. Two computer controlled delay stages are used to change the pump-probe delay times and also to map the THz pulse shape. The setup is constructed in such a way that one delay stage is scanning the time interval between the pump pulse with respect to both the THz source and probe pulses. In this way the whole THz transient is experiencing a constant delay from the pump pulse [139].

Double modulation is a well-known technique for both static and time-resolved terahertz spectroscopy [140–143], however to date this has only been used for noise reduction of the differential scan. The key element in simultaneous acquisition of reference and differential THz scans is the use of a two frequency chopper blade, which shape is shown on Fig 3.6(b). The chopper blade consists of two kinds of sets of slots and

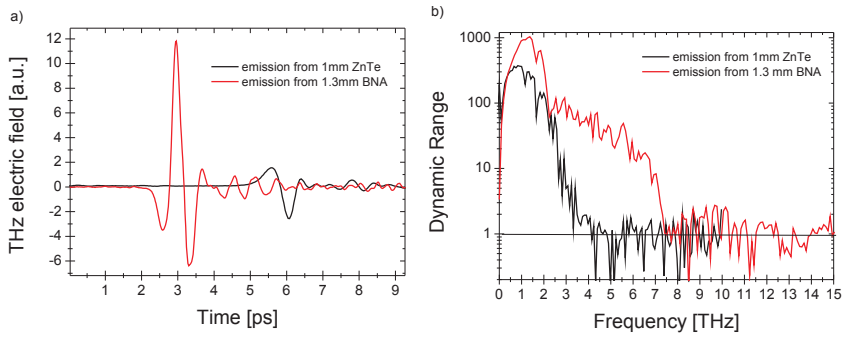

FIGURE 3.7: (a)Waveforms and (b) spectra of THz radiation generated in 1 mm-thick (110) ZnTe and 1.3 mm-thick (010) BNA and crystals.

shutters. The outer set is built of 15 slots and 15 shutters in equal spacing, while the inner set consists of 10 slots and 10 shutters, where the shutters are twice as wide as the slots. The chopper blade is rotating at such a speed to modulate the beam going though the outer part at 500 Hz, synchronized to the 1-kHz repetition rate of the laser. At the same time chopper blade modulates the beam going though the inner part at 333 Hz. The output from the balanced photodiode detector is split and sent to two independent lock-in amplifiers. The reference signals for the lock-in amplifiers are second (500Hz) and third (333 Hz) sub-harmonics of the laser system reference signal, and therefore are not harmonic with respect to each other. As a result the cross talk between signals measured at those frequencies is on the noise level.

Figure 3.8 shows the time sequence of the laser, pump, generation and THz pulses with respect to each other. The inner chopper blade selects every third pulse which is used for THz generation, while the outer blade transmits every second pulse which is used as a pump. The first transmitted THz transient does not experience the presence of a pump, while the transmission of the second THz pulse decreases due to increased absorption from excited free carriers. The reference and pumped electric fields of the terahertz transients can be expressed by the signals measured by the first [$E_1(t)$, modulated at 333 Hz] and the second [$E_2(t)$,

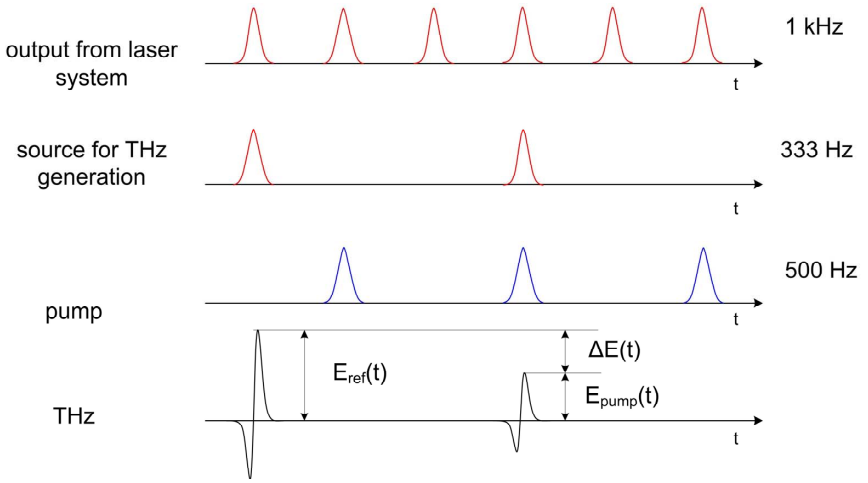

FIGURE 3.8: Time sequence of incoming pulses.

modulated at 500 Hz] lock-in amplifiers by

$$E_{ref}(t) = E_1(t) + AE_2(t) \tag{3.15}$$

$$E_{pump}(t) = E_1(t) - AE_2(t) \tag{3.16}$$

where A is a calibration constant.

Figure 3.9(a) shows a typical shape of the voltage difference V_{1-2} between the two balanced photodiodes while monitoring the induced phase retardation at the peak of the THz transient, as illustrated in the lowest row of signals in Fig. 3.8. The exponential decay at $t = 0$ ms corresponds to the transmitted THz signal strength without pump, whereas the exponential decay at $t = 3$ ms corresponds to the transmitted THz signal with pump light, thus resulting in a lower amplitude. The values

measured by the lock-in amplifiers at 333 Hz and 500 Hz are correspondingly the third (a_{333}) and second (a_{500}) harmonic Fourier coefficients of the repetitive voltage difference between the two photodiodes with 6-ms period (167 Hz repetition rate). The constant A can be expressed using a_{333} and a_{500} by

$$A = \frac{a_{333|\text{pump off}} - a_{333|\text{pump on}}}{a_{500|\text{pump on}}}. \tag{3.17}$$

Figure 3.9(b) shows calculated values of the calibration constant A as a function of the decay time τ of the voltage difference. For fast photodiodes ($\tau \approx 0$) the constant A is 1, and increases to a maximum value at $\tau = 0.75$ ms, followed by a gradual decrease at even slower photodiode response times. We note that not only the decay time constant, but also the detailed shape of the photodiode decay curve can influence the constant A significantly.

Figure 3.10(a) shows the measured E_1 and E_2 signals of the peak of the THz pulse as a function of time after 400 nm excitation of undoped silicon, as well as the calculated E_{ref} and E_{pump}. The carrier life time in silicon following 400 nm excitation is on the order of hundreds of μs [144], and so the first 20 ps after excitation the E_{pump} response is flat. This step-like response allows for accurate experimental determination of the constant A, which is found to be equal to 1.33. The decay constant of the voltage difference V_{1-2} between the balanced detector photodiodes was found to be 1.02 ms, what corresponds to the value of A of 1.28. The difference from the experimentally obtained value can be explained by variations of the voltage difference waveform from a pure exponential decay. Figure 3.10(b) shows the reference signal E_{ref}, calculated from E_1 and E_2. E_{ref} is constant except for near the arrival of the pump where a slight distortion originating from the detector response is visible.

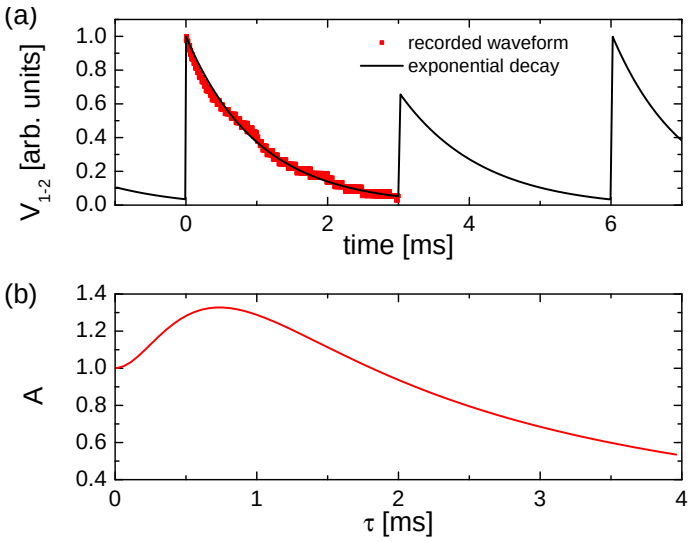

FIGURE 3.9: (a) The experimental waveform (points) of the voltage difference V_{1-2} between the balanced detector photodiodes with an exponential decay fit (solid line) extended to later times to represent a typical shape of the voltage difference during experiments with the simultaneous data acquisition scheme. The decay constant for the voltage difference was found to be 1.02 ms. (b) The calculated values of the constant A as a function of photodiodes decay time t under the assumption that voltage difference V_{1-2} is composed of pure exponential decays.

3.5 Results

Frequency-resolved THz spectroscopy was performed on a 0.44 mm-thick wafer of semi-insulating gallium arsenide (SI GaAs), which has become the standard test material for TRTS for its well known Drude conductivity response [12, 139], carrier dynamics and optical absorption [145].

Figure 3.11 presents the complex sheet conductivity, $\Delta\tilde{\sigma}_s$, in SI GaAs 30 ps after 400 nm excitation. The applied pump fluence is 25 μJ/cm^2, what results in a maximum differential THz transmission of 21%. The

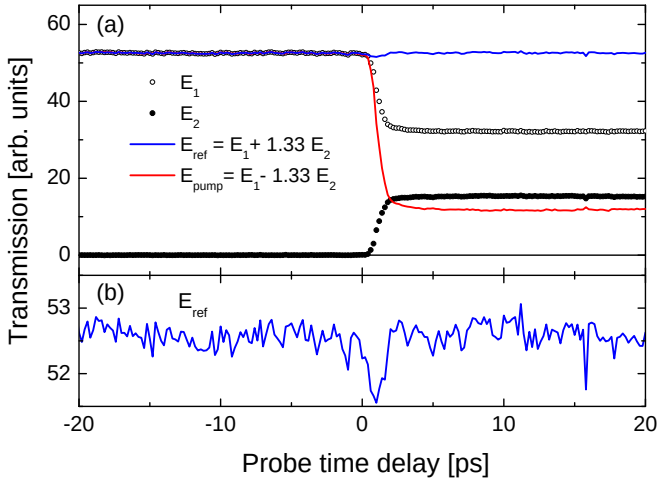

FIGURE 3.10: (a) Measured E_1 and E_2 signals at the peak of THz pulse after 400 nm excitation of semi-insulating silicon in a 1D pump-probe experiment. (b) The recovered reference signal $E_{ref} = E_1 + AE_2$ ($A = 1.33$) indicating a disordered response at the arrival of the pump.

left column (a-c) shows data obtained with the standard data acquisition method (E_{ref} and $\Delta E\,(t)$ obtained in separate scans). Reference $E_{ref}\,(t)$, pump $E_{pump}\,(t)$ and differential $\Delta E\,(t)$ waveforms for Fig. 3.11(a) are presented in the Fig. 3.4. The right column (d-f) shows results of measurements in which the simultaneous data collection scheme was applied. The individual plots differ from each other by the number of measured THz pulses used for averaging, which was done in the time-domain. The observed transient complex conductivity of photoexcited SI GaAs can be well described by a simple Drude model, although to a varying degree depending on data acquisition method and the number of averaged scans. It is evident that the spectra extracted from the simultaneous detection scheme employed here are better represented by the Drude model than the spectra obtained by separate acquisition. Drude model fits to both $\Delta\sigma_s'\,(\omega)$ and $\Delta\sigma_s''\,(\omega)$ data were performed simultaneously using the Levenberg-Marquardt algorithm [146]. The

Drude scattering time τ obtained using the separate and simultaneous acquisition methods differ, and the standard method gives lower values with greater variations. The results obtained with simultaneous data acquisition are identical within error and the uncertainty decreases with number of scans.

Comparing Fig. 3.11 (a) and (d) it can be seen that especially at high frequencies the conductivity spectrum obtained using the simultaneous method contains more noise. This behaviour can be explained by the fact that only every third pump pulse is measured by the E_2 signal, so the signal to noise ratio (SNR) decreases by a factor of $\sqrt{3}$ in comparison to the standard technique. This estimation of SNR is valid under the assumptions that the main source of noise in the system is the laser. In the case when the SNR is determined by the electrical noise from photodiodes and lock-in amplifiers (ΔE is not much higher than noise on a base line), the fact that $E_2 = \frac{1}{2A}\Delta E$ results in further decrease in SNR by a factor of $2A$. However, the factor of 2 which is gained in data acquisition speed with the simultaneous method increases signal-to-noise ratio by a factor of $\sqrt{2}$ for a given acquisition time. This is also observed when comparing Fig. 3.11(c) and Fig. 3.11(f). Scattering of data points at high frequencies, caused by the high ω roll-off of the THz pulse power spectrum, decreases with the number of scans in the average. The bandwidth at which the collected data agrees with the Drude model increases with the number of scans only for the simultaneous detection scheme.

Analyzing Figs. 3.11(a), (b) and (c) we find that the data obtained using the standard method are characterized with lower point to point noise, but the agreement with the Drude model is very poor. At frequencies higher than 1.5 THz, $\Delta\sigma_s'(\omega)$ is higher than expected from the Drude model, while $\Delta\sigma_s''(\omega)$ is lower than expected. Such a difference can have its origins in a small time shift between the reference E_{ref} and differential ΔE scans. A constant time shift Δt results in a linear phase shift $\Delta\Phi(\omega) = \omega\Delta t$. Based on the fact that $\cos(\Phi + \Delta\Phi) \approx \cos(\Phi) - \Phi\Delta\Phi$ and $\sin(\Phi + \Delta\Phi) \approx \sin(\Phi) + \Delta\Phi$ (which holds for $|\Delta\Phi| \ll |\Phi| \ll$

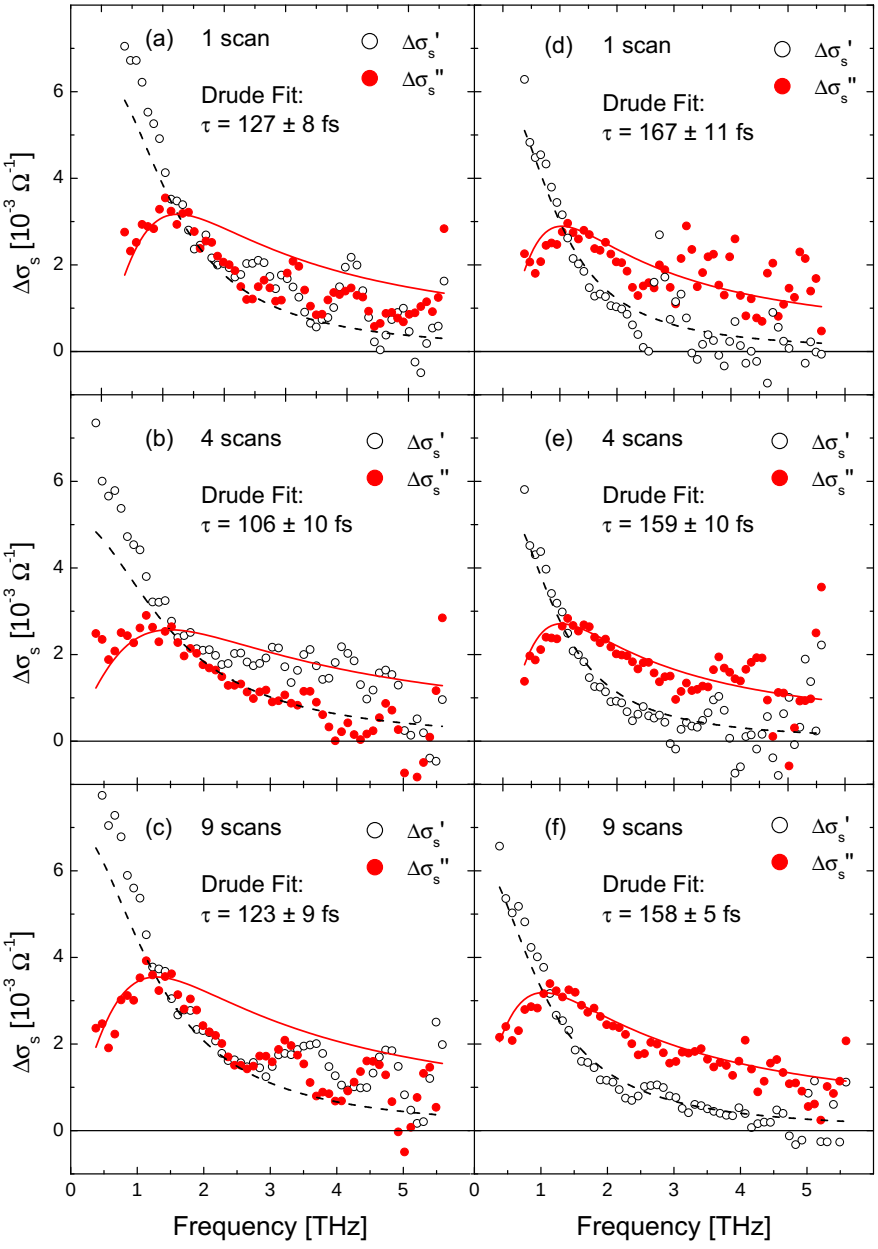

FIGURE 3.11: Complex sheet conductivities $\Delta\tilde{\sigma}_s = \Delta\sigma_s' + i\Delta\sigma_s''$ of photoexcited SI GaAs, 30 ps after 400 nm excitation at room temperature. Conductivity extracted by taking (a-c) two separately and (d-f) simultaneously acquired reference and pump waveforms. The lines over the conductivity data are simultaneous Drude fits to $\Delta\sigma_s'$ and $\Delta\sigma_s''$ with scattering times given in the figures.

1) and using Eqs. 3.9 and 3.10 we find expressions for the measured sheet conductivities $\Delta\sigma_s^{'*}(\omega)$ and $\Delta\sigma_s^{''*}(\omega)$,

$$\Delta\sigma_s^{'*}(\omega) = \Delta\sigma_s'(\omega) - \frac{N+1}{Z_0}\frac{1}{|T(\omega)|}\Phi\Delta\Phi, \tag{3.18}$$

$$\Delta\sigma_s^{''*}(\omega) = \Delta\sigma_s''(\omega) - \frac{N+1}{Z_0}\frac{1}{|T(\omega)|}\Delta\Phi. \tag{3.19}$$

A constant time shift influences both the real and imaginary part of conductivity in a linear fashion with opposite signs of the corrections to the real and the imaginary part (Φ is negative for a Drude response). This phase error influences the results of the extracted conductivity more at higher frequencies than lower frequencies. The relative error in the phase will be less in the vicinity of the scattering rate since this is where the transmission function has a peak in its phase response.

An analysis of the data in Fig. 3.11(c) shows that a constant time shift of 17 fs between the reference and differential scans can explain most of the disagreement between the data and the Drude model. The new value for the scattering time taking this shift into account is 141 ± 7 fs and is in better agreement with that obtained using simultaneous data acquisition scheme. To test the simultaneous data acquisition, we similarly performed a fit including a floating time shift correction to data from figure 3.11(f). A time shift of 1.0 ± 0.5 fs was found to improve the Chi^2 of the fit, but this is on level of accuracy of delay lines and confirms the principle of simultaneous scans acquisition.

A small time shift between the reference transient E_{ref} and the differential ΔE can have several origins. It can be a result of a change in the optical path between the THz generation and gating pulse (on the order of few just few μm), which can be caused by temperature changes of the optical table and elements on it, changes in the refractive index of air due to variations in atmospheric humidity or N_2 purging conditions, or changes in the output of the laser system. Particularly changes in the near infrared pulse duration can greatly impact the shape of the amplitude spectrum of the generated THz radiation. Accurate spectroscopy

therefore demands very stable laboratory conditions. Because a time shift results in a linear phase shift, this requirement is even more important for high bandwidth spectroscopy. The simultaneous detection scheme presented here eases the demands of these stability conditions. We note that in this case the conductivity response of the tested material was known in advance to be of Drude form. In more exotic materials where the response is unknown, elimination of these artifacts resulting from instability in experimental conditions is imperative for accurate spectroscopy and interpretation of the experimental data.

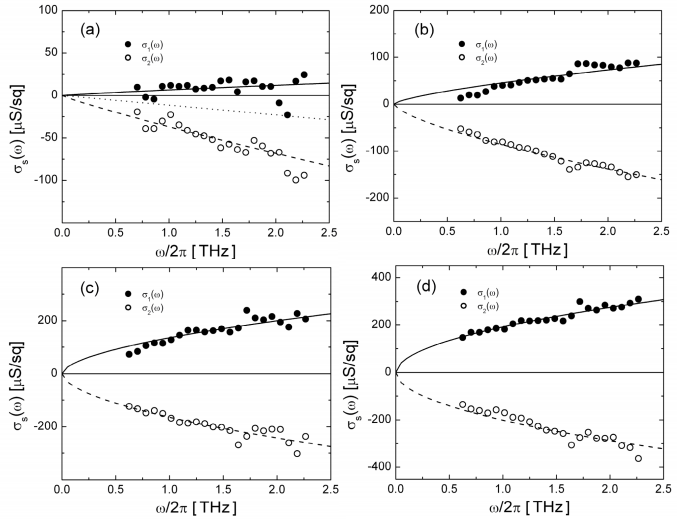

FIGURE 3.12: Complex sheet conductivity 1 ps after photoexcitation with 400 nm light at a fluence of 1.9 mJ/cm^2 for (a) P3HT, (b) P3HT:PCBM, (c) CdSe nanorods and (d) P3HT:CdSe nanorods as an example of non-Drude conductivity studied with simultaneous reference and differential waveform acquisition. The real conductivity increases with frequency, the imaginary conductivity is negative and both real and imaginary components are comparable in magnitude over the THz bandwidth. (from [133])

This developed by us method of simultaneous reference and differential waveform acquisition has been successfully applied in other experiments. Systems exhibiting pure Drude photoconductivity response (as

semiconductors [147]), and non-Drude response (InGaN/GaN multiple quantum well [128], black silicon [128] and conjugated polymer/CdSe nanorod composites [133] - Fig. 3.12) have been investigated. A similar method of two lockin detection for time-resolved terahertz spectroscopy was independently developed by Golde *et al.* [148].

3.6 Conclusions

In summary, we have suscessfully applied 1.4 mm-thick [010] BNA generation crystal combined with 0.3 mm-thick [110] GaP detection crystal to perform TRTS experiments with a bandwidth expanding from 0.1 to nearly 6 THz, which is over two time broader then similar setup based on ZnTe. We developed a new method for simultaneous data acquisition in time-resolved terahertz spectroscopy experiments. We have applied this method to extract the sheet conductivity of photoexcited carriers in SI GaAs and compared the results with those of a standard data acquisition scheme. We have shown that application of the new method minimizes errors in spectrally resolved photoconductivity data originating from fluctuations in the laser system output and timing errors in the THz pulse detection.

Chapter 4

Imaging THz field insidea parallel plate waveguide

Guiding of terahertz waves by various structures is a topic of extensive investigation [149]. Due to its unique properties such as dispersionless propagation of the TEM mode with no frequency cut-off, the parallel plate waveguide (PPWG) has attracted significant attention [104, 150–154] . Recently a tapered PPWG (TPPWG) has been proposed [155–157]. THz waves can be confined inside a TPPWG on subwavelength scale in both transverse dimensions [158] thus enabling THz near-field spectroscopy with subwavelength resolution. Recently a nanofocusing of mid-infrared radiation has been experimentally illustrated [159]. The TPPWG also offers significant field enhancement and thus has a big potential for investigation of nonlinear THz phenomena with tabletop laser sources, which in recent years has become a very active research field. For experimental characterization of the TPPWG it is necessary to characterize the electric field distribution inside the waveguide. Recently a method based on scattering of the field from needle tip inserted into the waveguide was demonstrated [160].

In the first part of the chapter we present a short review of chosen topic concerning THz waveguides. In more detail we describe parallel plate waveguide, which is in the focus of this chapter. Thereafter a short introduction to the air bias coherent detection of THz radiation will be given. As a next part of the chapter we present a new non-invasive method for characterization of the propagating electric field inside a TPPWG. We adapt the air bias coherent detection (ABCD) technique and apply it to a TPPWG in order to image the THz electric field distribution inside the waveguide along the propagation direction without disturbing the propagation of the guided THz wave. As an application of the method we demonstrate the direct measurements of the reflection coefficient for the THz wave at the end of the waveguide. In the next part of the chapter we investigate field enhancement properties of the TPPWG. We show that THz peak electric field exceeding 1.4 MV/cm can be obtained. That high values of electric field open exciting possibilities of investigating THz nonlinear processes.

4.1 Terahertz waveguides

The majority of THz systems are based on free space propagation of THz transients. At the same time THz waveguides show significant potential in many applications, including THz based sensors [161], THz communication [17, 162] and subwavelength imaging [163]. Development of waveguides for terahertz waves is motivated by the necessity of remote delivery of broad band terahertz radiation from a terahertz source to the point of interaction with the sample. The main challenge the THz field is facing, is a high loss in most structures; which is caused by either absorption losses in the material or conduction losses for the structures incorporating metals.

Variety of realized and proposed structures is very rich. So far the most investigated structure for guiding THz waves is a parallel plate waveguide, which in detail will be described in the next section of this chapter.

To other metal structures allowing for THz propagation one can account single [164–166] or double [167] metal wires, hollow circular and rectangular metal waveguides [168, 169] or metallic slit waveguides [170]. THz propagation on a metal surfaces in a form of Zennek surface waves has been also demonstrated [171, 172]. A next big class of THz waveguides are THz fibers, which include crystalline solid core fibers [173], polymer solid core fibers [174, 175] and hollow core photonic crystal fibers [176–178] and air-clad porous fiber with sub-wavelength features in the core [179]. Losses in those structures vary from tens of dB/cm for dielectric slab waveguides [180] and metal hollow core waveguides [168] to few dB/m for metal wires with plasmon mediated guidance [164]. Losses depend highly on the designed structure, but the general tendency is that the tighter the confinement the higher losses.

4.2 Parallel plate waveguides

Fig. 4.1(a) shows the simple geometry of the parallel plate waveguide (PPWG). PPWG consists of two conducting plates separated by a set distance b and forming in this way a waveguide. Many variations of this structure have been designed during years. Usually conducting plates are made of a well conducting bulk metals (mainly copper and aluminum), but constructions where plates are formed by thin evaporated metal [181] or by transparent conducting oxide like fluorinated tin oxide (FTO) [182] have been also used. The volume between the space can be filled with dielectric [161, 183] or left empty, depending on the purpose of the waveguide.

For the electric field polarized along y-direction and propagating in the z-direction only transverse magnetic (TM) modes can exist. If the plates are formed out of perfect conductor, the non-vanishing terms of the field

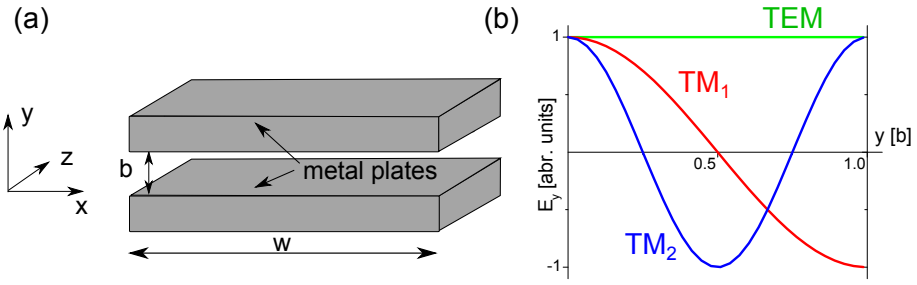

FIGURE 4.1: (a) Schematic of the parallel plate waveguide. (b) Mode profiles of the first three modes in PPWG.

components are [184]:

$$H_x(y,z) = A_m \cos\left(\frac{m\pi}{b}y\right) e^{-i\beta_z z}, \tag{4.1}$$

$$E_y(y,z) = -\frac{A_m \beta_z}{\omega_0 \epsilon} \cos\left(\frac{m\pi}{b}y\right) e^{-i\beta_z z}, \tag{4.2}$$

$$E_z(y,z) = \frac{A_m}{i\omega_0 \epsilon}\left(\frac{m\pi}{b}\right) \sin\left(\frac{m\pi}{b}y\right) e^{-i\beta_z z}, \tag{4.3}$$

$$\text{and } \beta_z^2 + \left(\frac{m\pi}{b}\right)^2 = \beta_0 = \omega_0^2 \mu\varepsilon, \tag{4.4}$$

where $m = 0, 1, 2, ...$ is the order of the TM mode, $0 \leq y \leq b$, A_m is the field amplitude, ω_0 is THz wave angular frequency, μ and ε are magnetic permeability and dielectric permittivity of the medium filling waveguide. The cut-off frequencies are given by

$$f_m = \frac{mc}{2b\sqrt{\mu\varepsilon}}, \tag{4.5}$$

where c is the speed of light. The lowest order TM_0 mode is in fact TEM mode. It has no cut-off frequency and for perfectly conducting plates, it is dispersionless, meaning that phase and group velocity of the whole structure are equal to the phase and group velocity of the filling dielectric.

Fig 4.1(b) shows mode profiles of the first three TM modes in PPWG. Modes have spatial dependence of $\cos(m\pi y/b)$. This dependence results

in a uniform field profile for the TEM mode, odd profile for TM_1 and even for TM_2 mode. It is important to note that all the modes are orthogonal to each other. That implies that any field distribution can be expressed as a superposition of waveguide modes. That allows for easy calculation of coupling coefficients of incoming field into the waveguide modes. For example Gaussian beam, which has a even symmetry, will excite only even modes (TEM, TM_2, TM_4) and the coupling coefficients will be given by overlap integrals. Presented theory predicts that for infinitely wide PPWGs mode profiles have no frequency dependance. That is due to the strong boundary conditions at the conductor-dielectric interfaces. Recently it has been experimentally shown that finite-width PPWGs with real (not perfect) metals exhibit transition frequency above which TEM-like mode changes its field profile and propagates as a plasmonic mode [160].

The propagation losses in a ideal PPWG come from two sources: conduction losses from currents in metal plates and dielectric losses from the medium filling the waveguide. In case of the PPWG filled with dry air/nitrogen the second type of losses is obviously vanishing. The first type of losses arises from the finite conductivity of the metal. The THz field after propagating for distance L along the waveguide is attenuated by factor $e^{-\alpha L/2}$. The attenuation constant α for the TEM mode coming from the Ohmic losses can be expressed by [185]

$$\alpha = \frac{2nR_s}{Z_0 b} \tag{4.6}$$

where $R_s = \sqrt{\pi f \mu/\sigma}$ is a surface resistivity, n is the refractive index of the material filling waveguide, Z_0 free space impedance and σ the conductivity of the metal. From this equation two important observations are seen. First of all losses of the TEM mode in the PPWG depend inversely proportionally on the plate separation b, and secondly they increase with frequency as a square root. This situation is different for higher order modes, where Ohmic losses for frequencies above cut-off are decreasing [151].

4.3 Air bias coherent detection

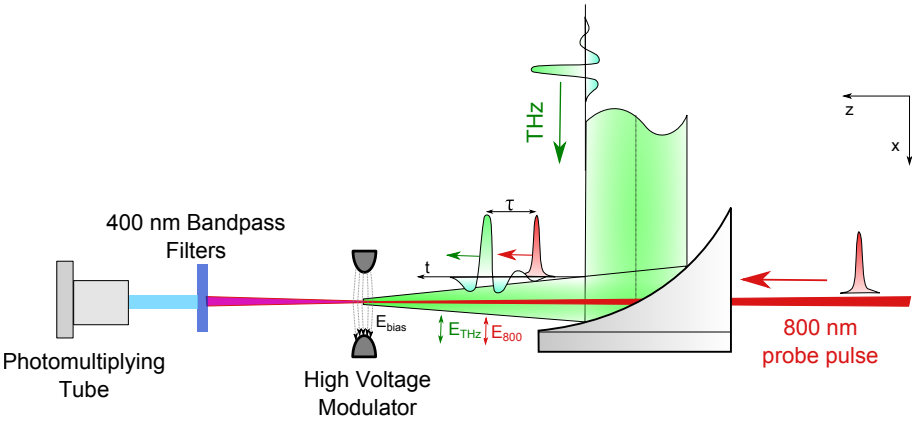

FIGURE 4.2: Schematic diagram of air bias coherent detection.

Coherent detection of THz radiation is based on the interaction between the laser pulse I_ω and the THz electric field E_{THz} in the presence of the external oscillating electric field E_{bias} [34]. Figure 4.2 shows a simple geometry of the air bias coherent detection (ABCD) setup. By focusing the terahertz pulse with a probe fundamental (ω) beam without addition of external bias, an optical field at second harmonic (2ω) is emitted:

$$E_{2\omega}\left(\vec{r},t\right) \propto \chi^{(3)}_{xxxx} E_{THz}\left(\vec{r},t\right) E_{\omega}\left(\vec{r},t\right) E_{\omega}\left(\vec{r},t\right), \tag{4.7}$$

where $\chi^{(3)}_{xxxx}$ is the third-order nonlinear susceptibility of the gas. All the fields on the Fig. 4.2 are polarized along x-direction. For the moment lets consider interaction only at one point $(\vec{r},t)$ and omit time-space coordinates. Since $E_{2\omega} \propto E_{THz} E_\omega E_\omega$, the intensity of the second harmonic is proportional to the intensity of the THz wave $I_{2\omega} \propto I_{THz}$. The signal measured in this way is incoherent, and its applications are limited. To realize coherent detection, external ac bias field with amplitude E_{bias} is added at the point of the optical focus. The phase of the external field relative to the THz pulse trains is oscillating from 0° to 180° with every other THz pulse, changing in this way direction of the bias

field. The external ac bias together with fundamental beam generates second harmonic pulse with field amplitude $E_{2\omega}^{LO} \propto \chi^{(3)} I_\omega E_{bias}$, which mixes with terahertz induced second harmonic $E_{2\omega}^{THz} \propto \chi^{(3)} I_\omega E_{THz}$. The total second-harmonic intensity has a form

$$I_{2\omega} \propto \left(E_{2\omega}^{THz} \pm E_{2\omega}^{LO}\right)^2 = \left(E_{2\omega}^{THz}\right)^2 \pm 2E_{2\omega}^{THz} E_{2\omega}^{LO} + \left(E_{2\omega}^{LO}\right)^2, \quad (4.8)$$

where we assume that E_{bias} is constant during the interaction time between the THz transient and the probe pulse, and what can be also written as

$$I_{2\omega} \propto \left(\chi^{(3)} I_\omega\right)^2 \left[E_{THz}^2 \pm 2E_{bias} E_{THz} + E_{bias}^2\right]. \quad (4.9)$$

Due to the phase modulation of the bias field between 0° to 180°, lock-in detection can easily isolate the cross-term. The amplitude of second harmonic intensity measured by the lock-in amplifier locked to the oscillation frequency of the high voltage modulator is equal to

$$I_{2\omega} \propto 4 \left[\chi^{(3)} I_\omega\right]^2 E_{bias} E_{THz}. \quad (4.10)$$

By changing the THz-probe time delay τ the full THz waveform can be mapped out. Since the detection of the THz radiation occurs in a nearly non-absorbing and non-dispersive medium, the spectrum is only limited by the properties of the laser probing pulse. In contrast to the free space electrooptic sampling in crystals, the measured spectrum is not disturbed by crystal phonon modes and accurately corresponds to the spectrum of the incident THz pulse. More over the acquired waveform does not suffer from reflections in the crystal and the spectral resolution can be increased by increasing the length of the measurement time window. The optimal intensity of the probe beam is such that it does not cause creation of plasma, what would lead to a white light generation and result in increased noise measured by the photomultiplier tube. On the other hand, it has been shown that for very high probe intensities ($\gg 6 \cdot 10^{14}$ W/cm^2) the generated second harmonic (SH) can act as a local oscillating field, so coherent detection is possible without

need external ac bias [32]. However this method is characterized by much poorer signal to noise ratio. THz detection in other gases than just air has been investigated and it has been found out that the THz ABCD detection in xenon can be more efficient [186]. Further more by applying balance detection signal to noise ratio of ADCD scheme can be improved [101].

4.4 Imaging terahertz field inside parallel plate waveguide

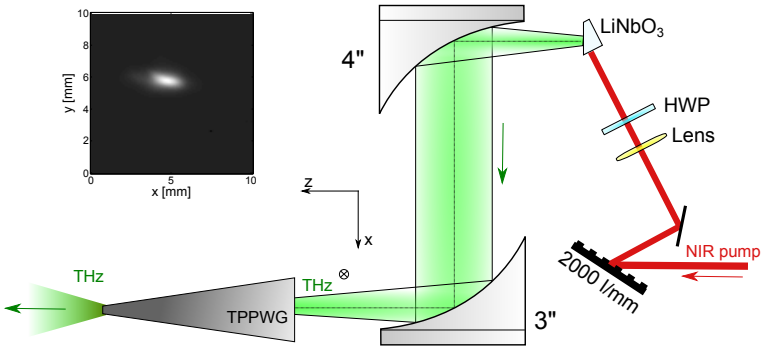

FIGURE 4.3: Schematic of THz generation and coupling to the tapered parallel plate waveguide. THz radiation is generated using tilted wavefront method in $LiNbO_3$. A pair of 4" and 3" off-axis parabolic mirrors is used to couple THz into the TPPWG. Inset shows THz spot at the input to the TPPWG measured using pyroelectric detector with a 250 μm-diameter aperture has elliptical shape with FWHMs intensity of 1.6 mm along x-direction and 0.7 mm along y-direction. HWP - half wave plate.

Here we present a novel non-invasive method for characterization of the propagating electric transients inside a tapered parallel plate waveguide (TPPWG). For this purpose we adapt previously described ABCD technique and apply it to a TPPWG in order to image the THz electric field distribution inside the waveguide along the propagation direction. This

method does not disturb the propagating THz field. In a closer detail we look at the influence of the cross-directional propagation.

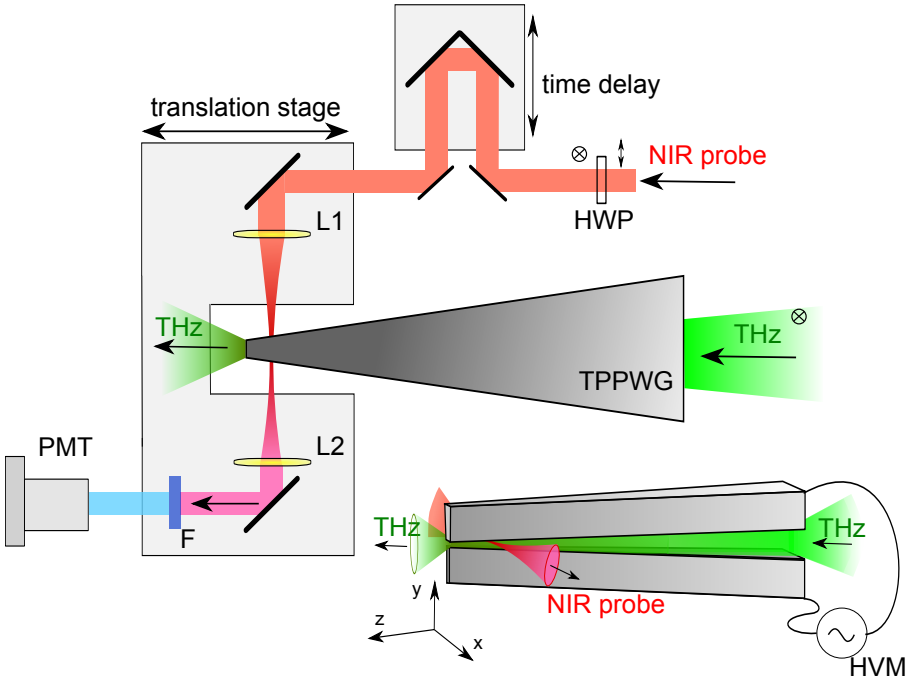

FIGURE 4.4: Schematic of the air photonic setup for non-invasive field imaging inside a tapered parallel plate waveguide. THz radiation is coupled into the TPPWG, propagates along it and then interacts with NIR probe inducing second harmonic generation in the presence of oscillating local electric bias field. L1, L2 - lenses, F - 400 nm bandpass filter, HVM - high voltage modulator, PMT - photomultiplying tube, HWP - half wave plate.

Figures 4.3 and 4.4 show the schematics of the experimental setup. The TPPWG consists of two electrically isolated, fine polished aluminum plates of varying width (input 3 mm, output 49 μm) and a varying plate separation. The input plate separation to the waveguide is set to 1 mm, while the output plate separation can be varied between 0μm and 500

μm by help of a micrometric stage. Aluminum was chosen as a material for metal plates because of its combination of high conductivity and hardness, that is needed for low loss propagation and possibility of manufacturing narrow tips. The total length of the TPPWG is 25.4 mm. A high voltage modulator (HVM) delivering $\pm$100 V at 500 Hz (synchronized with first subharmonic of the laser repetition rate) is connected to the waveguide plates. The applied voltage results in an electric bias field of $\pm$5 kV/cm at the point of the narrowest gap between metal plates for 200 μm plate separation. Broadband THz pulses are generated by tilted pulsefront optical rectification in $LiNbO_3$ (described in chapter 2.2.2) using near-infrared (NIR) 0.6 mJ pump pulse from a 1 kHz, 90 fs, 800 nm regenerative Ti:sapphire femtosecond laser amplifier (Spectra-Physics Hurricane). The intensity front of fs pulses is tilted by a 2000 line/mm holographic grating and imaged by a 63 mm-focal length lens with demagnification factor of 2 onto the front surface of a stoichiometric $LiNbO_3$ crystal at room temperature. THz pulse energies up to 0.5 μJ measured directly after the $LiNbO_3$ were obtained. Pair of 50.8 mm-diameter, 101.6 mm- and 76.2 mm-focal length off-axis parabolic mirror is used to collimate and focus THz radiation at the input to the TPPWG. A pyroelectric detector with a 0.25 mm-diameter aperture mounted on a x-y motorized translation stage was used to image THz field intensity at the input to the waveguide. The THz beam has an elliptical shape, shown in the inset to the Fig. 4.3, with intensity FWHMs of 1.6 mm along x-direction and 0.7 mm along y-direction. The THz wave couples into the TPPWG, propagates between the aluminium plates in a TEM mode and then couples out into the free space at the narrow end of the waveguide. A NIR beam from the same laser is used for probing the THz field between the plates of the waveguide. The probe beam is focused in the center of the volume between the plates with a 19 mm-focal length lens (L1) and recollimated after the waveguide with lens L2. The beam waist at the focus point has been estimated to be 6.5 μm and the Rayleigh range is 41 μm. The highest NIR pulse energy limited to 18 μJ in order to avoid ionization of the air. This part of the setup is

mounted on a translation stage, that enables scanning along the waveguide (z- direction). The beam is sent through 400 nm bandpass filters to a photomultiplier tube (PMT) which detects the 400-nm light generated in the ABCD process. The signal from the PMT is measured by a lock-in amplifier referenced to HVM modulation frequency. The polarizations of the four interacting electric fields (terahertz, fundamental, second harmonic and bias) are perpendicular to the waveguide plates.

In the standard ABCD configuration the probe pulse and the THz transient propagate collinearly through the area of a bias field. For a given THz-probe delay time τ, each point of the NIR probe interacts with the same part of a THz waveform through out the whole interaction length. Thus the detected second harmonic intensity $I_{2\omega}(\tau)$ is proportional to the time convolution between the THz waveform $E_{THz}(t)$ and the square of probe intensity $I_{\omega}^{2}(t)$:

$$I_{2\omega}(\tau) \propto E_{bias} \int E_{THz}(t)\, I_{\omega}^{2}(\tau - t)\, dt. \tag{4.11}$$

In our configuration the THz transient and the probe pulse propagate in perpendicular directions. In this case for a given THz-probe delay time τ, each point of the NIR probe interacts with a moving THz waveform and the intensity $I_{2\omega}(\tau)$ of the generated SH is expressed as:

$$I_{2\omega}(\tau) \propto \int E_{bias}(\vec{r}) \left(\int E_{THz}(t, \vec{r})\, I_{\omega}^{2}(t + \tau, \vec{r})\, dt \right) d^{3}\vec{r}. \tag{4.12}$$

In the above equation the inner integral is a temporal cross-correlation between the THz transient and the square of the probe beam intensity at the space point $\vec{r}$, while the outer integral sums contributions from each point of the interaction volume.

We now consider our case of a 800 nm, 90 fs-long NIR pulse in a focused Gaussian beam of waist 6.5 μm and a Rayleigh range of 41 μm. The beam is focused in a uniform THz field restrained to a volume of thickness L_x (inset in Fig. 4.5(a)). The maximum induced SH $I_{2\omega max}$ as a

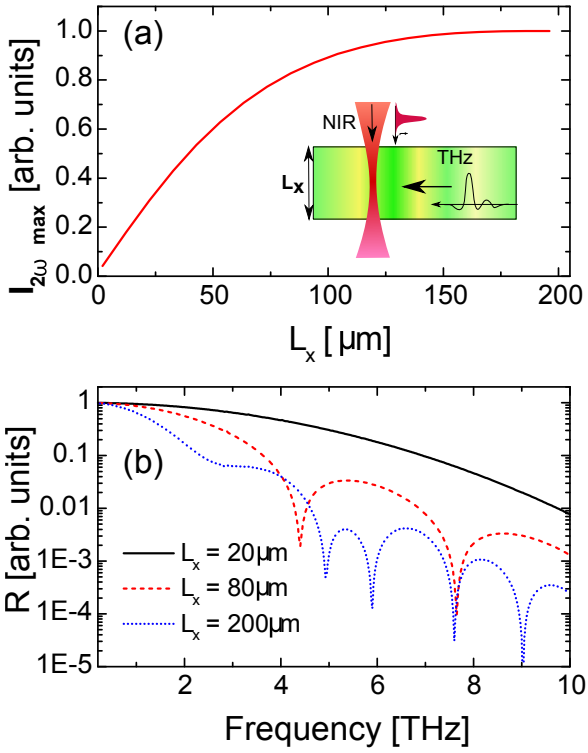

FIGURE 4.5: (a) Normalized maximum second harmonic intensity $I_{2\omega}$ as a function of interaction length L_x between fundamental and THz beams. The 800 nm beam waist at the focus point has been calculated to be 6.5 μm and the Rayleigh range is 41 μm, pulse duration 90 fs. Inset presents considered geometry. (b) Normalized response function $R(f)$ for $L_x = 20\mu$m, 80μm and 200μm.

function of L_x calculated with Eq. 4.12 is shown in Fig. 4.5(a). Single-cycle THz transient with frequency components in the range 0.05 - 3.0 THz was used for the calculations. For L_x shorter than the Rayleigh range the interaction length between the THz wave and the probe is defined by L_x. In the opposite limit of L_x longer than the Rayleigh range $I_{2\omega}$ saturates. The interaction length is limited by the geometrical dimensions of the focus of the probe beam, as indicated by the quadratic

dependence of I_ω in Eq. 4.12. This is valid as long as the wavelength of the highest frequency components within the THz transient is shorter than the Rayleigh range of the probe beam. The response function $R(f) = I_{2\omega}(f)/E_{THz}(f)$, which describes the spectral response, has been evaluated for different widths of the THz region as shown in Fig. 4.5(b). For small L_x the response function is monotonously decreasing with frequency. For larger L_x the effects of positive and negative part of THz waveform can interfere leading to sharp dips in the response.

In Fig. 4.6(a) we show a 2D map of THz induced SH $I_{2\omega}(\tau, z)$ as a function of the THz transient-probe delay time τ for different positions z of the probe beam along the waveguide can be obtained. Two THz transients are visible in the plot: the first transient, centered at 5 ps time delay, is the incident pulse propagating inside the waveguide. The second transient, propagating in the opposite direction, originates from the reflection at the waveguide end (position $z = 0$ mm) due to the impedance mismatch between the waveguide ($z < 0$) and free space ($z > 0$). Values of $I_{2\omega}(t, z)$ for $z < 0$ has been corrected for the local bias field $E_{bias}(z)$, which changes with the plate separation. We have to note that for $z > 0$ (outside the waveguide) the bias electric field quickly decays which leads to vanishing $I_{2\omega}(t, z)$. Fig. 4.6(b) shows the retrieved and simulated peak value of THz electric field as a function of NIR probe position z along the waveguide. To calculate $E_{THz}(t, z)$ the values of $I_{2\omega}(t, z)$ have been corrected using the width of metal plates (and correspondingly by the interaction length $L_x(z)$) according to the dependence from Fig. 4.5(a). The time-domain numerical simulation was performed with CST Microwave Studio for a TPPWG made of aluminium treated as a lossy metal with conductivity of $\sigma = 3.56 \cdot 10^7$ S/m [187]. The simulation agrees well with the measurement except for $z > 0$ where the fast decrease in the measured value is caused by the rapid decay of E_{bias} outside the waveguide. The dip at $z = -0.15$ mm has its origins in the interference between incident and reflected wave. The shape of the TPPWG structure can cause field enhancement in the proximity of the waveguide edges (propagating THz edge

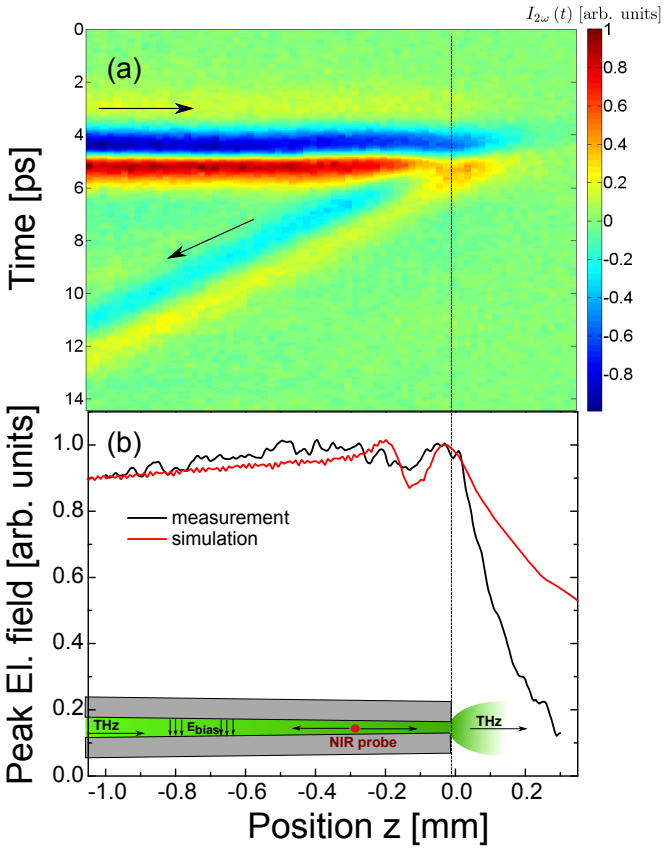

FIGURE 4.6: (a) 2D map of THz induced second harmonic $I_{2\omega}(t)$ as a function of THz wave-probe delay time for different positions of the probe beam along the waveguide. Values of $I_{2\omega}(t)$ have been corrected for the bias field. (b) Measured and simulated integrated peak THz electric field across the waveguide as a function of NIR probe position z.

plasmons)[158], while the calculated value of $E_{THz}(t, z)$ is an integrated value of the THz electric field along the probe direction within the interaction volume. If additional freedom of the scanning stage movement along directions x and y is available, then edge enhancement effects

can also be investigated using our method, with a transverse resolution determined by the Rayleigh range of the probe beam.

Fig. 4.7 shows measured frequency dependent amplitude reflection coefficient $\Gamma(f) = E_{\mathtt{refl}}(f)/E_{\mathtt{inc}}(f)$ of the waveguide end together with the result of a numerical simulation. For a good temporal separation between the incident and reflected pulses, the data (shown at the inset to the Fig. 4.7) is taken at a point $z = -0.9$ mm from the waveguide end. That implies that the presented reflection coefficient Γ includes not only reflection but also propagation effects, such as ohmic losses and wave scattering, which will lead to additional reduction of the amplitude of the reflected field. The reflection of the THz wave is caused by impedance mismatch between free space $Z_0 = 377\Omega$ and the waveguide $Z_{\mathtt{PPWG}} = \sqrt{(R + i\omega L)/(G + i\omega C)}$, where R, L, G, C are correspondingly distributed resistance, inductance, conductance and capacitance of the waveguide. We observe that the reflection coefficient $\Gamma = (Z_{\mathtt{PPWG}} - Z_0)/(Z_{\mathtt{PPWG}} + Z_0)$ decreases with increasing THz frequency, as it is expected since short waves are easier to squeeze through subwavelength gap. We find good agreement between measurement and simulation in the frequency range 0.1 - 0.5 THz. At higher frequencies the measured reflection coefficient Γ is smaller than theoretically predicted. This can be caused by the increased wave scattering (especially important at higher frequencies and at interfaces) [188] and increased ohmic losses at higher frequencies.

4.5 Field enhancement inside tapered parallel plate waveguide

Figure 4.8 shows the output intensity distributions of the THz electric field measured using a pyroelectric detector with a 0.25 mm-diameter aperture placed 0.8 mm away from the waveguide tip for output gaps of 0 μm, 20 μm and 200 μm with the input gap $B_{in} = 1$ mm. For the closed waveguide no THz field is transmitted directly through the

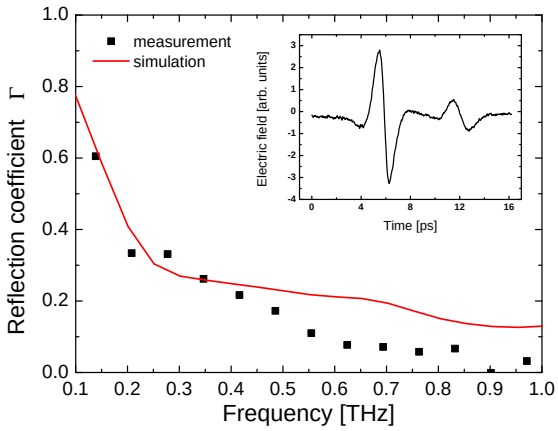

FIGURE 4.7: Measured and simulated frequency dependent amplitude reflection coefficient Γ of the waveguide end. Waveform from point $z = -0.9$ mm shown in the inset.

output. However we are able to observe THz waves that leaked around the tip - blurred halo around the center of the scan. The vertical lines visible on the picture come from the THz waves that propagate on the outside vertical walls of the waveguide. For the open gaps the majority of the THz wave propagates through the gap and dominates the pictures. Those strong burst of THz radiation, even for output gaps that are over one order of magnitude smaller than the THz wavelength, indicate that high THz intensities are focused below diffraction limit. This subwavelength energy concentration opens possibility of strong field enhancement which will be discussed below.

First we will try to estimate in an analytical manner the field enhancement at the output of the waveguide. Lets consider 1D-tapered infinitely wide PPWG with THz wave propagating as a TEM mode. In the case of PPWG tapered in the y-direction, the plate spacing b is a function of

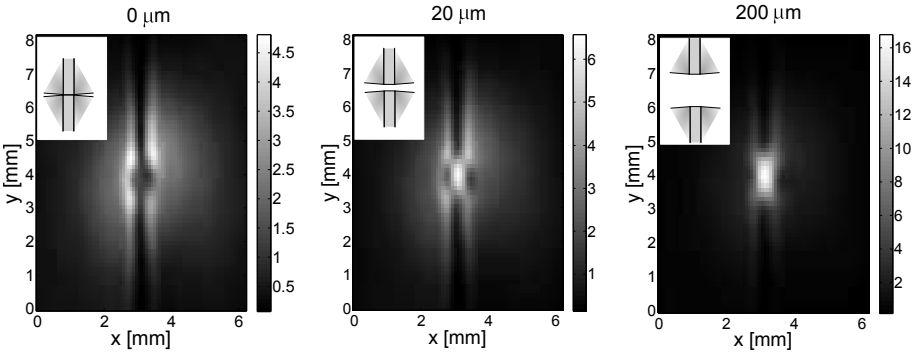

FIGURE 4.8: Output intensity distributions measured using pyroelectric detector with a 0.25 mm-diameter aperture placed 0.8 mm away from the waveguide tip for output gaps B_{out} of 0 μm, 20 μm and 200 μm. $B_{in} = 1$ mm.

the position z along the waveguide

$$b(z) = B_{in} - \frac{B_{in} - B_{out}}{L_{\mathrm{WG}}} z, \tag{4.13}$$

where B_{in} and B_{out} are plate separations at the input and output to the waveguide, L_{WG} is the total length of the waveguide. As a result the attenuation constant, expressed by Eq. 4.6, is also a function of position along the waveguide

$$\alpha(z) = \frac{2R_s}{Z_0 b(z)} = \frac{2R_s}{Z_0 \left(B_{in} - \frac{B_{in}-B_{out}}{L_{\mathrm{WG}}} z\right)}, \tag{4.14}$$

where $R_s = \sqrt{\pi f \mu / \sigma}$ is the surface resistivity. The differential equation for the field amplitude along the waveguide is of the form:

$$dE = E(z + dz) - E(z) = -\frac{\alpha(z)}{2} E(z)\, dz, \tag{4.15}$$

$$\frac{dE}{E} = -\frac{R_s}{Z_0 \left(B_{in} - \frac{B_{in}-B_{out}}{L_{\mathrm{WG}}} z\right)} dz. \tag{4.16}$$

By integrating both sides of above equation, the electric field as a function of position inside the waveguide is found in a form

$$E(z) = E_0 \left[1 - \left(1 - \frac{B_{out}}{B_{in}}\right) \frac{z}{L_{\mathrm{WG}}}\right]^{\frac{R_s}{Z_0} \frac{L_{\mathrm{WG}}}{B_{in} - B_{out}}}. \tag{4.17}$$

The field reduction *FR* at the output to the waveguide due to Ohmic attenuation is equal to:

$$\mathrm{FR} = \frac{E(z = L_{\mathrm{WG}})}{E_0} = \left[\frac{B_{out}}{B_{in}}\right]^{\frac{\sqrt{\pi f \mu/\sigma}}{Z_0} \frac{L_{\mathrm{WG}}}{B_{in} - B_{out}}}. \tag{4.18}$$

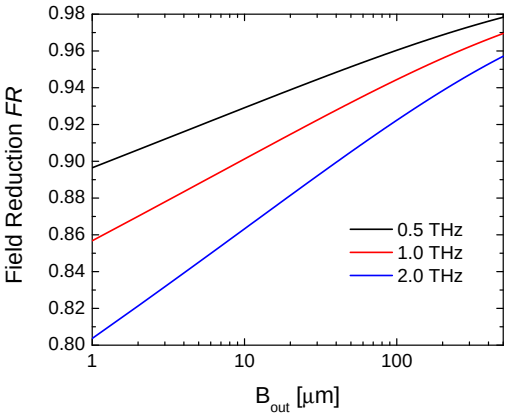

FIGURE 4.9: Calculated field reduction FR due to Ohmic losses at the output of a 1D-tapered PPWG as a function of the output gap B_{out} for 0.5, 1.0 and 2.0 THz. Data for input plate spacing $B_{in} = 1000\mu$m, the total length of the waveguide $L_{\mathrm{WG}} = 25.4$ mm and conductivity of the metal $\sigma = 3.56 \cdot 10^7$ S/m.

Figure 4.9 shows the calculated field reduction *FR* at the output of a 1D-tapered PPWG as a function of the output gap B_{out} for the field frequencies of 0.5, 1.0 and 2.0 THz. Lines are calculated using Eq. 4.18, where the conductivity of aluminum was set to $\sigma = 3.56 \cdot 10^7$ S/m [187], input plate spacing $B_{in} = 1000$ μm, and the total length of the

waveguide $L_{\mathrm{WG}} = 25.4$ mm. It can be seen on the figure that the field reduction depends strongly on the output plate separation B_{out}, in a way that the larger the plate separation the smaller the losses. Hence the attenuation coefficient α increases with the frequency of the propagating THz field as a $\sqrt{f}$, and therefore the field reduction FR is also frequency dependent.

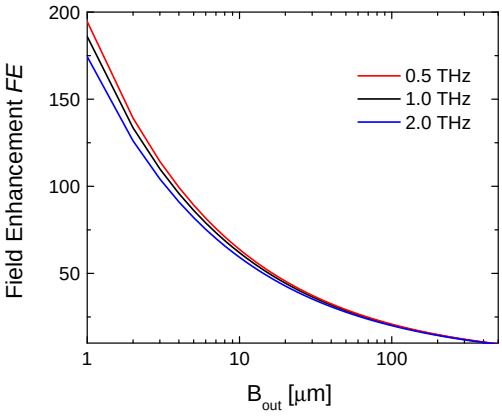

FIGURE 4.10: Calculated field enhancement FE at the output of a 2D-tapered PPWG as a function of the output gap B_{out} for 0.5, 1.0 and 2.0 THz. The field enhancement is achieved by energy squeezing in the area between metal plates. Data for $B_{in} = 1000\mu$m, $W_{in} = 3000\mu$m, $W_{out} = 49\mu$m, $L_{\mathrm{WG}} = 25.4$ mm and conductivity of the metal $\sigma = 3.56 \cdot 10^7$ S/m.

The analytical calculation of field reduction FR, which is presented above, is only an indication of the average Ohmic loss along a PPWG tapered in one direction, and does not include the fact that the THz energy of a THz wave is getting squeezed to a smaller area. The TPPWG investigated in this thesis has two-dimensional tapering in directions perpendicular to the propagation of THz wave. Now we will assume that a THz wave, which is uniformly distributed across input facet, is confined within the volume between metal plates. That is the transmitted total power is constant: $E^2(z)\, A(z) / Z_{WG}(z) = \mathrm{const}$, where $A(z)$ is a

cross-sectional area and $Z_{WG}(z)$ is impedance of the waveguide at the position z. Neglecting changes of impedance along the waveguide (what is reasonable since $Z_{in} \approx 126\ \Omega$ and $Z_{out} \approx 153\ \Omega$ for $B_{out} = 20\ \mu$m, calculated using $Z_{WG} = 120\pi b/w$) [189]), one can present the field enhancement as the product of the field reduction FR and the geometrical factor $\sqrt{\frac{A_{out}}{A_{in}}}$:

$$\mathrm{FE} = C\sqrt{\frac{A_{out}}{A_{in}}}\mathrm{FR}, \tag{4.19}$$

$$\mathrm{FE} = C\sqrt{\frac{W_{out}}{W_{in}}\frac{B_{out}}{B_{in}}}\left[\frac{B_{out}}{B_{in}}\right]^{\frac{\sqrt{\pi f\mu/\sigma}}{Z_0}\frac{L_{\mathrm{WG}}}{B_{in}-B_{out}}}, \tag{4.20}$$

where A_{in}, A_{out}, W_{in} and W_{out} are correspondingly the input and the output area and the width of the TPPWG. C is the coupling coefficient of the Gaussian input excitation beam E_G and the uniform field distribution E_U of the TEM eigen mode of the TPPWG at the its input. The constant C can be calculated using the mode overlap integral [190]:

$$C = \frac{\left|\int E_G E_U^* dA\right|}{\sqrt{\int |E_G|^2\, dA}\sqrt{\int |E_U|^2\, dA}}. \tag{4.21}$$

We note that an overlap integral as given above is useful for calculating mode amplitudes. For many situations, such as coupling of optical power into a mode, the square of the overlap integral is relevant. The coupling constant C between the Gaussian input excitation mode and uniform field distribution of the TEM mode for 1 mm plate spacing has been calculated to be 0.877. Figure 4.10 shows calculated field enhancement *FE* at the output of a TPPWG. In the figure we can see that the field enhancement increases with decreasing output plate separation. Values above 45 are achieved for B_{out} smaller than 20 μm. The presented calculations do not account for diffraction losses nor reflection from the non-perfect impedance matching, and because of that the actual values of FE will be lower. The argumentat does not take into account either that the mode profile may depend on the plate width and separation,

neither that the absorption constant may be different for finite width PPWG.

The time-domain numerical simulations are performed with CST Microwave Studio for a full size TPPWG made of aluminium treated as a lossy metal. The TPPWG is divided into $40 \cdot 10^6$ mesh cells. Perfectly matched layer (PML) boundary conditions are used. Simulations are performed on a 12-core processor computer workstation with 48GB of memory and take ~ 4.5 hours of computing time each. The THz beam at the input to the waveguide has shape close to elliptical Gaussian, with FWHM in intensity of 1.6 mm along x-direction and 0.7 mm along y-direction. Figure 4.11 shows the peak electric field at the central point between metal plates along the TPPWG for output gaps B_{out} of 20, 40, 60, 100, 140 and 200 μm. The electric field is normalized to the maximum of Gaussian field at the input to the waveguide. The input to the waveguide is at $z = -25.4$ mm and the output at $z = 0.0$ mm. During the first 7 mm of the waveguide the THz peak electric field oscillates. Those changes are caused by mode fitting between Gaussian mode and TEM mode. In the last 18 mm of the waveguide gradual increase of the peak THz electric field happens. Field enhancement higher than a factor of 20 is achieved for the output gap of 20 μm. At $z = 0$ THz field couples out of the TPPWG, and for $z > 0$ the peak electric field decreases due to strong diffraction. The smaller the output gap the bigger the diffraction angle in the vertical direction and the faster the decrease of the peak electric field. Also the reflection coefficient is larger for smaller gaps, so less energy couples out when B_{out} is narrow.

Figure 4.12 shows the calculated distributions of the y-component of the peak THz electric field along the TPPWG for a few chosen positions z. The field at the input ($z = -25.1$ mm) of the waveguide has an elliptical gaussian distribution. The general trend visible from presented field distribution is that the majority of the energy of the THz field is confined within the area between metal plates. The confinement is tighter the closer the metal plates are. At the position of $z = -9.1$ mm the field has a distribution more resembling the uniform field distribution of the TEM

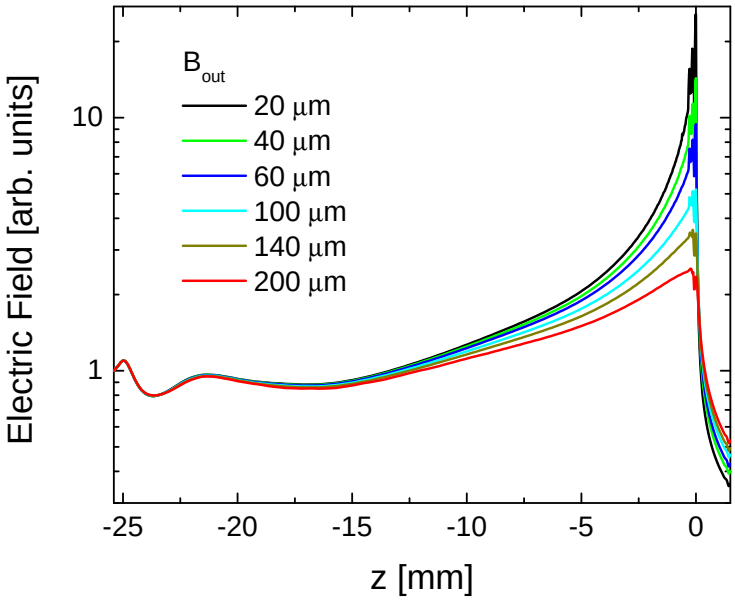

FIGURE 4.11: Simulated peak electric field along the TPPWG for output gaps B_{out} of 20, 40, 60, 100, 140 and 200 μm. Electric field is normalized to the field at the input to the waveguide. Field values for the center points between plates. Input to the waveguide is at $z = -25.4$ mm and the output at $z = 0.0$ mm. Data for $B_{in} = 1000$ μm, $W_{in} = 3000$ μm, $W_{out} = 49$ μm, $L_{\mathrm{WG}} = 25.4$ mm and conductivity of the metal $\sigma = 3.56 \cdot 10^7$ S/m.

mode, with exception of proximity to edges of the waveguide, where it is enhanced. This effect has been previously reported by Zhan *et al.* [157], and can be explained by the presence of THz propagating edge plasmon. Once the THz transient couples out of the TPPWG the THz beam rapidly diffracts. In Fig. 4.12(j) a blurred halo around the center of the image and the vertical lines that come from the THz waves that propagate on the outside vertical walls of the waveguide are visible, what is in agreement with measurements shown at Fig. 4.8(a) and (b).

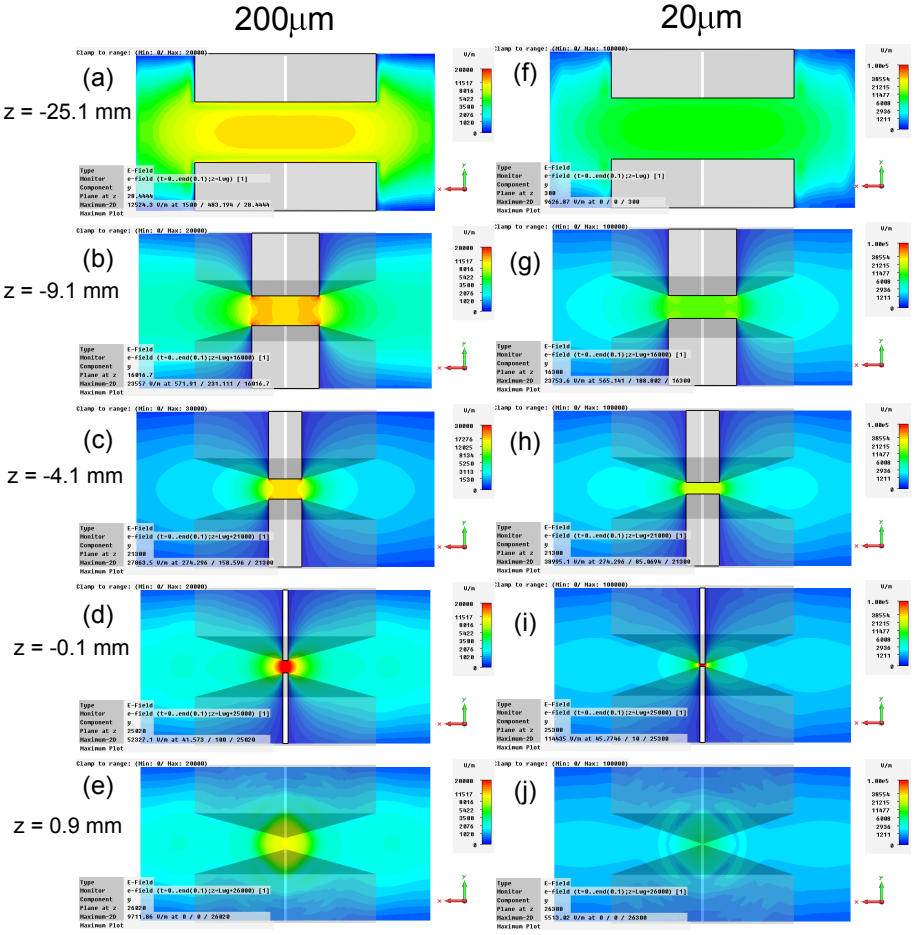

FIGURE 4.12: Distributions of the y-component of the peak THz electric field along the TPPWG for B_{out} of (a-e) 200 μm and (f-j) 20 μm at positions along the waveguide z = -25.1, -9.1, -4.1, -0.1 and 0.9 mm. Note that scales in the left and right column are different (left column range is 0 to 20000 V/m, while for the right column has range from 0 to 100000 V/m).

Figure 4.13 shows the ratio between THz field enhancement simulated using CST Microwave Studio FE_{sim} and calculated in analytical manner FE_{an} using Eq. 4.20 at the output of the TPPWG for different sizes of the output gap B_{out}. The main difference between FE_{sim} and FE_{an} is that the second one does not account for wave diffraction in the x-direction, so $\frac{\mathrm{FE}_{sim}}{\mathrm{FE}_{an}}$ is a good representation of diffraction losses. It is clear that diffraction losses increase with increasing output gap separation. This effect can be explained using the contrast between effective waveguide impedance Z_{WG} and a free space impedance Z_0. Narrowing plate separation increases effective waveguide impedance Z_{WG}. Higher contrast between Z_{WG} and Z_0 leads to higher reflection coefficient in the x-direction, which means that the THz wave is tighter confined within the waveguide. This effect is analogous to solid core optical fibers, where high contrast in refractive index gives tight confinement of the optical wave. A single exponential decay has been fitted to the data points in Fig. 4.13 with parameters shown in the figure. The agreement between data points and the exponential decay is very good. The long distance limit of $\frac{\mathrm{FE}_{sim}}{\mathrm{FE}_{an}}$ ($B_{out} \to \infty$) fit is 0.174 ± 0.011. This result is in agreement with work of Zhan *et al.* [157], who has experimentally showed that the field confinement in the area between plates of a PPWG decreases exponentially with increasing plate separation.

To experimentally verify THz field enhancement by TPPWG two methods are used. The first method is to detect THz radiation using free space electro-optic sampling outside the TPPWG and then to use outcoupling coefficients, delivered by numerical simulation, to compute fields at the output of the waveguide. The second method is based on detection of THz induced second harmonic and is similar to the ABCD method.

Figure 4.14 show a schematic of the free space electro-optic setup for detection of the THz field at the output of the tapered parallel plate waveguide. NIR probe pulses from the same laser amplifier are focused using a 50 mm-focal length lens onto 300 μm-thick [110] GaP crystal. Part of the NIR probe enters the GaP crystal and is reflected from the back surface of the electro-optic crystal and copropagates with THz radiation.

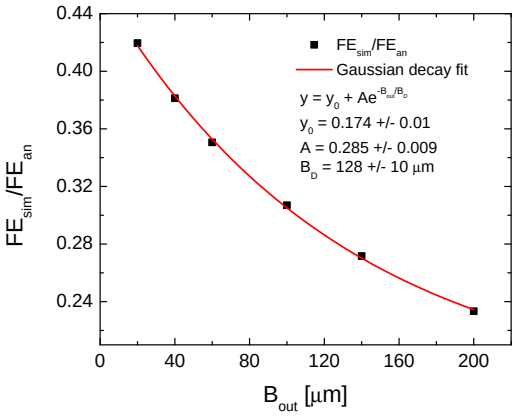

FIGURE 4.13: Calculated diffraction losses in a TPPWG as a function of the output gap B_{out} for THz wave at 1.0 THz. Solid line shows exponential decay fit. Data for $B_{in} = 1000\mu$m, $W_{in} = 3000\mu$m, $W_{out} = 49\mu$m, $L_{\mathrm{WG}} = 25.4$ mm and conductivity of the metal $\sigma = 3.56 \cdot 10^7$ S/m.

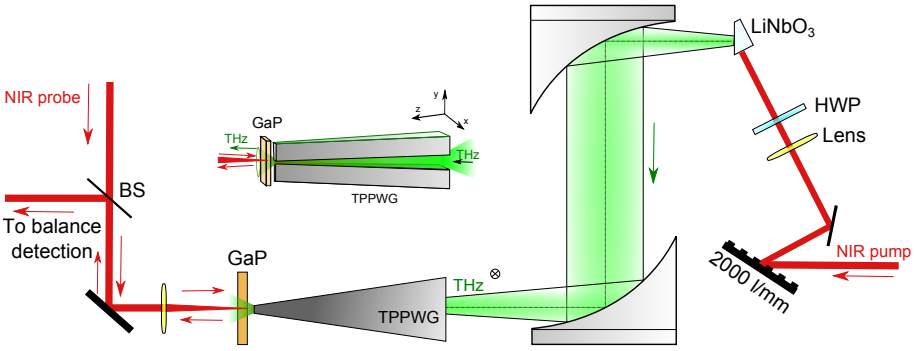

FIGURE 4.14: Schematic of the electro-optic detection of output from the tapered parallel plate waveguide. THz radiation is generated using the tilted wavefront method in $LiNbO_3$, coupled into the TPPWG, propagates along it, couples out and is detected in 300 μm-thick [110] GaP crystal in reflection configuration. Distance between output of TPPWG and the GaP crystal is $\sim 360\mu$m.

The beam waist at the focus point has been estimated to be approximately 20 μm. The lens is mounted on a micrometric xyz-translation stage for an accurate alignment on the crystal. Due to unfortunate geometrical restrictions the distance between GaP crystal and waveguide output can not be shorter than 300 μm. The THz electric field induces a phase retardation between polarization components of the NIR probe. The phase retardation is measured by the balanced detection. The same setup was used to detect THz field at the input to the waveguide.

The second method of calibrating the electric field of the THz wave at the output of the TPPWG is based on measuring the THz induced SH intensity. According to Eq. 4.9 the total second harmonic generated as a result of interaction between the THz transient, the fundamental pulse and the DC bias electric field is expressed by

$$I_{2\omega} \propto \left(\chi^{(3)} I_{\omega}\right)^2 \left[E_{THz}^2 + 2E_{bias}E_{THz} + E_{bias}^2\right]. \tag{4.22}$$

Now, instead of modulating E_{bias} as it is done in the ABCD method, we will modulate the THz beam by inserting an optical chopper in its path. A lock-in amplifier is locked to chopper frequency and detects following SH intensity

$$I_{2\omega} \propto [E_{THz}^2 + 2E_{bias}E_{THz}]. \tag{4.23}$$

Performing two measurements of SH intensity: $I_{2\omega}^0$ without and $I_{2\omega}^{bias}$ with known external DC bias, the absolute amplitude and sign of the THz electric field can be determined:

$$x = \frac{I_{2\omega}^{bias} - I_{2\omega}^0}{I_{2\omega}^0} = \frac{2E_{bias}E_{THz}}{E_{THz}^2}, \tag{4.24}$$

$$E_{THz} = \frac{2E_{bias}}{x}, \tag{4.25}$$

where x is the modulation depth of the generated second harmonic. Figure 4.15 shows measurements of intensity of the THz induced SH without and with external 10 kV/cm bias at the output of TPPWG with an output gap of 100 μm. Measurements are performed in the setup

presented in Fig. 4.4. Because of the bipolar nature of the THz transient one peak of the induced SH decreases in the presence of external field while the other one increases. Using the method outlined above the peak of the THz electric field has been calculated to be 295 kV/cm. To check if the THz induced second harmonic has a nature described by Eq. 4.23, a pair of polarizers has been inserted in the path of THz beam. By rotating the first polarizer, the THz field strength can be varied. Figure 4.16(a) shows the intensity of the generated SH as a function of E^2_{THz}. A linear dependence is clear for over two orders of magnitude of the THz intensity. Figure 4.16(b) shows the difference of the generated SH in the presence of external bias DC field, which is well described by a linear function of E_{THz}.

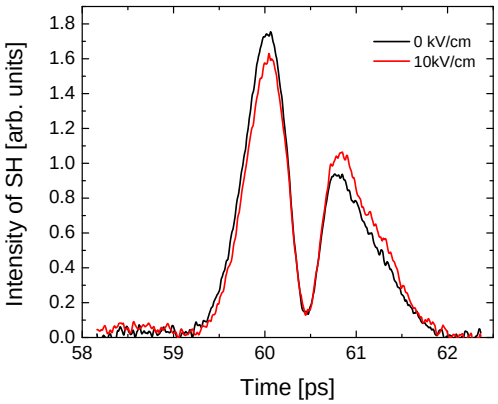

FIGURE 4.15: Intensity of THz induced second harmonic (SH) for output gap of 100 μm with and without DC bias.

Figure 4.17 presents the collection of results of the peak THz field at the output of the TPPWG for different output gaps B_{out} in the range 20 - 200 μm. Black squares are results of direct measurement using THz-induced second harmonic generation. Unfortunately due to high intensity of the probe beam (though still lower than plasma ionization threshold) measurements of the THz field in this way for B_{out} smaller

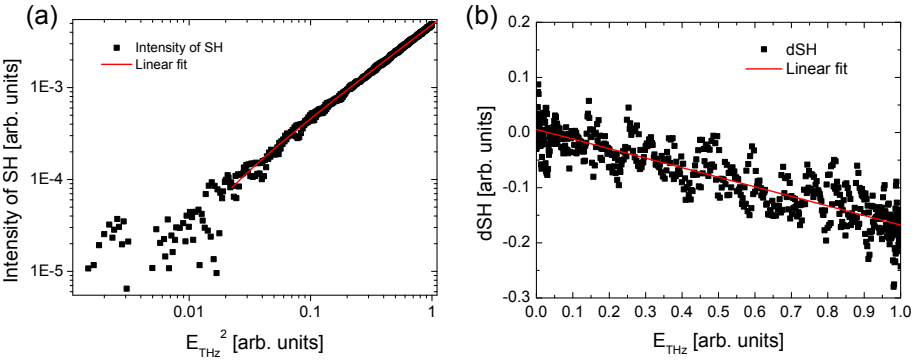

FIGURE 4.16: (a) Intensity of generated SH as a function of E_{THz}^2. Red line shows best linear fit. (b) Difference of intensity of generated SH (with and without external DC bias) as a function of E_{THz}. Red line shows best linear fit. Bias field 8.5 kV/cm, output gap of the TPPWG 140 μm. The peak THz field is 293 kV/cm.

than 60 μm resulted in a high chance of damaging the waveguide, so values are presented only for $B_{out} \geq 60\mu$m. Red circles in Fig. 4.17 represent values of peak THz electric field measured using electro-optic detection in GaP crystal corrected by outcoupling coefficients. Previously described numerical CST Microwave Studio simulations were used to obtain values of the outcoupling coefficients, which are calculated by considering average THz electric field at the location of the GaP crystal divided by peak value of the field at the tip of the waveguide. The blue dashed line shows values of the THz field from CST Microwave Studio simulation, using the previously described elliptical beam with peak THz field of 68 kV/cm as input. All the three values of the peak electric field at the tip of the TPPWG agree well with each other over a wide range of B_{out}. The small differences can have different nature of origins. For the THz field obtained by air-photonic method they can be caused by non-uniform distribution of the bias field within the THz beam. Deviations can also come from the fact that local field enhancement at the edges of the waveguide were probed. The uncertainty of the electro-optic values are increasing with decreasing the output gap size, since the outcoupling coefficients are smaller. Error bars in the Fig. 4.17

has been calculated on the basis of uncertainty of the distance between the waveguide tip and GaP crystal. In any case the good agreement between different measurements indicate that very high values of the THz field at the tip of the waveguide were achieved. For the output gap of 20 μm we estimated a value of over 1.4 MV/cm. Even higher values are expected for smaller output gaps.

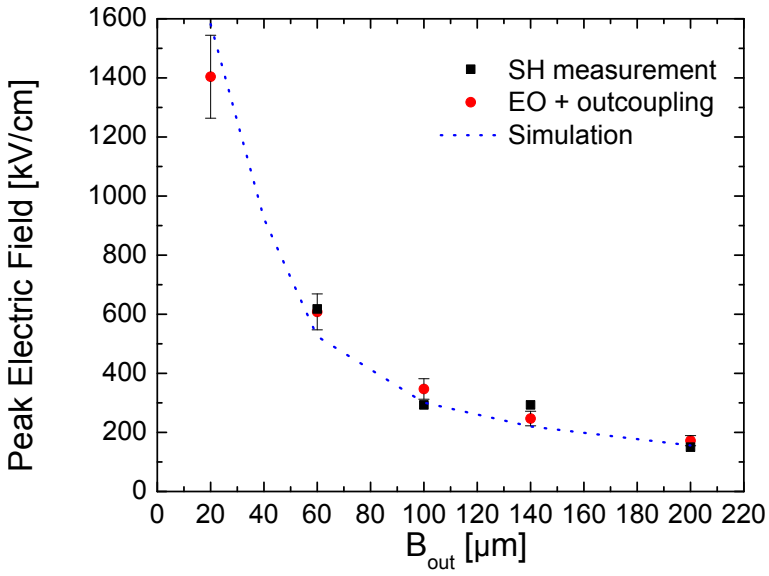

FIGURE 4.17: Peak electric field at the output of the TPPWG for different output gaps B_{out}.

In Fig. 4.18(a) the waveforms of THz radiation transmitted through the TPPWG for different output gaps B_{out} are shown. THz radiation is detected in a 300 μm-thick [110] GaP crystal positioned 358 ± 30 μm away from the waveguide output. No signs of group velocity dispersion is visible. Small part of radiation that leaked around the tip is visible for the closed waveguide output. Figure 4.18(b) shows output spectra of THz radiation transmitted through the TPPWG for different output gaps B_{out}, normalized to the input spectrum incident on the whole waveguide. The spectra are presented on a logarithmic plot. The dashed line shows the best fit to the spectrum according to Eq. 4.18, where THz

Ohmic losses are proportional to the square root of frequency. The dip at $\sim$ 1.7 THz comes from incomplete cancellation of water vapor absorption lines in the reference and sample spectra, due to 25.4 mm of extra propagation in the humid air.

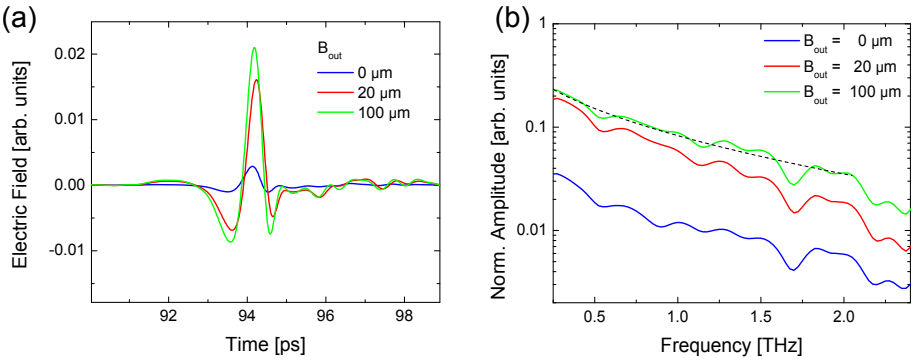

FIGURE 4.18: (a) Measured waveforms and (b) spectra of THz radiation transmitted through the TPPWG normalized to the input spectrum. THz radiation is detected in 300 μm-thick [110] GaP crystal positioned $\sim$ 360 μm away from the waveguide output. Dashed line shows the best fit to the spectrum according to the Eq. 4.18.

4.6 Conclusions

In conclusion we have presented a novel non-invasive broadband method of imaging the THz field inside PPWGs. The method does not disturb the propagating THz field as exemplified by the measurement of the THz reflection coefficient from the tip of the waveguide. The resolution of the method is restricted by the geometrical dimensions of the NIR probe focus spot only, while the frequency response depends on the interaction length between THz and the NIR probe. We investigated field enhancement properties of the TPPWG and we showed that a field enhancement of over 20 is possible, resulting in THz peak electric field exceeding 1.4 MV/cm for the output gaps of 20 μm. Field values were measured using two methods: free-space electro-optic sampling and THz

enhanced second harmonic generation. Obtained values agree with each other and also with predictions from numerical simulations. Even higher values of peak THz field are expected for smaller output gaps. Such high values of electric field open exciting possibilities of investing THz nonlinear processes.

Chapter 5

Terahertz radar cross sections

Scattering of terahertz waves by conducting and dielectric objects is an area of intensive investigation both from theoretical and experimental side [191–195]. Time-domain based THz systems can provide a convenient, fast and precise method of visualization of scattering centers. At the same time, the measurement of the radar cross section (RCS) is a standard technique, particularly important for military and defense-related purposes, including detection and identification of aircrafts, ships and other targets as well as for countermeasures such as RCS reduction and stealth. The necessity for operating on massive objects, such as full-size airplanes or ships, can make those measurements complicated, time consuming, and expensive. Also the size of the platforms makes it impractical to iterate the design and testing phases allowing only for software calculations of RCS values with limited possibility of experimental testing.

Submillimeter continuous wave systems based on molecular lasers with bolometric detectors for characterization of RCS on scale targets have

been previously investigated [196]. Poor signal to noise ratio, single frequency operation and no possibility of depth resolution were important factors limiting the application of those systems. In this chapter we combine a time-domain based THz system and the RCS technique to obtain RCS values at broadband THz frequencies with high signal to noise ratio and depth resolution of 200μm. By employing scaling laws we are able to scale values measured in the low THz range (0.1-2 THz) into values that would be measured at radar frequencies. Typical radar systems operate at a frequency range from hundreds of MHz up to a few tens of GHz. This defines the scaling factor between THz waves and radar waves from tens to a few hundreds, forcing scale objects to be in the size range of a few centimeters and larger. Objects of such dimensions are easy to handle and manipulate and allow for iterative design and testing procedure, where the test object is manufactured by a rapid prototyping system such as a computer numerically controlled 3D milling machine or a 3D printer.

Radar technology also opens the door for imaging objects using synthetic aperture radars (SAR) and inverse synthetic aperture radars (ISAR), which will be explained in chapter 5.1.1. The first works on this ground using THz frequencies also have been performed [197–200]. Most of this work is in its proof-of-concept phase and significant progress still has to be achieved before THz SAR and ISAR imaging systems can be used outside laboratories.

In this work we measure the THz RCS of scale models and present polar and azimuthal time- and frequency resolved RCS plots of F-16 and F-35 fighter aircraft models rotated on a pedestal. The time domain sub-ps resolution allows for sub-mm range resolution and also allows for identification of scattering points. The obtained sub-mm range resolution for THz frequencies after upscaling to radar frequencies is comparable with the resolution of modern radars. The shape of the model and positions of scattering parts are retrieved by the filtered back projection algorithm.

5.1 Radar Cross Sections (RCS)

The term radar comes from the phrase "radio detection and ranging". Radar plays an important role in both military and civilian applications. In the civilian systems, radar is used for navigation, air traffic control, weather monitoring and altimetry. On the military side, radars perform reconnaissance, surveillance and attack tasks. Military missions have higher chances of success when detection by the enemy is avoided. For this reason reduction of radar cross section has received high priority in the design of new platforms such as airplanes, ships, missiles and satellites. Those invisible to radar platforms have been described as "stealth". To be undetectable, it is necessary that the radar echo returning to the receiver is below detection threshold. Stealth technology has evolved as a countermeasure against radars and in a consequence more sensitive radars have evolved to detect lower RCS platforms.

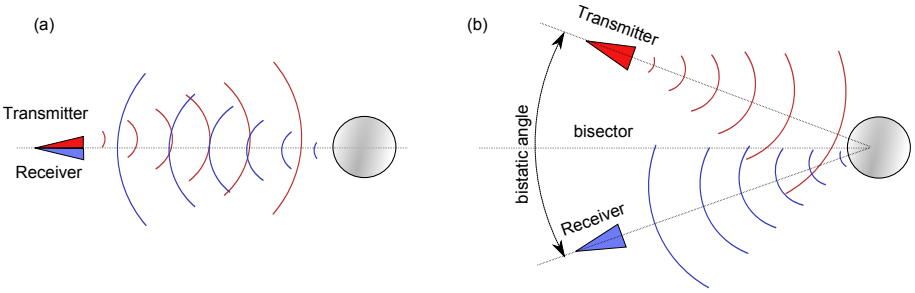

FIGURE 5.1: (a) Monostatic and (b) bistatic radar configuration.

In the most general case, the radar transmitter and receiver can be at different locations, as shown in Fig. 5.1(b). This is referred to as bistatic radar. However, the transmitter and receiver are usually located on the same platform and share antenna, which is called monostatic configuration and has been depicted in Fig. 5.1(a). When a radar uses two slightly separated antennas, it is called quasi monostatic. For the purpose of this study, the quasi monostatic can be considered equal to

monostatic, since the distance between antennas is much smaller than the distance to the target.

Most radars operate in the frequency range of 10 MHz - 100 GHz, where low frequencies are used for long range high power search radars and higher frequencies for airborne compact short range radars. Typical bandwidths are up to few percent of the central frequency. A modern radar can provide a large amount of information about a target and the environment, such as: 1) range, measured as the propagation time of a radar pulse to the target and back, 2) velocity, by measuring the Doppler frequency shift 3) size of the target, based on the scattered signal intensity 4) target shape, determined by the magnitude as a function of the viewing angle.

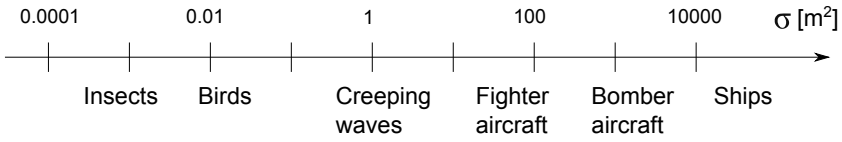

FIGURE 5.2: Typical values of RCS for some natural and man-made objects.

The RCS of a scattering target illuminated with radar radiation is a parameter expressed in units of area which describes the intensity of the wave reflected back to the radar. The most general definition of RCS can be written as [201, 202],

$$RCS = \lim_{R\to\infty} 4\pi R^2 \frac{|E_s|^2}{|E_i|^2} \tag{5.1}$$

where E_i and E_s are the incident and scattered electric fields, and R is the distance between radar and target. In this definition the limiting process is primarily introduced to ensure that the incident wave is a plane wave which, in the optical design of our setup presented in Chap. 5.3, is fulfilled. As indicated in Fig. 5.2, typical values of RCS range from $\sim$0.001 m^2 for insects, $\sim$ 0.01 - 0.1 m^2 for birds, $\sim$ 100 m^2 for fighter airplanes to over 10000 m^2 for large ships. The RCS depends on

many factors. Those include the size and shape of the target, incident and reflected angle, ratio between the size of target and the wavelength, polarization of the emitted and detected radiation and finally on the properties of the material that the target is made of.

Below we will derive the radar range equation. Let us consider a monostatic radar located a distance R from a target. The radar transmitter power is P_t and the antenna gain is G_t. The incident power density at the target W_i is given by

$$W_i = \frac{P_t G_t}{4\pi R^2}. \tag{5.2}$$

The RCS relates the incident power density W_i at the target to the power scattered back in the direction of the observer W_s.

$$W_s = \frac{P_t G_t}{4\pi R^2} \cdot RCS \cdot \frac{1}{4\pi R^2} \tag{5.3}$$

Power received by the detector P_r is the product of the scattered power density W_s and effective receiving antenna area A_{eff} :

$$P_r = \frac{P_t G_t}{4^2\pi^2 R^4} \cdot RCS \cdot A_{eff} = \frac{P_t G_t}{4^2\pi^2 R^4} RCS \frac{G_r \lambda^2}{2\pi}, \tag{5.4}$$

where $G_r = \frac{2\pi A_{eff}}{\lambda^2}$ is the receiving antenna gain. Since $P_r \sim RCS/R^4$ that implies that if an airplane wants to be twice as close to the radar and stay undetected it has to reduce RCS by factor of $2^4 = 16$. This strong dependance of maximum stealth RCS on the minimal radar-target range underlines the importance of proper design of the aircraft and its RCS characterization.

The wave scattering of a target is strongly dependent on the incident wave frequency. There are three frequency regions in which the scattering characteristics are different. Those regions are distinguished by the product of the incident wavevector k and the characteristic size of the target L.

- Low-frequency region, also called Rayleigh range, where $k \cdot L \ll 1$. At those frequencies the phase variations of the incoming plane wave across the target are small. The shape of the target's body is not important (e.g., a small metal sphere and a small metal cube will have similar scattering pattern). Wave scattering is essentially isotropic (direction independent). In general, RCS vs. $k \cdot L$ is smooth and varies as $1/\lambda^4$ (as presented on the Fig. 5.3). Rayleigh scattering of the sun light on microscopic air density fluctuations is the phenomena that makes the sky blue.

- Resonance region, also called Mie range, where $k \cdot L \approx 1$. The phase variations of the incoming plane wave across the target are significant. All parts of the object contribute to the scattering pattern. RCS vs. $k \cdot L$ will oscillate.

- High-frequency region, also called optical range. $k \cdot L \gg 1$. Multiple 2π phase variations of the incoming plane wave across the target. The scattered field is strongly angle dependent. Strong narrow scattering peaks are possible due to the specular scattering (mirror-like reflection) by big flat surfaces. In general, in this region RCS vs. $k \cdot L$ may be smooth and independent of λ.

A perfect illustration to those three frequency regions is the scattering of electromagnetic waves on the most simple scatterer, which is a metal sphere. The RCS of a perfectly conducting sphere with radius r as a function of $k \cdot r$ is depicted in the Fig. 5.3. The presented RCS is calculated on the base of the Mie theory [203, 204]. For $k \cdot r \ll 1$ the RCS varies as $1/\lambda^4$, for $k \cdot r \approx 1$ the RCS oscillates around πr^2 and for $k \cdot r > 1$ a metal sphere has a frequency independent RCS equal to its physical cross section area $RCS = \pi r^2$.

For a conducting cylinder the largest $RCS = 2\pi r h^2/\lambda$ is achieved at the specular angle, where h is the height of the cylinder. The RCS of a flat conducting plate with sides a and b decreases rapidly with angle from

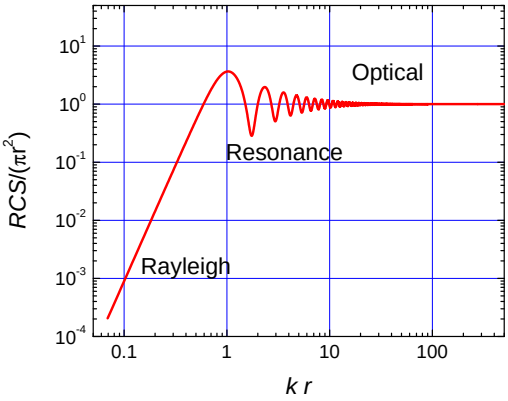

FIGURE 5.3: RCS of a perfectly conducting sphere of radius r as a function of $k \cdot r$ product.

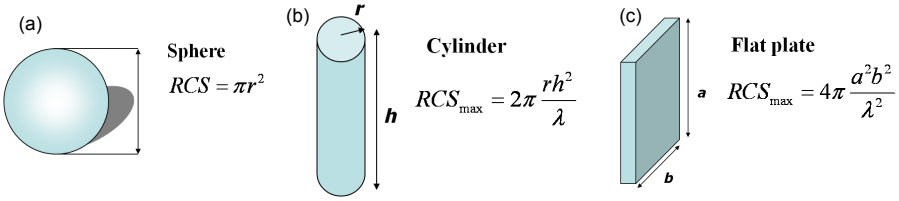

FIGURE 5.4: Maximum RCS of (a) sphere (b) cylinder (c) flat plate.

the maximum value $RCS = 4\pi a^2 b^2/\lambda^2$ at the specular reflection angle, which has been depicted in the Fig. 5.5.

The RCS should ideally be a parameter describing the target and should not depend on the target-detector distance. This statement is valid only for sufficiently large distances. Let us consider a flat conducting disc with radius r_0, which can be treated as a perfect reflector. Figure 5.6 shows the RCS at the specular reflection angle as a function of the disc-radar distance R, calculated using $RCS\,(R) = 4\pi R^2 \frac{|E_s(R)|^2}{|E_i|^2}$. The scattered field $E_s\,(R)$ has been found using Fresnel diffraction integral. For short distances $|E_s|^2 = |E_i|^2$ and the RCS increases as R^2 with

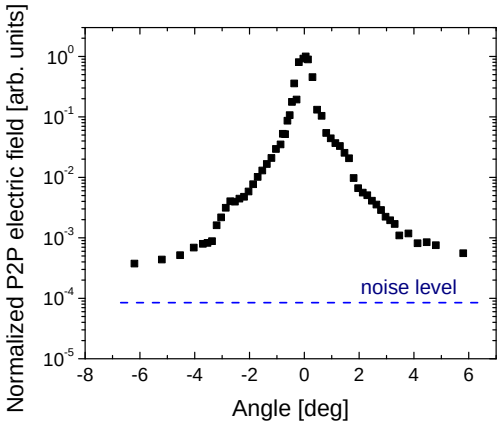

FIGURE 5.5: Normalized peak-to-peak electric field scattered by a 15 cm in diameter flat plate measured as a function of azimuthal plate orientation. Blue line represents noise level without the plate in the THz path.

modulation which originates in interferences. For longer distances wave diffraction becomes dominant and $|E_s|^2 \propto 1/R^2$ implying that the RCS saturates. It can be shown that the RCS of a circular flat disc reaches 91% of its long-distance value at a distance $R = 3r_0^2/\lambda$. The distance where the RCS reaches its far-distance value is shorter for objects with smaller radius of curvature. Also, the angular distribution of scattered electric field depends on the distance from the target. It may seem counterintuitive that RCS increases with the distance to the radar. It can be explained a bit more on the example of a radar operator. If radar detects an unknown object, the distance to the object R can be computed using time of flight of the scattered signal. The radar operator, knowing the power of his radar, may calculate value of the electric field at the position of scatterer. Hence one measures scattered field, one can calculate RCS using equation $4\pi R^2 \frac{|E_s|^2}{|E_i|^2}$. Now if the object is closer to the radar, the computed values of R, E_s and E_i will be different, so RCS can also change. Even though the calculated value of RCS can decrease, it does not mean that the object will be less visible to the radar, simply

because according to Eq. 5.4 power received by radar increases with decreasing distance faster ($P_r \sim RCS/R^4$).

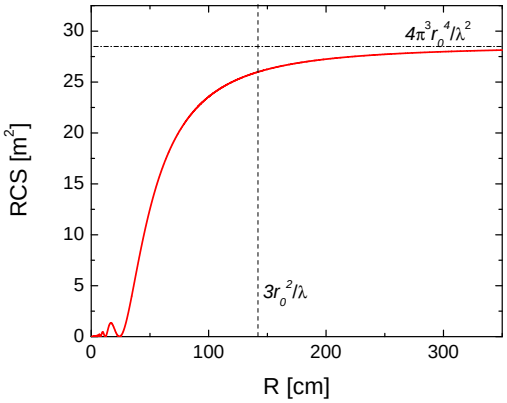

FIGURE 5.6: RCS of a flat conducting disc of a radius $r_0 = 12$ mm as a function of disc-radar distance R. THz radiation at frequency of 1 THz is incident and scattered at normal angle. RCS reaches 91% of its long-distance value $RCS_\infty = 4\pi^3 r_0^4/\lambda^2 = 28.6$ m^2 at a distance $R = 3r_0^2/\lambda = 143$ cm. The RCS is over 63000 times larger than the geometrical cross section.

The RCS of objects typically encountered by radars are more complicated than simple spheres, cylinders or plates. But the scattering pattern of any complex targets can be decomposed into primitives (basic geometrical shapes). It is possible to express the total scattered electric field as a superposition of fields scattered by the individual source on the target:

$$|E_s| = \left| \sum_{n=1}^{N_s} E_{s_n} \right|, \tag{5.5}$$

where N_s is the number of primitive scattering objects. Each of the basic objects may be characterized by different frequency and angle dependent scattering mechanism. For RCS measurements the three most important scattering mechanisms are:

- Reflections. This mechanism gives the highest RCS peaks, but peaks are limited to the number or reflecting surfaces. Multiple surfaces can produce multiple reflection (e.g. corner reflector).

- Diffraction. Diffracted waves originate at discontinuities on the target, such as edges and tips. Scattered fields are less intense but appear in a wide angular range.

- Surface waves. Electromagnetic waves that propagate along the target and then are reemitted in the direction of the receiver. One example are creeping waves, which travel around a curved object.

5.1.1 Synthetic aperture and inverse synthetic aperture radar imaging

A Synthetic Aperture Radar (SAR), is a coherent radar system which utilizes the movement of the radar platform to electronically simulate an extremely large antenna or an aperture. This procedure generates high-resolution remote sensing images. The synthetic aperture radars are mostly airborne or spaceborne sidelooking systems. The SAR works similar to a phased array, but in contrast to a large number of the parallel antenna elements of a phased array, SAR uses one antenna in different locations. The different geometric positions of the antenna elements are a result of the moving platform.

Complimentary to SAR is the inverse synthetic aperture radar (ISAR) systems. The ISAR technology uses movement of the target rather than emitter to create the synthetic aperture. High resolution ISAR images allow for discrimination between various missiles, military and civilian aircrafts. If the investigated target is rotated by an angle $\Delta\theta$, the phase ϕ of the object will change proportionally to the cross-range (direction perpendicular to the radar wave propagation) distance X from the center of rotation to the target as it undergoes a change in range according to the formula: $\phi \approx 2\pi\Delta\theta X/\lambda$. Therefore, if the change of the phase ϕ

of the target is measured over a finite angular extent, the cross-range coordinate X of the scatterer can be calculated by performing a simple Fourier transform. In a similar way, the downrange distance (along the radar wave propagation) to the target can be calculated by varying the frequency of the radar and carefully measuring the change in the phase of the scatterers. For accurate ISAR imaging, high resolution frequency determination of the phase of scattered field is needed. Also very high phase stability is required. To obtain a 2D image, the investigated object has to be rotated independently along two perpendicular axes, which are perpendicularly oriented to the radar wave propagation. The acquired 2D matrix of phase values of the scattered field is Fourier transformed to obtain 2D image of the scattering centers.

5.2 Terahertz Computed Tomography

Tomography is a cross-sectional imaging of objects, obtained by measuring the transmitted or reflected radiation. The most common type of tomography is computed tomography (CT), in which digital geometry processing is used to generate a three-dimensional image of the inside of an object from a large series of images taken around a single axis of rotation. Particularly popular version of CT is a X-ray CT, which through out years has become a standard medical imaging techniques (Nobel prize in 1979). Although primarily used in medicine, CT is also used in other fields, such as nondestructive materials testing, archaeology, paleontology and biological studies.

In computed tomography investigated object is rotated by 360° along single rotation axis. Next the object is divided into set of slices along this rotation axis. For each slice a set of line scans indexed by the slice orientation round the rotation axis is measured. Those line scans are also called as shadow images and are connected to the optical properties

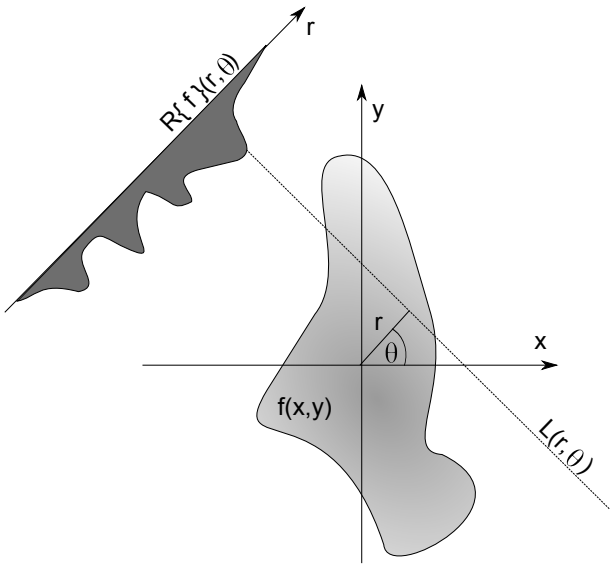

FIGURE 5.7: Schematic of the Radon transform. The Radon transform $R\{f\}(r,\theta)$ of the function $f(x,y)$ represents a total object optical density integrated along the $L(r,\theta)$ line. Line $L(r,\theta)$ is defined by the distance to the rotation axis r and the angle θ.

of the investigated slice by a Radon transform [205]:

$$R\{f\}(r,\theta) = \int_{L(r,\theta)} f(x,y)\, ds, \tag{5.6}$$

where $f(x,y)$ is a function describing the properties of the scanned object. In case of X-ray CT, $f(x,y)\,ds$ represents the probability that the radiation is absorbed or scattered in the section ds along a straight line $L(r,\theta)$. For each shadow image filtered backprojection algorithm [206] can be used to invert Eq. 5.6 and obtain 2D tomography slice. The basic idea behind back projection method is to populate pixels of the reconstructed image with the shadow projections back along the directions they were measured (hence the name "back projection") to obtain a rough approximation to the original. The back projections from different angles will add constructively in regions they originate from.

Unfortunately this solution gives blurring of the image and high-pass spatial filtering is needed to make the back projected image sharp. A set of 2D tomography slices stacked together give a full 3D image.

Terahertz computed tomography, demonstrated first by Ferguson and co-workers [207], is a growing imaging technique [208–210]. There are several differences between THz and X-ray CT, which come from the different nature of wave interaction with matter. In the X-ray range choosing the absorption as the $f(x, y)$ function is straightforward and it is a good representation of the density of the object. In the THz range different quantities have been used: total transmitted power, time of flight of the THz pulse or the phase of transmitted radiation. The next difference arises from the fact that the THz beam propagation can not be accurately described as a straight ray-line, which is valid for X-ray. The wavelength of THz radiation is seven order of magnitude longer than X-ray, so the diffraction and scattering can blur and deform reconstruction image. Also choice of the reconstruction algorithm is an important factor and can improve the quality of the reconstructed image [211]. In most cases THz CT is performed in the transmission configuration, but the reflection configuration has also been investigated [212].

5.3 Experimental Setup

A schematic diagram of our THz RCS setup is shown in Fig. 5.8. A regenerative Ti:sapphire femtosecond laser amplifier delivers 35 fs, 2.9 mJ pulses with center wavelength of 800 nm at a 1 kHz repetition rate. The laser output is split into a source beam for THz pulse generation and a gating beam for THz detection by free-space electro-optic sampling. THz waves are generated by optical rectification in lithium niobate $LiNbO_3$ crystal applying the tilted pulse front method, described in chapter 2.2.2. The intensity front of fs pulses is tilted by a 1714 line/mm grating and imaged by a 75 mm lens with demagnification factor of 2 onto the front surface of a stoichiometric $LiNbO_3$ crystal at room temperature. The

$LiNbO_3$ crystal was doped with 2% of MgO to prevent photorefractive damage [213]. The highest THz peak electric field in the focused THz beam achieved in our setup is at least 40 kV/cm, limited predominantly by the high angular and material dispersion inside the $LiNbO_3$ crystal of the 60 nm-FWHM pump pulses. The high efficiency of THz generation allows us to obtain high dynamic range of the setup up to 43 dB, defined as ratio between the peak electric field to the noise floor for the THz beam reflected in a specular angle off a metal mirror bigger than the THz beam - (blue line in the Fig. 5.5). The near-infrared light transmitted through the $LiNbO_3$ crystal is blocked by a black polyethylene sheet, which is highly transmissive for the THz pulse.

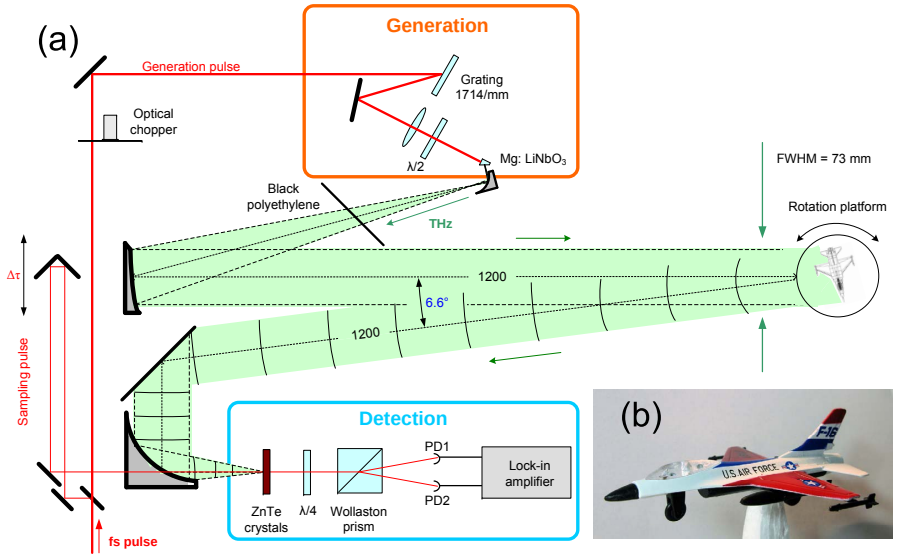

FIGURE 5.8: (a) Schematic diagram of the THz RCS setup. (b) 10 cm-long 1:150-scale metal model of aircraft fighter F-16.

A pair of off-axis parabolic mirrors with focal lengths of 25.4 mm and 516.8 mm and diameters of 25.4 mm and 101.6 mm respectively is used to expand the THz beam and subsequently to collimate it. The wide,

collimated THz beam propagates 1200 mm towards the target which is placed on a computer-controlled rotation platform. The expansion optics increases the THz beam size by a factor of 20, which leads to a spatial FWHM of 73 mm of the THz electric field at the object distance. The electric field of the THz transient is polarized in the vertical plane. The scattered THz radiation is collected by a 170 mm−diameter flat metal mirror at a distance of 1200 mm from the target, and focused using a 101.6 mm-diameter, 152.4 mm-focal length off-axis paraboloidal mirror onto a detection crystal. The scattered THz radiation thus travels 1430 mm before it reaches the detector. The angle between the incident and scattered radiation is 6.6° and therefore our RCS measurements are in principle bistatic, but in practice reasonably close to a monostatic radar configuration. A truly monostatic configuration can be achieved by using a thick wedge silicon beam splitter and a normal incidence. Such a configuration will inevitably reduce the dynamic range due to reflection losses on the beam splitter. All THz and infrared beams propagate at a height of 160 mm above optical table which is sufficient to avoid reflections from the table surface. The setup is aligned using a big 170 mm-diameter metal mirror in a place of the scattering object. This mirror reflects all THz radiation in the direction of the receiver. The complete THz beam path is purged by dry nitrogen to avoid absorption by water vapor in the atmosphere.

The 800 nm probe beam is directed through a small hole in the center of off-axis parabolic mirror for collinear detection. A computer-controlled delay stage is used to map the temporal THz pulse shape. The electric field of the THz transients is detected by free-space electrooptic sampling in a [110] zinc telluride (ZnTe) crystal (2 mm-thick). A second passive [100] 2mm-thick ZnTe crystal with anti-reflective coating for 800 nm light on one facet is stacked together with the active crystal to increase temporal separation between the directly transmitted THz pulse (transient A in Fig. 5.9(a)) and the pulse that experience two reflections in the detection crystals (transient B in Fig. 5.9(a)) [214]. The time delay between these two pulses is 89 ps. The temporal order of incoming pulses

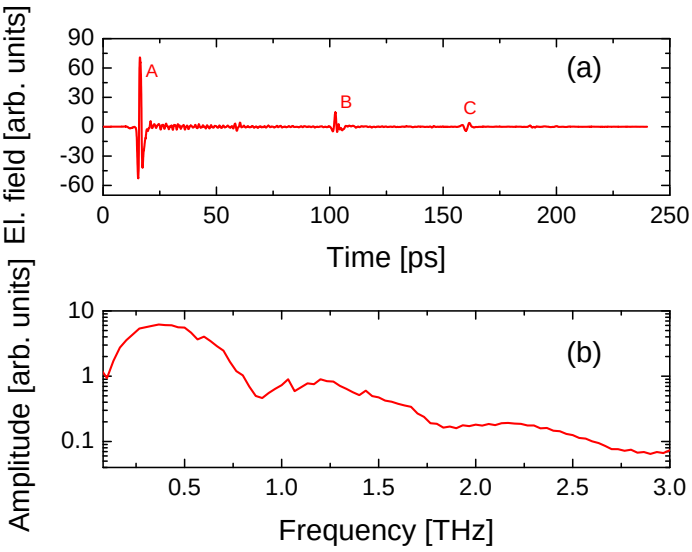

FIGURE 5.9: (a) THz waveform reflected from a 170 mm-diameter metal flat disk. The transient include the main THz pulse (labeled A), a partial reflection of the main pulse inside the detection crystals (labeled B), and a part of the main pulse undergoing multiple reflections in the $LiNbO_3$ crystal (labeled C). (b) The amplitude spectrum of the generated THz radiation obtained as a Fourier transform of a 50 ps-wide time window around transient A.

is further complicated by an additional THz pulse (transient C in Fig. 5.9(a)) which experiences multiple reflections inside $LiNbO_3$ crystal and arrives at detector 160ps after the main pulse. Between transient A and pulse B (at 60 ps) there is also a small pulse visible, which has its origins in imperfections of the boundary between the [110] detection crystal and the [100] inactive spacer crystal. The FWHM of the main THz transient of 0.96 ps allows for distinction of two different point scatterers separated by 144 μm along the THz propagation direction. Figure 5.9(b) shows the amplitude spectrum of the detected THz radiation obtained from a Fourier transform of a 50 ps time window around transient A. The amplitude spectrum extends from 0.02 THz up to 3 THz, but 95% of the generated THz energy lies within 0.1 THz - 1.0 THz range. The

longest THz waves that are generated in our setup have a wave vector of $k = 2\pi/\lambda =\sim 2$ mm^{-1} (at ~ 0.1 THz), so for all the investigated objects ($L > 1$ mm) we are in the optical regime ($kL \gg 1$).

The target objects are placed on a support column of polystyrene foam, which consists of 97% air or other gases and only 3% polymer, and thus has low refractive index of 1.02 in the THz range [215]. Furthermore, the polystyrene foam is cut in a shape which resembles a tapered diamond column, which reflects all the THz radiation away from the detector. No signs of volume reflections from the thousands of internal cells in the foam structure have been observed. No THz signal has been measured without samples positioned on the polystyrene support column above the background noise level. The investigated target was a 1:150-scale model of aircraft fighter F-16. The model was 10 cm long with a wingspan of 6.7 cm. The object was made of painted metal with elements such as missiles, nose and undercarriage made of plastic.

5.4 Terahertz radar cross section on scale models of aircrafts

Before the RCS measurements are performed in the previously described setup, the linearity check and calibration of the setup has to be executed. We have decided to do it using the most standard technique, based on the field scattering from conducting spheres. Figure 5.10 shows the peak scattered electric field as a function of metal sphere diameter between 2 and 45 mm. The steel spheres are placed on the polystyrene column and centered in the THz beam. The data are results of averaging up to 25 single THz waveforms. Since all the frequency components arrive in phase at the peak of the THz transient, the squared value of the peak electric field E_p accurately represents the energy carried by the pulse. Since $RCS_{\text{sphere}} = \pi r^2$ and $RCS_{\text{sphere}} \sim E_p^2$, we find that $E_p \sim r$. This linear relationship is shown in Fig. 5.10 from which the coefficient of proportionality is obtained by linear regression (red line). For metal

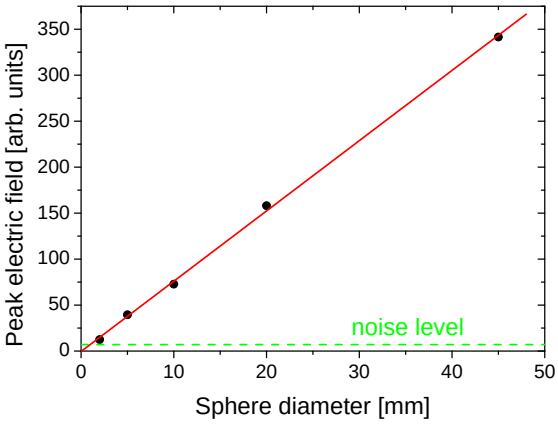

FIGURE 5.10: The peak electric field of THz radiation scattered from a conducting sphere as a function of sphere diameter. The red line shows the best linear fit to the experimental data. The horizontal green line represents the average noise level in single scan measurement. The red and green curves intercept at the point corresponding to a sphere of 0.98 mm diameter.

spheres with diameter larger than the THz beam waist dependence of E_p of sphere radius will become sublinear, and will saturate at a constant value at the limit of $r \to \infty$, when all the THz radiation is reflected to the detector. The horizontal green line in Fig. 5.10 represents the noise level of a single scan. The smallest detectable sphere in a single scan has a diameter of 0.98 mm (crossing of the red and green line).

For complicated structures, which we will be dealing with below, the electric field from multiple point scatterers overlap and another method is required for calculating the RCS. For the purposes of this article we introduce a frequency-averaged RCS, which can be defined by:

$$RCS = \pi r_0^2 \frac{\int_0^T |E_{\text{object}}(t)|^2}{\int_0^T |E_{\text{cal}}(t)|^2 - \int_0^T |E_{\text{bg}}(t)|^2}, \tag{5.7}$$

where $E_{\text{object}}(t)$ is the detected electric field from the scattering object as a function of time t, $E_{\text{cal}}(t)$ the electric field scattered by calibrated metallic spheres of $RCS = \pi r_0^2$, and $E_{\text{bg}}(t)$ represents background noise measured as a signal without the sample on the support column. The standard procedure to calibrate a RCS setup is substitution by a metal sphere of known RCS. Since we measure not only the intensity of electromagnetic radiation but the field itself we can also introduce the frequency resolved RCS defined as follows:

$$RCS = \pi r_0^2 \frac{|E_{\text{object}}(\omega)|^2}{|E_{\text{cal}}(\omega)|^2 - |E_{\text{bg}}(\omega)|^2}, \tag{5.8}$$

where $E_i(\omega)$ is the Fourier transform of $E_i(t)$.

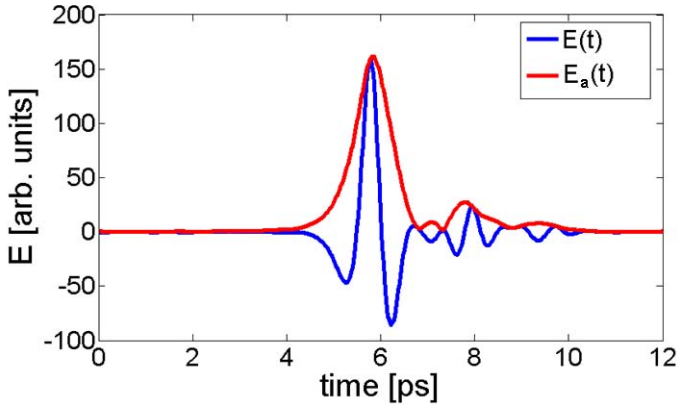

FIGURE 5.11: THz transient $E(t)$ and its instantaneous amplitude $E_a(t) = |E(t) + i \cdot H\{E\}(t)|$

The instantaneous amplitude of the function $u(t)$ is the absolute value of the complex analytic signal $u_a(t) = |u(t) + i \cdot H\{u\}(t)|$, where $H\{u\}(t)$ is the Hilbert transform [216] of a function $u(t)$, and which can be expressed using following formula:

$$H\{u\}(t) = \frac{1}{\pi} \text{p.v.} \int_{-\infty}^{\infty} \frac{u(\tau)}{t - \tau} d\tau, \tag{5.9}$$

where p.v. stands for principal value. For example for a pure sinusoid, the instantaneous amplitude is a constant, while for single-cycle electromagnetic pulses the instantaneous amplitude is a good representation of the envelope function - Fig. 5.11.

Figure 5.12(a) shows the logarithm of the instantaneous amplitude of the THz waveforms vs. polar angle and range (calculated from the time-of-flight of the reflected THz pulse and the speed of light), recorded on the F-16 scale model. In such high range resolution maps the single point scatterers are seen as sine functions (sinograms) of the rotation angle. 0° position on Fig. 5.12(a) corresponds to the position where the nose of the airplane faces the incoming THz radiation, while 180° is tail-on. Clear traces of scattering originating at the airplane nose, wing tips, fuselage, tail and exhaust pipe are visible. Figure 5.12(b) shows the frequency-averaged polar RCS for the investigated scale model. The values of RCS vary from 1.4 cm^2 (seen from the front of the airplane) up to 193 cm^2 (seen from a wing side). The RCS plot is rotated slightly counter-clockwise with respect to the orientation of the symmetry plane because of the 6.6° bistatic design of the setup. The RCS plot is also asymmetric due to a possible minor unintentional azimuthal tilt of the scale model. Figure 5.12(c) presents again the logarithm of the instantaneous amplitude of the THz waveforms, now as function of the azimuthal angle and range. On the azimuthal map, the orientation 0° corresponds to the situation at which the airplane is exposed to THz radiation directly from above. Scattering from wing surfaces and edges, tail, fuselage and even plastic missiles is easily distinguishable. However, due to pulse reflections B and C in Fig. 5.9(a) some of the sinograms are repeated with a delay corresponding to the delay between the reflections, but at significantly lower amplitudes. By inspection of Fig. 5.12(d) we notice that the largest RCS in the azimuthal configuration is when the airplane is seen exactly from below (1208 cm^2) and above (881 cm^2). The smallest RCS is observed just below the wings. The RCS plot is again counter-clockwise rotated with respect to the orientation of the symmetry plane due to the bistatic nature of measurement. Scaling

by a factor of 150^2 can provide the RCS of a full-sized F-16 measured at a distance of $150 \cdot 143$ cm = 214.5 m at frequency $\sim$ 3 GHz. This scaling approach is only valid as far as the model is a true scale copy of the original and under the assumption that the material reflection properties are unchanged as function of frequency. This scaling assumption is true for metals between the GHz and THz frequencies, but may be invalid for the dielectric objects. Both data sets were measured in the configuration where the incoming THz radiation was polarized in the vertical direction. Obtained results would have been different if the THz radiation was polarized in the horizontal direction. We can expect that the biggest differences would come from objects with dimensions in one direction longer than the THz wavelength and in the perpendicular direction comparable or shorter than the THz wavelength, such as thin wires or sharp edges (e.g. wing or tail tips). The FWHM of the instantaneous amplitude of the main THz transient from the Fig. 5.9(a) is 1.8 ps, which gives range resolution of presented sinograms of 270μm.

RCS measurements have also been performed on a 1:150-scale metal model of the aircraft fighter F-35. Fig. 5.13 shows frequency-averaged polar RCS for the investigated scale model. When comparing RCS for F-16 (Fig. 5.12(b)) and for F-35 (Fig. 5.13), few differences are visible. All values of RCS for F-35 fighter are smaller. Secondly, the biggest differences are at angles 90° and 270°. The fighter F-16 has a vertically oriented tail, which gives a strong specular reflections at those angles. Small azimuthal tilt of the model causes the RCS peaks to be asymmetric. At the same time F-35 has two tails, each of them tilted by 20° from the vertical axis so the specular reflections are avoided and measured RCS is $\sim$ 10 time lower.

Figure 5.14 shows values of the frequency-resolved THz RCS of the scale model of the F-16 fighter in the azimuthal configuration for frequencies 0.3, 0.7 and 1.1 THz. We notice that at angles where the THz waves are reflected from large plane surfaces (0° and 180° - from the wing surfaces and at 90° and 270° from the tail surface), the RCS at high frequencies is larger than at low frequencies, in agreement with the

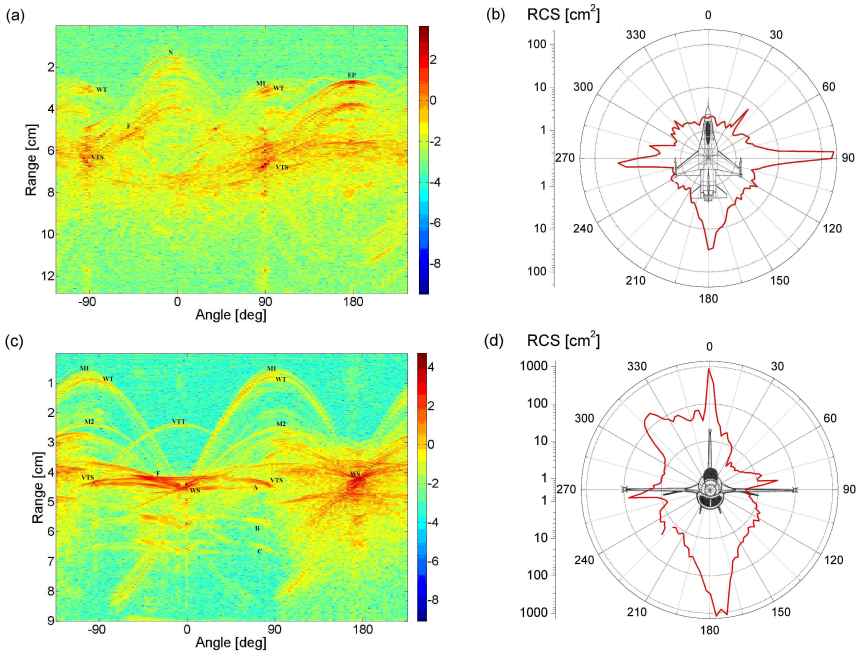

FIGURE 5.12: Logarithm of the instantaneous amplitude of THz waveforms scattered from the F-16 scale model shown in Fig. 5.8(b) for different (a) polar and (c) azimuthal angles and (b), (d) their frequency-averaged *RCS*. Letter marks indicate positions of different scattering parts of the airplane model: nose (N), wing tips (WT), wing surface (WS), vertical tail surface (VTS), vertical tail tip (VTT), fuselage (F), missiles (M1, M2). Additionally letters marks A, B and C show example of the main transient and two echoes (according to Fig. 5.9(a)).

frequency-dependent nature of wave scattering by objects with different curvatures.

Our THz radar system is similar to a reflection tomography setup [212]. Each sinogram contains enough information about the target to transform it into a two-dimensional image of the target. The filtered back projection algorithm (FBP) [206] is one possible method to retrieve the spatial distribution of scatterers. However, the FBP algorithm does not

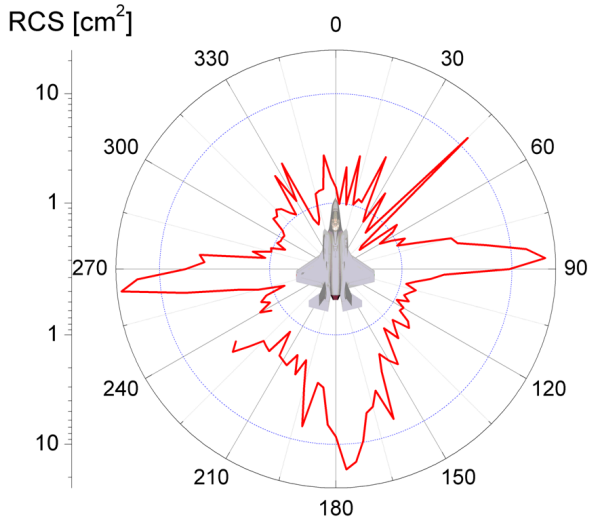

FIGURE 5.13: Frequency-averaged polar *RCS* of a metal model of aircraft fighter F-35

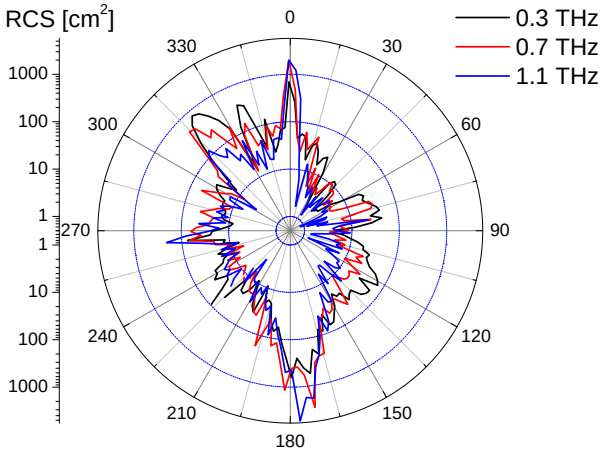

FIGURE 5.14: Frequency-resolved azimuthal RCS of a metal model of the fighter aircraft F-16 at frequencies 0.3, 0.7 and 1.1 THz. The presented data are averaged within a frequency interval of +/− 20GHz.

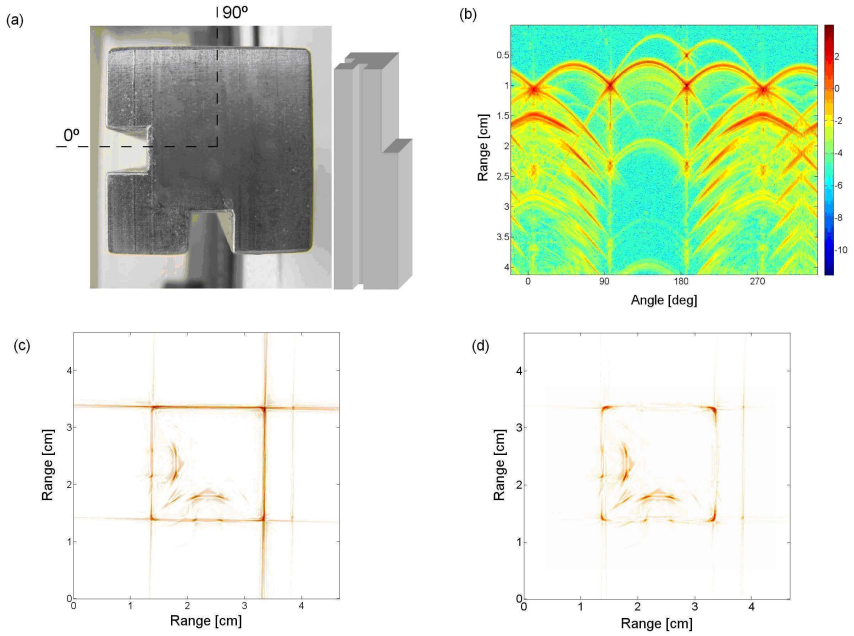

FIGURE 5.15: (a) Metal test target (b) Logarithm of the instantaneous amplitude of THz waveforms scattered from the metal test target. (c) Cross section of the test target reconstructed using filtered back projection algorithm (d) Cross section of the test target reconstructed using filtered back projection algorithm with windowing out flat surface reflections.

include wave diffraction effects which leads to artifacts that we demonstrate by measurements on a metal test target shown in Fig. 5.15(a). The test target is an elongated cuboid (20 x 20 mm in cross section) with two 4 x 4 mm grooves cut in its cross-section profile. Additionally on one of the sides a 4 mm-thick step was introduced to make the structure more asymmetric. Figure 5.15(b) shows sinogram for the test target. Data are taken with 1° angular resolution. Figure 5.15(c) shows the FBP reconstruction using data from Fig. 5.15(b). Because of the small sizes of the test object (for most of the angles echoes B and C do not overlap in time with the real reflected signals) it was possible to apply simple time windowing function that would minimize effects of

echoes B and C. The reconstructed image represents the actual shape of the target well. However, the image is not free from artifacts in the form of lines crossing the whole image, with the tendency for large plane surfaces to be represented by stronger and longer lines. This behavior originates in the fact that the FBP algorithm does not compensate for diffraction of scattered waves. That effect is especially important at intermediate target-detector distances, where the angular distribution of electric field depends strongly on object size and shape. In our case the detector is placed 143 cm away from the target. At this distance, the RCS reaches 91% of its long-distance value for a plane metal plate of radius $r_0 = \sqrt{R\lambda/3} = 12$ mm at a frequency of 1 THz (what has been also presented at Fig. 5.6). This implies that for flat objects bigger than 12 mm, the angular distribution of the scattered electric field is strongly dependent on the size of the target even within a class of objects with the same shape. A more complete reconstruction algorithm would have to take such diffraction effects into account. To further illustrate this weakness of the FBP algorithm in the form that we have applied here, we window out the intense, localized reflections from flat surfaces in the sinogram in Fig. 5.15(b), since these reflections are the main source of error. Figure 5.15(d) shows the result of the FBP algorithm after windowing. The picture is much clearer and in a better way represents all the point and edge scatterers. The depth resolution of a single angle scan is 270μm, but because FBP uses many projections for image reconstruction, both depth and lateral resolution of the reconstructed image is $270/\sqrt{2} = 191\mu$m.

Finally we have applied the FBP algorithm, with and without windowing on the data from the model aircraft sinogram in Fig. 5.12(c), and the results are shown in Fig. 5.16. The outline shape of the airplane can be easily recognized. Also particular scatterers such as fuselage, tail, wings, end of the wings and even missiles are distinguishable.

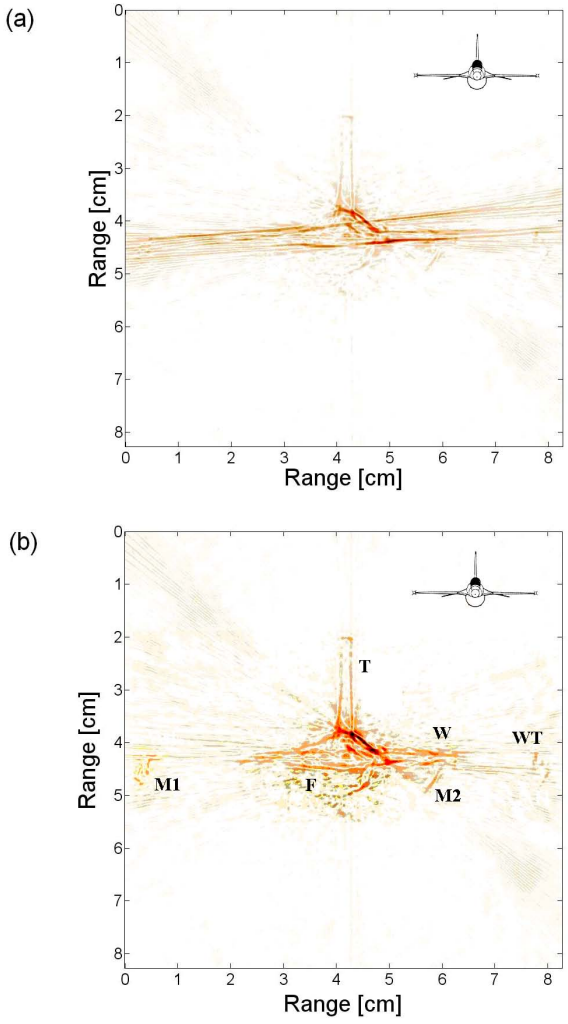

FIGURE 5.16: Projected cross section of the scale model of the F-16 aircraft reconstructed using the filtered back projection algorithm on data from Fig. 5.12(c) without (a) and with (b) windowing out flat surface reflections. Letter marks indicate positions of different scattering parts of the airplane model: wing tips (WT), wing (W), tail (T), fuselage (F) and missiles (M1, M2).

5.5 Stealth metamaterial objects characterized in the far field by Radar Cross Section measurements

Stealth technology, that includes reduction of RCS, radar jamming and deception techniques, is an ongoing trend in the design of new aircrafts, ships and ground vehicles, which aims to make them less visible (ideally invisible) to radars. For a full control over RCS, both the shape and the material that the object is made of, has to be optimized. The geometrical approach to reduction of RCS is based on using multiple angled surfaces, that reflect incoming electromagnetic radiation away from the radar - a beautiful example is Lockheed F-117 Nighthawk aircraft. Multiple surfaces that give return reflections like corner reflector should be also avoided. Complimentary approach is to use radar absorbing materials (RAM) that give low reflections. RAMs can be realized in several different ways, that include foam absorbers for anechoic chambers, cancelation of phase shifted ways reflected from multilayered materials, and radar absorbing paints. Due to their broadband absorption spectrum and planar configuration radar absorbing paints are probably most useful for the military aircraft industry. Most of RAMs are based on ferrites, which are ceramic materials with a cubic crystalline structure and chemical formula $MOFe_2O_3$, where Fe_2O_3 is iron oxide and MO refers to a combination of two or more divalent metal oxides. Different metal oxides create ferrites that exhibit different magnetic and absorptive properties. The reduction of wave reflection from ferrites is based on the fact that they can have complex magnetic permeability equal (or nearly equal) to complex dielectric constant, what results in their impedance equal to that of free space. Ferrites can provide 10 - 25 dB of absorption between 30 MHz and 1 GHz.

As we have explained in the chapter 5.1, scaling law of transforming RCS values measured at THz frequencies to the RCS values at radio frequencies is valid only if the electric properties of the material are

the same in those two frequency ranges. This condition is basically fulfilled in case of metals. For example for copper with DC conductivity of $\sigma_{DC} = 5.7 \cdot 10^7$ S/m, the THz reflectivity is 0.9972 at 1 THz, while reflectivity at 1 GHz is 0.99991 [136], which gives the difference of reflection factors smaller than $3 \cdot 10^{-3} \ll 0.99991$. The situation is more complicated for dielectric materials, for which dielectric function $\epsilon(\omega)$ may have completely different values at radio frequency and corresponding THz frequency. The lack of natural materials, which would allow for designing electromagnetic response, has led to the development of new artificial materials - metamaterials (MMs). Most metamaterials are based on a periodic arrangement of a single unit cell structure, which mimics the natural occurring crystal structure. Unit cells of metamaterials are much larger than atoms or even single molecules, but still shorter than the wavelength of the electromagnetic wave that they are designed for. The response of such metamaterial is based on electromagnetic resonances in fabricated fundamental elements, and can be tailored for specific applications. Metamaterials exhibit numerous novel effects, such as negative refractive index [217], perfect lensing [218, 219] or cloaking [220]. Fabrication and optical characterization of metamaterial films designed for THz frequencies is a very active area in the THz field [221–223]. THz MM enabled the demonstration of device concepts such as frequency-agile filters [224], absorbers [225–227], polarizers [228], modulators for THz radiation [229–231] and sensing devices [232].

In this chapter we apply a near-unity absorbing MM as a way to reduce the radar cross section of an object, and consider the real-life situation where the probe beam is significantly larger than the MM film and the object under investigation. Thus we need to be concerned not only about the intrinsic properties of the MM film, but also on scattering from edges of the object and other disturbances. The metamaterial absorber is based on the principle of minimal transmission and simultaneously, minimal reflection [225, 227]. By manipulating resonances in dielectric permittivity ϵ and magnetic permeability μ of the metamaterial independently, it is possible to absorb both the incident electric

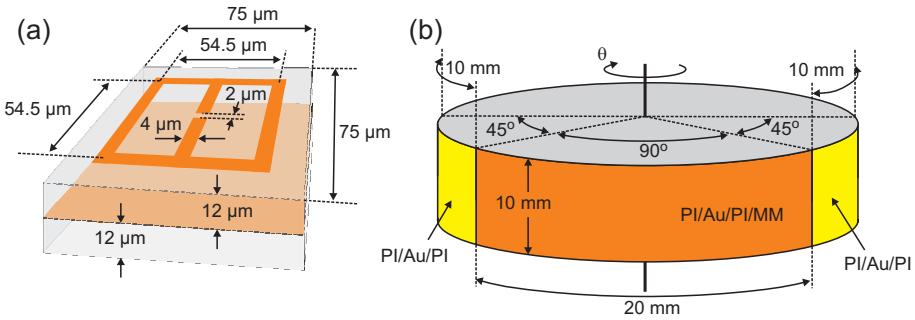

FIGURE 5.17: (a) Unit cell layout and dimensions of the metamaterial absorber. (b) Metamaterial foil wrapped around an aluminium cylinder with circumference 80 mm. PI: polyimide spacer.

and magnetic field. Additionally, by matching ϵ and μ, a metamaterial can be impedance-matched to free space, minimizing reflectivity. Tao *et al.* [226] recently designed, fabricated and characterized thin, flexible films of near-unity resonant metamaterial-based absorbers which could be wrapped around mm-sized cylinders [233]. The real-world applications of such absorbing materials are plentiful, including suppression of unwanted reflections, stealth operation, and frequency-selective filters for chemical imaging applications [234, 235]. We follow closely this design, with a geometry shown in Fig. 5.17. A 12 μm thick polyimide (PI) layer is covered with a 200 nm thick gold layer, followed by another 12 μm thick layer of PI. On top of this sandwich structure a periodic array of split-ring resonator (SRR) is defined in 200 nm thick gold by UV lithography, with SRR side lengths of 54.5 μm, capacitor gap of 2 μm, and line width of 4 μm, and a lattice period of 75 μm, as illustrated in Figure 5.17(a).

The resonant electromagnetic response to an electric field applied parallel to the central capacitor is due to the LC resonator formed by the two inductive loops on each side of the central capacitor and a dipolar response of the side conductors. For electric fields polarized perpendicularly to the central capacitor leads, a single dipole resonance is expected. The metamaterial array forms an active area of 20x10 mm, flanked by

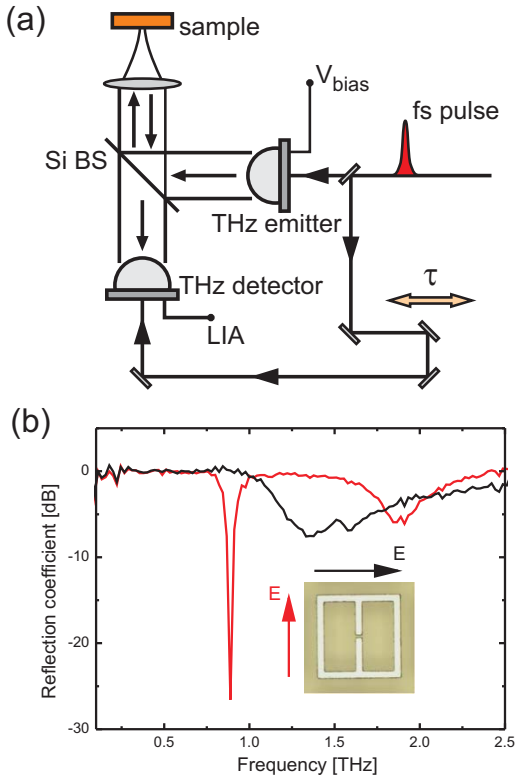

FIGURE 5.18: (a) Schematic setup for normal-incidence reflection THz-TDS. (b) Measured power reflection coefficient at normal incidence of the samples, normalized to the reflection coefficient of a blank metal surface for the two polarizations of the incident THz field: parallel (red curve) and perpendicular (black curve) to the central capacitor leads.

pads of dimensions 10x10 mm, consisting of the gold layer embedded between the PI layers but without MM structures defined on the top. The full sample of dimensions 40x10 mm is wrapped around an aluminium cylinder with circumference 80 mm and height 10 mm, thus covering exactly half of the circumference of the cylinder. The MM absorber was attached to the cylinder by double-sided sticky tape. The macroscopic sample geometry is illustrated in Fig. 5.17(b).

First, the normal-incidence reflection spectra were recorded with a reflection-type THz-TDS system based on low-temperature-grown GaAs photoconductive emitters and detectors (Menlo Systems) and driven by a femtosecond oscillator (Femtolasers Fusion 300 Pro). The experimental setup is illustrated schematically in Fig. 5.18(a). For this measurements MM sample is placed on a flat aluminum mounting plate. Briefly, the THz beam is coupled from the emitter onto the sample at normal incidence by a 2-mm thick high-resistivity silicon wafer. The reflected beam is transmitted back through the beamsplitter and directed to the detector. The spot size of the THz probe beam on the sample for this measurement is slightly below 1 mm, measured as the 10-90% rise distance of the reflection signal when scanned over a razor blade edge. The focusing is achieved by a polymer lens with 40 mm focal length.

The reflection spectrum recorded at a position close to the center of the sample active area is shown in Fig. 5.18(b), for the two polarizations of the incident THz field: parallel (red curve) and perpendicular (black curve) to the central capacitor leads. The LC resonance is seen as a sharp dip in the reflection coefficient, reaching a minimum reflectivity of -27 dB at 0.89 THz. Power transmission through the sample is estimated to be smaller than 0.0067, what has been calculated on the base of the skin depth of 80 nm [236, 237] for 1 THz radiation through a 200 nm gold layer. Power reflectivity of -27 dB with transmission $T < 0.0067$ corresponds to an absorptivity $A = 1 - R - T = 0.9913$. A second, less pronounced reflectivity minimum is seen at 1.9 THz. For the perpendicular polarization the dipole resonance is seen as a relatively broad reflectivity minimum reaching -7.5 dB at 1.35 THz. A weak,

secondary reflectivity minimum is observed at 1.6 THz. The reflectivity spectra are each normalized to the reflectivity of the blank metal surfaces at the each side of the active area.

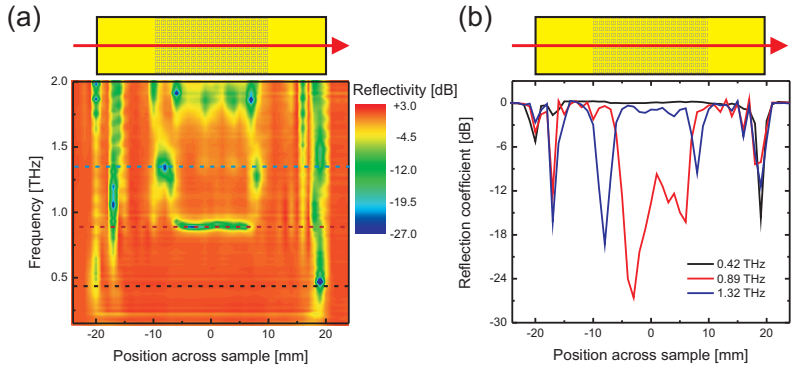

FIGURE 5.19: (a) Position-dependent power reflection spectrum of the sample along the direction indicated. (b) Position-dependent reflection coefficient at representative frequencies 0.42, 0.89 and 1.32 THz as indicated by cross-lines in (a).

In Fig. 5.19(a) we have plotted the positional dependence of the power reflectivity spectrum of the sample across its surface along the route indicated in the illustration above the diagram. The LC resonance is clearly visible at 0.89 THz in the region from -7 to +9 mm. Near the edges of the MM array the resonance is blurred and abruptly shifted to a higher frequency of 1.3 THz. While this edge effect is subjected to ongoing further investigations we believe that it is a signature of the finite size of the MM array and modified coupling between the MM cells near the edge of the sample area, due to the neighbor interactions [238]. In addition to this significant modification of the reflection spectrum we observe a slight variation across the active area of the resonance frequency of the order of 0.03 THz around the average resonance frequency of 0.89 THz. This may be due to fabrication inaccuracies of the flexible film or the subsequent significant handling of the film during repeated attachment and release on various metallic objects.

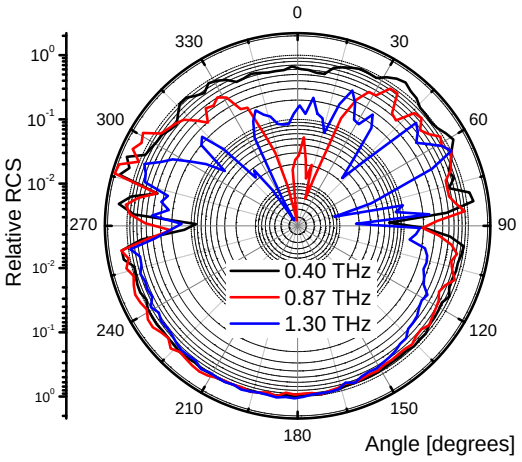

FIGURE 5.20: *RCS* measurements of the MM-covered cylinder at 0.40, 0.87, and 1.30 THz.

Figure 5.19(b) shows the positional dependence of the power reflectivity at specific frequencies (0.42, 0.89, and 1.32 THz) across the sample, as indicated by cross-lines in Fig. 5.19(a). For 0.42 THz the reflectivity is uniform except of the edges of the sample (position -20 and 20 mm), where interferences and scattering from the boundary between the sample (which is elevated due to the double-sided sticky tape beneath) and the aluminum metal surface causes the reflectivity to decrease. For 0.89 THz at the position -3 mm, reflectivity reaches minimum of -27 dB. A slight variation across the active area of the resonance frequency results in an increase of the reflectivity at the position $\sim$ 0 mm, and then its decrease at +7 mm. For 1.3 THz the reflectivity reaches minima at the edges of the MM area.

To investigate effects of the illumination with THz beam larger than the sample, we have performed radar cross section measurements on the MM sample mounted on the metal cylinder, depicted in Fig. 5.17(b) and placed in a target position in the *RCS* setup presented in Fig. 5.8(a). Results of the frequency-resolved *RCS* measurements for frequencies 0.4, 0.87 and 1.3 THz are presented in Fig. 5.20. Values of *RCS* are

normalized to the RCS of a metal cylinder (in this case 180° orientation). Here we note that the resonance frequencies between flat planar geometry (Fig. 5.19(b)) and bent cylidrycal geometry (Fig. 5.17(b)) are shifted by 0.02 THz into longer waves. For 0.4 THz the variations of RCS in Fig. 5.20 are small, and they mostly occur at the edges of the sample, where interferences and scattering causes decrease in the reflectivity. For 0.87 THz, the minimal RCS of 0.0026 is achieved for sample orientation of $-8°$. RCS of 0.0026 corresponds well to the reduction of reflectivity in the planar geometry by -27 dB (-27 dB $= 0.002 = 1/384$). For 1.3 THz, RCS has two minima: one at $-32°$ and the second one at $+8°$. In general the shape of the RCS for those three frequencies is very similar to the shape of the reflectivity across the sample, as shown in Fig. 5.19(b). Here we show that significant reduction of RCS is possible, even though the MM sample is bent to accommodate for the round shape of the cylinder, and even though the THz beam that is used for illumination of the structure is larger then the size of the structure, and interferences between THz radiation originating at different part of the structure are present.

Recently a dual band terahertz metamaterial absorbers have been designed and manufactured [239, 240]. The dual band absorber consists of a dual electric-field-coupled resonator on a metallic plane. Individual fine tuning of the two absorption resonances can be achieved by individually adjusting each electric-field-coupled resonator geometry, and in this way providing possibility for even larger freedom in designing object with decreased RCS in even broader frequency range.

5.6 Conclusions

We have presented a method for bistatic RCS measurements using THz waves. The calibrated setup has resolution of 0.2 mm. We have performed a series of RCS measurements in the polar and azimuthal orientation on a scale model of the fighter aircrafts F-16 and F-35. By

scaling wavelengths and models to real-scale platforms we can make detailed comparisons to RCS of real sized aircrafts at standard MHz/GHz frequencies. The application of a time domain system allows not only for determination of the total RCS but it also provides RCS values of particular elements of the model. Using the filtered back projection algorithm we are able to reconstruct a two-dimensional (and in principle also three-dimensional) visualization of all the scattering points. Our results show need for better algorithms, which could take into account the shape of the object and could compensate for diffraction, for improving the quality of reconstructed images. Furthermore we have investigated properties of flexible metamaterial absorbers, that allow for designing electromagnetic response according to our requirements. We have shown that reduction of RCS by factor of nearly 400 at the frequency of 0.87 THz is possible. Possibility of designing and manufacturing MM according to our requirements, makes them ideal for simulating stealth materials in the THz frequency range.

Chapter 6

Conclusions and outlook

This thesis has been dealing with chosen aspects of THz technology that can have defense and security-related applications. In chapter 2 we have presented a short review of the current THz technologies, used for purposes of this thesis. The review included a brief description of THz sources, with a focus on high intensity THz generation using the tilted wavefront technique. A summary of possible detection schemes for THz experiments has been also presented.

In this thesis we have developed a novel method for simultaneous data acquisition in time-resolved terahertz spectroscopy experiments, based on the simultaneous double modulation of the probe and pump beams. We have applied this method to extract the sheet conductivity of photoexcited carriers in SI GaAs and compared the results with those of a standard data acquisition scheme. We have shown that application of the new method minimizes errors in spectrally resolved photoconductivity data originating from fluctuations in the laser system output and timing errors in the THz pulse detection. Furthermore we have demonstrated that the new organic material, BNA, is a very strong and broadband THz emitter, which enabled us to carry out spectroscopy with a bandwidth twice as large (from 0.1 to nearly 6 THz) as conventional

spectroscopy in the field. Fast development of high power THz sources will make advanced techniques such as all-THz pump-probe [241–243] and even two dimensional nonlinear THz spectroscopy accessible in the near future. Those techniques will allow for investigation of yet poorly-understood anharmonic interactions between different phonon modes in molecular crystals including explosives and related compounds. Nonlinear interactions and energetic coupling between lattice vibrations will not only open a new big block of fundamental science, but will also provide additional information about the investigated sample and its environment. This extra information can allow for example for more accurate discrimination between different compounds that might have similar linear phonon spectrum. 2D nonlinear THz spectroscopy is a very challenging technique and only experiments in the mid infrared, have been performed [45, 244]. For that reason at first we have concentrated on time-resolved terahertz spectroscopy, which in its pump-probe nature is a simplified linear version of the 2D THz spectroscopy. Before 2D spectroscopy will be realized it is essential to be sure that the extracted data correspond to the physical reality. According to our predictions the technique of simultaneous data acquisition can also be adapted and used for the THz 2D spectroscopy.

The need for high intensity sources of THz radiation directed our focus on possible ways of enhancing THz field in different waveguide structures. As a result we have manufactured a tapered parallel plate waveguide consisting of two aluminium plates of a varying width and a varying plate separation. To fully understand field dynamics inside the waveguide, we have developed a novel non-invasive broadband method of imaging the THz electric field inside PPWGs. The method is based on nonlinear interaction between NIR probe pulse and a THz transient in the presence of external oscillating bias. The interaction leads to the generation of THz-enhanced second harmonic of a near-infrared probe pulse, which can be measured and related to the value of THz field in an absolute and calibrated manner. The method does not disturb the

propagating THz field as exemplified by the measurement of the THz reflection coefficient from the tip of the waveguide. The resolution of the method is restricted by the geometrical dimensions of the NIR probe focus spot only, while the frequency response depends on the interaction length between THz and the NIR probe. Next we investigated field enhancement properties of the TPPWG. Analytical and numerical approaches are compared and based on the differences diffraction losses are estimated. We show that a field enhancement factor of over 20 is possible, resulting in a THz peak electric field exceeding 1.4 MV/cm for the output gaps of 20 μm, which is a significant fraction of molecular field inside crystals. Obtained values are verified using two independent methods and agree well with numerical predictions. Even higher values of the THz electric field are expected for smaller output gaps, and further work needs to be done to find limits of this field enhancement.

High values of electric field opens exciting possibilities of THz nonlinear processes. One extremely interesting phenomena would be overcoming the work function of a metal by the ponderomotive potential of high intensity THz wave. The work function is the minimum energy needed to remove an electron from a solid to a point immediately outside the solid surface. For example for aluminum the work force is 4.08 eV, for silver 4.7 eV and for gold 5.1 eV [245]. The ponderomotive energy is the cycle-averaged energy of a free electron in an electric field. The ponderomotive energy is given by $U_p = \frac{e^2 E^2}{4m\omega^2}$, where E is the amplitude of the electric field, m is mass of electron and ω is the frequency of electro-magnetic radiation. For 1 MV/cm peak field THz wave of a central frequency of 1 THz, the ponderomotive potential is 11.1 eV and is bigger than the work function. It would be very interesting to investigate if so high ponderomotive potential is able to remove the electron from the metal. The electric field of the TEM mode in the PPWG is perpendicular to the metal plate, so if such effect is achievable then the free electron would be accelerated by the electric field and travel to the other plate causing microscopic current. Because of the field enhancement and TEM mode

propagation, the TPPWG structure seems to be ideal for investigation of the described phenomena.

The measurement of the radar cross section of a target is a standard technique in the GHz region, particularly important for military and defense-related purposes including detection and identification of unknown targets as well as for countermeasures. In chapter 5 we have presented a method for bistatic RCS measurements using THz waves. By employing scaling laws we are able to scale values measured in the low THz range (0.1-2 THz) into values that would be measured at radar frequencies. The access to high intensity THz pulses, generated by tilted wavefront optical rectification, allowed for determination of THz RCS of small scattering centers. The calibrated setup is able to detect object smaller than 1 mm-diameter metal sphere. The range resolution of the setup is 0.27 mm and cross range resolution 0.19 mm. We have performed a series of RCS measurements in the polar and azimuthal orientation on scales model of the aircraft fighters F-16 and F-35. By scaling wavelengths and models to real-scale platforms we can make detailed comparisons to RCS of real sized aircrafts at standard MHz/GHz frequencies. The application of a time domain system allows not only for determination of the total RCS but it also provides RCS values of particular elements of the model. Using the filtered back projection algorithm we are able to reconstruct a two-dimensional (and in principle also three-dimensional) visualization of all the scattering points. Our results show need for better algorithms, which could take into account the shape of the object and could compensate for diffraction, for improving the quality of reconstructed images. To have a better control over the measured RCS we have investigated possibility of using metamaterials (MMs). We have showed that using MM perfect absorbers significant reduction of RCS can be achieved. Possibility of designing and manufacturing MM according to requirements, makes them ideal for simulating stealth materials in the THz frequency range. Elasticity of produced MM structures opens door for placing them on curved surfaces. Further work on different techiques for depositing MM on the surfaces of

investigated targets is still required. Next class of interesting problems concerning THz RCSs is the influence of the environment on the result of measurements and capability of simulating real life scenarios in the THz frequency range.

Appendix A

Acknowledgements

During the past three years of my PhD studies at DTU Fotonik, I had a chance to meet, know and work with many wonderful people, without whom this thesis would probably have never been written.

First I would like to express my gratitude to my supervisors, **Peter Uhd Jepsen** from DTU Fotonik and **Henning Heiselberg** from Danish Defense Acquisition and Logistics Organization for their supervision, advice, and guidance from the very early stage of this research, as well as giving me extraordinary experiences throughout the work. Peter showed me that a real scientist always finds a passion in his job.

I am highly indebted to all present and former members of the Terahertz and Biophotonic Group at DTU Fotonik. I would like to mention few of them. First of all thanks to **David Cooke**, whom I had a chance to work with for over two years. It is Dave who thought me how to align the laser, it is with him that I have done my first terahertz experiments, and it is him who helped me interpret the first THz data. Special thanks to **Henrik Porte**, my fellow PhD colleague whom I worked with the whole duration of my PhD program and who recently received his PhD. We have spent with Henrik countless hours in the lab and had countless conversations, which for sure benefited my work. I would like to

thank **Andrei Andryieuski** for patiently performing all the numerical simulations of the tapered parallel plate waveguide. Thanks to **Dmirty Turchinovich** for lot of simulating discussions and ideas. I want to thank **Binbin Zhou** for fixing so many laser problems and his advise with autocorrelation measurements. I would like to thank all my colleagues and friends who were involved in proofreading of this thesis.

I would like to thank people from Rensselaer Polytechnic Insitute in Troy, USA, where I had a chance to work for nearly 5 months. First of all to **Xi-Cheng Zhang**, director of Center for THz Research who gave me the opportunity to work in his group. Second to **Jianming Dai** for his patient assistance in the lab and help with laser issues. Special thanks for all the grad students at the Center for Terahertz Research for extremely stimulating scientific discussions, help in the lab and friendly atmosphere which helped me survive a cold North-American winter.

A special thanks to **Martin Nielsen** and **Frank Persson** from mechanical workshop at DTU Electro for manufacturing many of the curtail parts of my systems. They used high precision even with parts that were asked for with a short notice, improving the results of this thesis.

I would like to thank **all my friends** from all over the world. Time with you even though not connected to scientific research has helped me keep a healthy balance between work and personal life. Thanks to everyone from **Copenhagen Mermates**, my swimming and triathlon team, for motivating me to do sport, and, to stay fit and healthy. Last but not least I would like to thank my **family** for support which I could always feel even being thousands of kilometers away.

Appendix B

Ph.D. Publications

B.1 Peer Reviewed Journal

1. Krzysztof Iwaszczuk, Andrei Andryieuski, Andrei Lavrinenko, Xi-Cheng Zhang and Peter Uhd Jepsen, "Non-invasive terahertz field imaging inside parallel plate waveguides," *Applied Physics Letters* **99**, 071113 (2011).

2. Krzysztof Iwaszczuk, Henning Heiselberg, Peter Uhd Jepsen, "Terahertz radar cross section measurements," *Optics Express* **18**, 26399 (2010).

3. Krzysztof Iwaszczuk, David Cooke, Masazumi Fujiwara, Hideki Hashimoto and Peter Uhd Jepsen, "Simultaneous reference and differential waveform acquisition in time-resolved terahertz spectroscopy," *Optics Express* **17**, 21969 (2009).

4. Krzysztof Iwaszczuk, Andrei Andryieuski, Andrei Lavrinenko, Xi-Cheng Zhang and Peter Uhd Jepsen, "Terahertz field enhancement using tapered parallel plate waveguides," (in preparation).

5. Krzysztof Iwaszczuk, Andrew C. Strikwerda, Kim Fan, Xi Zhang, Richard D. Averitt, and Peter Uhd Jepsen, "Flexible terahertz absorbers for stealth applications," Optics Express, (in preparation).

6. Krzysztof Iwaszczuk, Binbin Zhou, Morten Bache and Peter Uhd Jepsen "Spectral compression of intense sub-picosecond pulses," (in preparation).

B.2 Conference Contributions

7. Krzysztof Iwaszczuk, Andrei Andryieuski, Andrei Lavrinenko, Xi-Cheng Zhang and Peter Uhd Jepsen, " Non-invasive method of field imaging in parallel plate waveguides," presentation and a proceedings publication at the 36th International Conference on Infrared, Millimeter and THz waves, Huston, USA, October 2011 (**proceedings + talk**).

8. Krzysztof Iwaszczuk, Kim Fan, Andrew C. Strikwerda, Xi Zhang, Richard D. Averitt, and Peter Uhd Jepsen, "Radar Cross Section measurements on the stealth metamaterial objects," Danish Physical Society Meeting, Nyborg, Denmark, June 2011 (**poster**).

9. Krzysztof Iwaszczuk, Andrei Andryieuski, Andrei Lavrinenko, Xi-Cheng Zhang and Peter Uhd Jepsen, "Terahertz field imaging inside tapered parallel plate waveguides," THz Science and Technology - The Castle Meeting, Schloss Rauischholzhausen, Germany, June 2012 (**poster**).

10. Krzysztof Iwaszczuk, Kim Fan, Andrew C. Strikwerda, Xi Zhang, Richard D. Averitt, and Peter Uhd Jepsen, "Stealth metamaterial objects characterized in the far field by Radar Cross Section measurements", poster and a proceedings publication at International Workshop on Optical Terahertz Science and Technology, Santa Barbara, California, USA, March 2011 (**poster**).

11. Krzysztof Iwaszczuk and Peter Uhd Jepsen, "Defense and security-related applications of THz radiation," Militaer Teknisk Forening (MTF), Copenhagen, April 2011 (**talk**).

12. - Krzysztof Iwaszczuk, Henning Heiselberg, Peter Uhd Jepsen "Terahertz radar cross secition measurements," keynote presentation and a proceedings publication at the 35th International Conference on Infrared, Millimeter and THz waves, Rome, Italy, September 2010 (**proceedings + keynote talk**).

13. Krzysztof Iwaszczuk, Henning Heiselberg, and Peter Uhd Jepsen, "Terahertz radar cross section measurements," Sensors and Electronics Technology Panel Specialists Meeting, Terahertz and other electromagnetic wave techniques for defence and security (SET) - 159, Vilnius, Lithuania, 2010 (**proceedings + talk**).

14. Krzysztof Iwaszczuk and Peter Uhd Jepsen, "DTU THz activities," Sensors and Electronics Technology Panel Specialists Meeting, Terahertz and other electromagnetic wave techniques for defence and security (SET) - 124 meeting, Rome, Italy, May 2009 (**talk**).

15. Krzysztof Iwaszczuk, David Cooke and Peter Uhd Jepsen, "Broadband high power THz generation," 1 Nordic Meeting in Physics, 2009, DTU, Lyngby, Denmark (**poster**).

16. David Cooke, Krzysztof Iwaszczuk, Kristian Nielsen, Ole Bang and Peter Uhd Jepsen, "Broadband THz waveguiding and high-precision broadband time-resolved spectroscopy," International Workshop on Terahertz Technology (TeraTech) - 2 , 2I-B5, 2009, Osaka, Japan (**Invited conference contribution**).

B.3 Book chapters

17. Krzysztof Iwaszczuk, Henrik Porte, Rasmus Kjelsmark Olsson, David Cooke, Dmitry Turchinovich and Peter Uhd Jepsen, "Terahertz technology : terahertz sources and detectors," Chapeter in "Beyond optical horizons, today and tomorrow with photonics," pp. 113-129, DTU Fotonik, Kgs. Lyngby (2009).

Bibliography

[1] P. U. Jepsen, D. G. Cooke, and M. Koch. Terahertz spectroscopy and imaging - modern techniques and applications. *Laser & Photonics Reviews*, 5(1):124–166, January 2011.

[2] Jason B. Baxter and Glenn W. Guglietta. Terahertz spectroscopy. *Anal. Chem.*, 83(12):4342–4368, 2011.

[3] M.R. Scarfi, M. Romano, R. Di Pietro, O. Zeni, A. Doria, G.P. Gallerano, E. Giovenale, G. Messina, A. Lai, G. Campurra, D. Coniglio, and M. D'Arienzo. THz exposure of whole blood for the study of biological effects on human lymphocytes. *J. BIOL. PHYS.*, 29:171–176, 2003.

[4] R.H. Clothier and N. Bourne. Effects of THz exposure on human primary keratinocyte differentiation and viability. *J. BIOL. PHYS.*, 29:179–185, 2003.

[5] B. E. Cole, J. B. Williams, B. T. King, M. S. Sherwin, and C. R. Stanley. Coherent manipulation of semiconductor quantum bits with terahertz radiation. *Nature*, 410(6824):60–63, March 2001.

[6] R. Huber, F. Tauser, A. Brodschelm, M. Bichler, G. Abstreiter, and A. Leitenstorfer. How many-particle interactions develop after ultrafast excitation of an electron-hole plasma. *Nature*, 414(6861):286–289, November 2001.

[7] S. Leinß, T. Kampfrath, K. v.Volkmann, M. Wolf, J. T. Steiner, M. Kira, S. W. Koch, A. Leitenstorfer, and R. Huber. Terahertz coherent control of optically dark paraexcitons in Cu_2O. *Phys. Rev. Lett.*, 101:246401, Dec 2008.

[8] M. Schall, M. Walther, and P. Uhd Jepsen. Fundamental and second-order phonon processes in CdTe and ZnTe. *Phys. Rev. B*, 64:094301, Aug 2001.

[9] Markus Walther, Bernd M. Fischer, and P. Uhd Jepsen. Noncovalent intermolecular forces in polycrystalline and amorphous saccharides in the far infrared. *Chem. Phys.*, 288(2-3):261 – 268, 2003.

[10] C Ronne, L Thrane, PO Astrand, A Wallqvist, KV Mikkelsen, and SR Keiding. Investigation of the temperature dependence of dielectric relaxation in liquid water by THz reflection spectroscopy and molecular dynamics simulation. *J. Chem. Phys.*, 107(14):5319–5331, OCT 8 1997.

[11] Charles A. Schmuttenmaer. Exploring dynamics in the far-infrared with terahertz spectroscopy. *ChemInform*, 35(24):no–no, 2004.

[12] Michael Schall and Peter Uhd Jepsen. Photoexcited GaAs surfaces studied by transient terahertz time-domain spectroscopy. *Opt. Lett.*, 25(1):13–15, Jan 2000.

[13] K. P. H. Lui and F. A. Hegmann. Ultrafast carrier relaxation in radiation-damaged silicon on sapphire studied by optical-pump-terahertz-probe experiments. *Appl. Phys. Lett.*, 78(22):3478 –3480, may 2001.

[14] D. G. Cooke, A. N. MacDonald, A. Hryciw, J. Wang, Q. Li, A. Meldrum, and F. A. Hegmann. Transient terahertz conductivity in photoexcited silicon nanocrystal films. *Phys. Rev. B*, 73(19):193311, May 2006.

[15] Masayoshi Tonouchi. Cutting-edge terahertz technology. *Nat Photon*, 1(2):97–105, February 2007.

[16] Hai-Bo Liu, Hua Zhong, N. Karpowicz, Yunqing Chen, and Xi-Cheng Zhang. Terahertz spectroscopy and imaging for defense and security applications. *Proceedings of the IEEE*, 95(8):1514 –1527, aug. 2007.

[17] Martin Koch. Terahertz communications: A 2020 vision. In Robert Miles, Xi-Cheng Zhang, Heribert Eisele, and Arunas Krotkus, editors, *Terahertz Frequency Detection and Identification of Materials and Objects*, volume 19 of *NATO Security through Science Series*, pages 325–338. Springer Netherlands, 2007.

[18] Ernest V. Loewenstein. The history and current status of fourier transform spectroscopy. *Appl. Opt.*, 5(5):845–854, May 1966.

[19] K. D. M. Moeller and W. G. Rothschild. *Far-Infrared Spectroscopy.* Wiley Interscience, 1971.

[20] Jam Farhoomand and Herbert M. Pickett. Stable 1.25 Watts CW far infrared laser radiation at the 119 μm methanol line. *International Journal of Infrared and Millimeter Waves*, 8:441–447, 1987. 10.1007/BF01013257.

[21] D. H. Auston. Picosecond optoelectronic switching and gating in silicon. *Appl. Phys. Lett.*, 26(3):101–103, 1975.

[22] Martin van Exter, Ch. Fattinger, and D. Grischkowsky. Terahertz time-domain spectroscopy of water vapor. *Opt. Lett.*, 14(20):1128–1130, Oct 1989.

[23] P. F. Moulton. Spectroscopic and laser characteristics of ti:al2o3. *J. Opt. Soc. Am. B*, 3(1):125–133, Jan 1986.

[24] J.D. Kafka, M.L. Watts, and J.-W.J. Pieterse. Picosecond and femtosecond pulse generation in a regeneratively modelocked ti:sapphire laser. *Quantum Electronics, IEEE Journal of*, 28(10):2151 –2162, oct 1992.

[25] D. W. Faries, K. A. Gehring, P. L. Richards, and Y. R. Shen. Tunable far-infrared radiation generated from the difference frequency between two ruby lasers. *Phys. Rev.*, 180:363–365, Apr 1969.

[26] K. H. Yang, P. L. Richards, and Y. R. Shen. Generation of far infrared radiation by picosecond light pulses in linbo3. *Appl. Phys. Lett.*, 19(9):320–323, 1971.

[27] Q. Wu and X.-C. Zhang. Free-space electro-optic sampling of terahertz beams. *Appl. Phys. Lett.*, 67(24):3523–3525, 1995.

[28] P. Uhd Jepsen, C. Winnewisser, M. Schall, V. Schyja, S. R. Keiding, and H. Helm. Detection of thz pulses by phase retardation in lithium tantalate. *Phys. Rev. E*, 53(4):R3052–R3054, Apr 1996.

[29] Ajay Nahata, David H. Auston, Tony F. Heinz, and Chengjiu Wu. Coherent detection of freely propagating terahertz radiation by electro-optic sampling. *Appl. Phys. Lett.*, 68(2):150–152, 1996.

[30] Q. Wu and X.-C. Zhang. Ultrafast electro-optic field sensors. *Appl. Phys. Lett.*, 68(12):1604–1606, 1996.

[31] D. J. Cook and R. M. Hochstrasser. Intense terahertz pulses by four-wave rectification in air. *Opt. Lett.*, 25(16):1210–1212, Aug 2000.

[32] Jianming Dai, Xu Xie, and X.-C. Zhang. Detection of broadband terahertz waves with a laser-induced plasma in gases. *Phys. Rev. Lett.*, 97(10):103903, Sep 2006.

[33] Jingle Liu, Jianming Dai, See Leang Chin, and ZhangX.-C. Broadband terahertz wave remote sensing using coherent manipulation of fluorescence from asymmetrically ionized gases. *Nat Photon*, 4(9):627–631, September 2010.

[34] Nicholas Karpowicz, Jianming Dai, Xiaofei Lu, Yunqing Chen, Masashi Yamaguchi, Hongwei Zhao, X.-C. Zhang, Liangliang Zhang, Cunlin Zhang, Matthew Price-Gallagher, Clark Fletcher, Orval Mamer, Alain Lesimple, and Keith Johnson. Coherent heterodyne time-domain spectrometry covering the entire terahertz gap. *Appl. Phys. Lett.*, 92(1):011131, 2008.

[35] Andrei G. Stepanov, Jnos Hebling, and Jrgen Kuhl. Efficient generation of subpicosecond terahertz radiation by phase-matched optical rectification using ultrashort laser pulses with tilted pulse fronts. *Appl. Phys. Lett.*, 83(15):3000–3002, 2003.

[36] Matthias C Hoffmann and Jozsef A. Fulop. Intense ultrashort terahertz pulses: generation and applications. *J. Phys. D: Appl. Phys.*, 44(8):083001, 2011.

[37] X. Xin, H. Altan, A. Saint, D. Matten, and R. R. Alfano. Terahertz absorption spectrum of para and ortho water vapors at different humidities at room temperature. *J. Appl. Phys.*, 100(9):094905, 2006.

[38] Takeshi Yasui, Eisuke Saneyoshi, and Tsutomu Araki. Asynchronous optical sampling terahertz time-domain spectroscopy for ultrahigh spectral resolution and rapid data acquisition. *Appl. Phys. Lett.*, 87(6):061101, 2005.

[39] C. Janke, M. Först, M. Nagel, H. Kurz, and A. Bartels. Asynchronous optical sampling for high-speed characterization of integrated resonant terahertz sensors. *Opt. Lett.*, 30(11):1405–1407, Jun 2005.

[40] O. Morikawa, M. Tonouchi, and M. Hangyo. A cross-correlation spectroscopy in subterahertz region using an incoherent light source. *Appl. Phys. Lett.*, 76(12):1519–1521, 2000.

[41] Maik Scheller and Martin Koch. Terahertz quasi time domain spectroscopy. *Opt. Express*, 17(20):17723–17733, Sep 2009.

[42] Kohji Yamamoto, Mariko Yamaguchi, Fumiaki Miyamaru, Masahiko Tani, Masanori Hangyo, Takeshi Ikeda, Akira Matsushita, Kenji Koide, Michiaki Tatsuno, and Yukio Minami. Noninvasive inspection of C-4 explosive in mails by terahertz time-domain spectroscopy. *Jpn. J. Appl. Phys.*, 43(3B):L414–L417, 2004.

[43] Feng Huang, Brian Schulkin, Hakan Altan, John F. Federici, Dale Gary, Robert Barat, David Zimdars, Minghan Chen, and D. B. Tanner. Terahertz study of 1,3,5-trinitro-s-triazine by time-domain and fourier transform infrared spectroscopy. *Appl. Phys. Lett.*, 85(23):5535–5537, 2004.

[44] T. M. Goyette J. C. Dickinson R. H. Giles W Goodhue W. Waldman W. E. Nixon A. J. Gatesman, A. Danylov and W. Hoen. Terahertz behaviour of optical components and common materials. *SPIE*, 6212, 2006.

[45] W. Kuehn, K. Reimann, M. Woerner, and T. Elsaesser. Phase-resolved two-dimensional spectroscopy based on collinear n-wave mixing in the ultrafast time domain. *J. Chem. Phys.*, 130(16):164503, 2009.

[46] G. Vaillancourt, T. B. Norris, J. S. Coe, P. Bado, and G. A. Mourou. Operation of a 1-kHz pulse-pumped ti:sapphire regenerative amplifier. *Opt. Lett.*, 15(6):317–319, Mar 1990.

[47] Donna Strickland and Gerard Mourou. Compression of amplified chirped optical pulses. *Opt. Commun.*, 56(3):219 – 221, 1985.

[48] F. J. McClung and R. W. Hellwarth. Giant optical pulsations from ruby. *J. Appl. Phys.*, 33(3):828–829, 1962.

[49] J. A. Armstrong. Measurement of picosecond laser pulse widths. *Appl. Phys. Lett.*, 10(1):16–18, 1967.

[50] M. Maier, W. Kaiser, and J. A. Giordmaine. Intense light bursts in the stimulated Raman effect. *Phys. Rev. Lett.*, 17:1275–1277, Dec 1966.

[51] F. Salin, P. Georges, G. Roger, and A. Brun. Single-shot measurement of a 52-fs pulse. *Appl. Optics*, 26(21):4528–4531, Nov 1987.

[52] J. Horvat and R. A. Lewis. Peeling adhesive tape emits electromagnetic radiation at terahertz frequencies. *Opt. Lett.*, 34(14):2195–2197, Jul 2009.

[53] D. T. Hodges, F. B. Foote, and R. D. Reel. Efficient high-power operation of the cw far-infrared waveguide laser. *Appl. Phys. Lett.*, 29(10):662–664, 1976.

[54] Benjamin S. Williams. Terahertz quantum-cascade lasers. *Nat Photon*, 1(9):517–525, September 2007.

[55] B. F. J. Zuidberg and A. Dymanus. High-order submillimeter mixing in point-contact and schottky diodes. *Appl. Phys. Lett.*, 29(10):643–645, 1976.

[56] W. H. Haydl, S. Smith, and R. Bosch. 100 GHz Gunn diodes fabricated by molecular beam epitaxy. *Appl. Phys. Lett.*, 37(6):556–557, 1980.

[57] G. P. Williams. FAR-IR/THz radiation from the jefferson laboratory, energy recovered linac, free electron laser. *Rev. Sci. Instrum.*, 73(3):1461–1463, 2002.

[58] Y. Shen, T. Watanabe, D. A. Arena, C.-C. Kao, J. B. Murphy, T. Y. Tsang, X. J. Wang, and G. L. Carr. Nonlinear cross-phase modulation with intense single-cycle terahertz pulses. *Phys. Rev. Lett.*, 99(4):043901–4, July 2007.

[59] Gwyn P Williams. Filling the THz gap - high power sources and applications. *Reports on Progress in Physics*, 69(2):301, 2006.

[60] D. H. Auston, K. P. Cheung, and P. R. Smith. Picosecond photoconducting hertzian dipoles. *Appl. Phys. Lett.*, 45(3):284–286, 1984.

[61] D. H. Auston, K. P. Cheung, J. A. Valdmanis, and D. A. Kleinman. Cherenkov radiation from femtosecond optical pulses in electro-optic media. *Phys. Rev. Lett.*, 53:1555–1558, Oct 1984.

[62] Ch. Fattinger and D. Grischkowsky. Terahertz beams. *Appl. Phys. Lett.*, 54(6):490–492, 1989.

[63] P.R. Smith, D.H. Auston, and M.C. Nuss. Subpicosecond photoconducting dipole antennas. *Quantum Electronics, IEEE Journal of*, 24(2):255 –260, feb 1988.

[64] A. C. Warren, J. M. Woodall, J. L. Freeouf, D. Grischkowsky, D. T. McInturff, M. R. Melloch, and N. Otsuka. Arsenic precipitates and the semi?insulating properties of gaas buffer layers grown by low?temperature molecular beam epitaxy. *Appl. Phys. Lett.*, 57(13):1331–1333, 1990.

[65] I. S. Gregory, C. Baker, W. R. Tribe, M. J. Evans, H. E. Beere, E. H. Linfield, A. G. Davies, and M. Missous. High resistivity annealed low-temperature gaas with 100 fs lifetimes. *Appl. Phys. Lett.*, 83(20):4199–4201, 2003.

[66] Masato Suzuki and Masayoshi Tonouchi. Fe-implanted ingaas photoconductive terahertz detectors triggered by 1.56 μm femtosecond optical pulses. *Appl. Phys. Lett.*, 86(16):163504, 2005.

[67] N. Chimot, J. Mangeney, L. Joulaud, P. Crozat, H. Bernas, K. Blary, and J. F. Lampin. Terahertz radiation from heavy-ion-irradiated $in_0.53ga_0.47as$ photoconductive antenna excited at 1.55 μm. *Appl. Phys. Lett.*, 87(19):193510, 2005.

[68] M. Bass, P. A. Franken, J. F. Ward, and G. Weinreich. Optical rectification. *Phys. Rev. Lett.*, 9(11):446–448, Dec 1962.

[69] F. Blanchard, L. Razzari, H.C. Bandulet, G. Sharma, R. Morandotti, J. C. Kieffer, T. Ozaki, M. Reid, H. F. Tiedje, H. K. Haugen, and F. A. Hegmann. Generation of 1.5 μj single-cycle terahertz pulses by optical rectification from a large aperture ZnTe crystal. *Opt. Express*, 15(20):13212–13220, Oct 2007.

[70] P. Y. Han, M. Tani, F. Pan, and X.-C. Zhang. Use of the organic crystal DAST for terahertz beam applications. *Opt. Lett.*, 25:675, 2000.

[71] J. O. White, D. Hulin, M. Joffre, A. Migus, A. Antonetti, E. Toussaere, R. Hierle, and J. Zyss. Ultrabroadband second harmonic generation in organic and inorganic thin crystals. *Appl. Phys. Lett.*, 64(3):264–266, 1994.

[72] John J. Carey, Ray T. Bailey, D. Pugh, J. N. Sherwood, F. R. Cruickshank, and Klaas Wynne. Terahertz pulse generation in an organic crystal by optical rectification and resonant excitation of molecular charge transfer. *Appl. Phys. Lett.*, 81(23):4335–4337, 2002.

[73] Hideki Hashimoto, Hironori Takahashi, Takashi Yamada, Kazuyoshi Kuroyanagi, and Takayoshi Kobayashi. Characteristics of the terahertz radiation from single crystals of n -substituted 2-methyl-4-nitroaniline. *J. Phys.: Condens. Matter*, 13(23):L529, 2001.

[74] Kazuyoshi Kuroyanagi, Masazumi Fujiwara, Hideki Hashimoto, Hironori Takahashi, Shin ichiro Aoshima, and Yutaka Tsuchiya. All organic terahertz electromagnetic wave emission and detection using highly purified *N*-benzyl-2-methyl-4-nitroaniline crystals. *Jpn. J. Appl. Phys.*, 45(5A):4068–4073, 2006.

[75] Masazumi Fujiwara, Kazuhiro Yanagi, Minoru Maruyama, Mitsuru Sugisaki, Kazuyoshi Kuroyanagi, Hironori Takahashi, Shin ichiro Aoshima, Yutaka Tsuchiya, Andrew Gall, and Hideki Hashimoto. Second order nonlinear optical properties of the single crystal of *N*-benzyl 2-methyl-4-nitroaniline: Anomalous enhancement of the d_{333} component and its possible origin. *Jpn. J. Appl. Phys.*, 45(11):8676–8685, 2006.

[76] Masazumi Fujiwara, Minoru Maruyama, Mitsuru Sugisaki, Hironori Takahashi, Shin ichiro Aoshima, Richard J. Cogdell, and Hideki Hashimoto. Determination of the *d*-tensor components of a single crystal of *N*-benzyl-2-methyl-4-nitroaniline. *Jpn. J. Appl. Phys.*, 46(4A):1528–1530, 2007.

[77] Kazuyoshi Kuroyanagi, Masazumi Fujiwara, Hideki Hashimoto, Hironori Takahashi, Shin ichiro Aoshima, and Yutaka Tsuchiya. Determination of refractive indices and absorption coefficients of highly purified *N*-benzyl-2-methyl-4-nitroaniline crystal in terahertz frequency regime. *Jpn. J. Appl. Phys.*, 45(29):L761–L764, 2006.

[78] Katsuhiko Miyamoto, Hiroaki Minamide, Masazumi Fujiwara, Hideki Hashimoto, and Hiromasa Ito. Widely tunable terahertz-wave generation using an n-benzyl-2-methyl-4-nitroaniline crystal. *Opt. Lett.*, 33(3):252–254, Feb 2008.

[79] J. Hebling, A.G. Stepanov, G. Almsi, B. Bartal, and J. Kuhl. Tunable thz pulse generation by optical rectification of ultrashort laser pulses with tilted pulse fronts. *Appl. Phys. B: Lasers Opt.*, 78:593–599, 2004. 10.1007/s00340-004-1469-7.

[80] K.-L. Yeh, M. C. Hoffmann, J. Hebling, and Keith A. Nelson. Generation of 10μj ultrashort terahertz pulses by optical rectification. *Appl. Phys. Lett.*, 90(17):171121, 2007.

[81] O. E. Martinez. Grating and prism compressors in the case of finite beam size. *J. Opt. Soc. Am. B*, 3(7):929–934, July 1986.

[82] J. A. Fülöp, L. Pálfalvi, G. Almási, and J. Hebling. Design of high-energy terahertz sources based on optical rectification. *Opt. Express*, 18(12):12311–12327, Jun 2010.

[83] P. L. Richards. Bolometers for infrared and millimeter waves. *J. Appl. Phys.*, 76(1):1–24, 1994.

[84] M. J. E. Golay. A pneumatic infra-red detector. *Rev. of Sci. Intr.*, 18:357–362, 1947.

[85] Gael Sebald, Daniel Guyomar, and Amen Agbossou. On thermoelectric and pyroelectric energy harvesting. *Smart Materials and Structures*, 18(12):125006, 2009.

[86] S. M. Sze. *Semiconductor Devices*. John Wiley and Sons, Physics and Technology, 1984.

[87] D. Grischkowsky, Søren Keiding, Martin van Exter, and Ch. Fattinger. Far-infrared time-domain spectroscopy with terahertz beams of dielectrics and semiconductors. *J. Opt. Soc. Am. B*, 7(10):2006–2015, Oct 1990.

[88] X.-C. Zhang and D. H. Auston. Optoelectronic measurement of semiconductor surfaces and interfaces with femtosecond optics. *J. Appl. Phys.*, 71(1):326–338, 1992.

[89] P. Uhd Jepsen, R. H. Jacobsen, and S. R. Keiding. Generation and detection of terahertz pulses from biased semiconductor antennas. *J. Opt. Soc. Am. B*, 13(11):2424–2436, Nov 1996.

[90] A. Cingolani, M. Ferrara, and M. Lugar. Dispersion of the linear electrooptic coefficient and of the non-linear susceptibility in ZnTe. *Solid State Commun.*, 38(9):819 – 821, 1981.

[91] Yu Berozashvili, S Machavariani, A Natsvlishvili, and A Chirakadze. Dispersion of the linear electro-optic coefficients and the non-linear susceptibility in GaP. *J. Phys. D: Appl. Phys.*, 22(5):682, 1989.

[92] Q. Chen and X.-C. Zhang. Polarization modulation in optoelectronic generation and detection of terahertz beams. *Appl. Phys. Lett.*, 74(23):3435–3437, 1999.

[93] Paul C. M. Planken, Han-Kwang Nienhuys, Huib J. Bakker, and Tom Wenckebach. Measurement and calculation of the orientation dependence of terahertz pulse detection in ZnTe. *J. Opt. Soc. Am. B*, 18(3):313–317, Mar 2001.

[94] Q. Wu and X.-C. Zhang. 7 terahertz broadband GaP electro-optic sensor. *Appl. Phys. Lett.*, 70(14):1784–1786, April 1997.

[95] A. Leitenstorfer, S. Hunsche, J. Shah, M. C. Nuss, and W. H. Knox. Detectors and sources for ultrabroadband electro-optic sampling: Experiment and theory. *Appl. Phys. Lett.*, 74(11):1516–1518, 1999.

[96] C Kubler, R Huber, and A Leitenstorfer. Ultrabroadband terahertz pulses: generation and field-resolved detection. *Semicond. Sci. Technol.*, 20(7):S128–S133, 2005.

[97] Alexander Sell, Rdiger Scheu, Alfred Leitenstorfer, and Rupert Huber. Field-resolved detection of phase-locked infrared transients from a compact er:fiber system tunable between 55 and 107 THz. *Appl. Phys. Lett.*, 93(25):251107, 2008.

[98] M. R. Freeman, M. J. Brady, and J. Smyth. Extremely high frequency pulse magnetic resonance by picosecond magneto?optic sampling. *Appl. Phys. Lett.*, 60(20):2555–2557, 1992.

[99] J. A. Riordan, F. G. Sun, Z. G. Lu, and X.-C. Zhang. Free-space transient magneto-optic sampling. *Appl. Phys. Lett.*, 71(11):1452–1454, 1997.

[100] Jingle Liu, Jianming Dai, and X.-C. Zhang. Ultrafast broadband terahertz waveform measurement utilizing ultraviolet plasma photoemission. *J. Opt. Soc. Am. B*, 28(4):796–804, Apr 2011.

[101] Xiaofei Lu and X.-C. Zhang. Balanced terahertz wave air-biased-coherent-detection. *Appl. Phys. Lett.*, 98(15):151111, 2011.

[102] Jingle Liu and X.-C. Zhang. Terahertz-radiation-enhanced emission of fluorescence from gas plasma. *Phys. Rev. Lett.*, 103(23):235002, Dec 2009.

[103] Benjamin Clough, Jingle Liu, and X.-C. Zhang. Laser-induced photoacoustics influenced by single-cycle terahertz radiation. *Opt. Lett.*, 35(21):3544–3546, November 2010.

[104] David G. Cooke and Peter Uhd Jepsen. Time-resolved THz spectroscopy in a parallel plate waveguide. *Physica Status Solidi A*, 206(5):997–1000, 2009.

[105] Bradley Ferguson and Xi-Cheng Zhang. Materials for terahertz science and technology. *Nat. Mater.*, 1(1):26–33, September 2002.

[106] Daniel Mittleman, editor. *Sensing with terahertz radiation.* Springer, Berlin, 2003.

[107] H. Harde, Søren Keiding, and D. Grischkowsky. Thz commensurate echoes: Periodic rephasing of molecular transitions in free-induction decay. *Phys. Rev. Lett.*, 66(14):1834–1837, Apr 1991.

[108] D.M. Mittleman, R.H. Jacobsen, R. Neelamani, R.G. Baraniuk, and M.C. Nuss. Gas sensing using terahertz time-domain spectroscopy. *Appl. Phys. B: Lasers Opt.*, 67:379–390, 1998. 10.1007/s003400050520.

[109] L. Thrane, R.H. Jacobsen, P. Uhd Jepsen, and S.R. Keiding. THz reflection spectroscopy of liquid water. *Chem. Phys. Lett.*, 240(4):330 – 333, 1995.

[110] J. T. Kindt and C. A. Schmuttenmaer. Far-infrared dielectric properties of polar liquids probed by femtosecond terahertz pulse spectroscopy. *The Journal of Physical Chemistry*, 100(24):10373–10379, 1996.

[111] Uffe Møller, David G. Cooke, Koichiro Tanaka, and Peter Uhd Jepsen. Terahertz reflection spectroscopy of Debye relaxation in polar liquids. *J. Opt. Soc. Am. B*, 26(9):A113–A125, Sep 2009.

[112] Jie Shan, Feng Wang, Ernst Knoesel, Mischa Bonn, and Tony F. Heinz. Measurement of the frequency-dependent conductivity in sapphire. *Phys. Rev. Lett.*, 90(24):247401, Jun 2003.

[113] Hiroaki Yasuda and Iwao Hosako. Measurement of terahertz refractive index of metal with terahertz time-domain spectroscopy. *Jpn. J. Appl. Phys.*, 47(3):1632–1634, 2008.

[114] D. M. Mittleman, J. Cunningham, M. C. Nuss, and M. Geva. Noncontact semiconductor wafer characterization with the terahertz hall effect. *Appl. Phys. B: Lasers Opt.*, 71(1):16–18, 1997.

[115] Paul C. M. Planken, Martin C. Nuss, Igal Brener, Keith W. Goossen, Marie S. C. Luo, Shun Lien Chuang, and Loren Pfeiffer. Terahertz emission in single quantum wells after coherent optical excitation of light hole and heavy hole excitons. *Phys. Rev. Lett.*, 69(26):3800–3803, Dec 1992.

[116] Y. C. Shen, T. Lo, P. F. Taday, B. E. Cole, W. R. Tribe, and M. C. Kemp. Detection and identification of explosives using terahertz pulsed spectroscopic imaging. *Appl. Phys. Lett.*, 86(24):241116, 2005.

[117] Joseph S. Melinger, N. Laman, and D. Grischkowsky. The underlying terahertz vibrational spectrum of explosives solids. *Appl. Phys. Lett.*, 93(1):011102, 2008.

[118] Robert J. Foltynowicz, Ronald E. Allman, and Eric Zuckerman. Terahertz absorption measurement for gas-phase 2,4-dinitrotoluene from 0.05thz to 2.7THz. *Chem. Phys. Lett.*, 431(1-3):34 – 38, 2006.

[119] M. C. Nuss, D. H. Auston, and F. Capasso. Direct subpicosecond measurement of carrier mobility of photoexcited electrons in gallium arsenide. *Phys. Rev. Lett.*, 58(22):2355–2358, Jun 1987.

[120] D. G. Cooke, F. A. Hegmann, E. C. Young, and T. Tiedje. Electron mobility in dilute GaAs bismide and nitride alloys measured by time-resolved terahertz spectroscopy. *Appl. Phys. Lett.*, 89(12):122103, 2006.

[121] E. Hendry, M. Koeberg, J. Pijpers, and M. Bonn. Reduction of carrier mobility in semiconductors caused by charge-charge interactions. *Phys. Rev. B*, 75(23):233202, Jun 2007.

[122] O. Ostroverkhova, D. G. Cooke, S. Shcherbyna, R. F. Egerton, F. A. Hegmann, R. R. Tykwinski, and J. E. Anthony. Bandlike transport in pentacene and functionalized pentacene thin films revealed by subpicosecond transient photoconductivity measurements. *Phys. Rev. B*, 71(3):035204, Jan 2005.

[123] James T. Kindt and Charles A. Schmuttenmaer. Theory for determination of the low-frequency time-dependent response function in liquids using time-resolved terahertz pulse spectroscopy. *J. Chem. Phys.*, 110(17):8589–8596, 1999.

[124] J. F. Federici, B. I. Greene, P. N. Saeta, D. R. Dykaar, F. Sharifi, and R. C. Dynes. Direct picosecond measurement of photoinduced cooper-pair breaking in lead. *Phys. Rev. B*, 46(17):11153–11156, Nov 1992.

[125] Robert A. Kaindl, Marc A. Carnahan, Daniel S. Chemla, Seongshik Oh, and James N. Eckstein. Dynamics of cooper pair formation in $bi2sr2cacu2o8 + \delta$. *Phys. Rev. B*, 72(6):060510, Aug 2005.

[126] A. Dienst, M. C. Hoffmann, D. Fausti, J. C. Petersen, S. Pyon, T. Takayama, H. Takagi, and A. Cavalleri. Bi-directional ultrafast electric-field gating of interlayer charge transport in a cuprate superconductor. *Nat Photon*, 5(8):485–488, August 2011.

[127] Hakan Altan, Feng Huang, John F. Federici, Aidong Lan, and Haim Grebel. Optical and electronic characteristics of single walled carbon nanotubes and silicon nanoclusters by tetrahertz spectroscopy. *J. Appl. Phys.*, 96(11):6685–6689, 2004.

[128] Henrik Porte. *Time-resolved terahertz spectroscopy of semiconductor nanostructures*. PhD thesis, DTU, 2011.

[129] Matthew C. Beard, Gordon M. Turner, James E. Murphy, Olga I. Micic, Mark C. Hanna, Arthur J. Nozik, and Charles A. Schmuttenmaer. Electronic coupling in InP nanoparticle arrays. *Nano Lett.*, 3(12):1695–1699, 2003.

[130] D. Turchinovich, K. Pierz, and P. Uhd Jepsen. InAs/GaAs quantum dots as efficient free carrier deep traps. *physica status solidi (c)*, 0(5):1556–1559, 2003.

[131] R. P. Prasankumar, A. Scopatz, D. J. Hilton, A. J. Taylor, R. D. Averitt, J. M. Zide, and A. C. Gossard. Carrier dynamics in self-assembled ErAs nanoislands embedded in GaAs measured by optical-pump terahertz-probe spectroscopy. *Appl. Phys. Lett.*, 86(20):201107, 2005.

[132] Tae-In Jeon, Keun-Ju Kim, Chul Kang, Seung-Jae Oh, Joo-Hiuk Son, Kay Hyeok An, Dong Jae Bae, and Young Hee Lee. Terahertz conductivity of anisotropic single walled carbon nanotube films. *Appl. Phys. Lett.*, 80(18):3403–3405, 2002.

[133] David G. Cooke, Jun Y. Lek, Frederik C. Krebs, Yeng Ming Lam, and Peter Uhd Jepsen. Time-resolved terahertz spectroscopy of conjugated polymer/CdSe nanorod composites. *Proc. SPIE*, 7600(1):76000H, 2010.

[134] J. D. Wiley. *Semiconductor and Semimetals*. Academic Press, N.Y., 1975.

[135] M. Tinkham. Energy gap interpretation of experiments on infrared transmission through superconducting films. *Phys. Rev.*, 104(3):845–846, Nov 1956.

[136] Martin Dressel and George Gruner. *Electrodynamics of Solids*. Cambridge University Press, 2003.

[137] F A Hegmann and K P H Lui. *Optical pump - Terahertz probe investigation of carrier relaxation in radiation-damaged silicon-on-sapphire*, volume 4643, pages 31–41. 2002.

[138] Georgi L. Dakovski, Brian Kubera, Song Lan, and Jie Shan. Finite pump-beam-size effects in optical pump-terahertz probe spectroscopy. *J. Opt. Soc. Am. B*, 23(1):139–141, Jan 2006.

[139] Matthew C Beard, Gordon M Turner, and Charles A Schmuttenmaer. Subpicosecond carrier dynamics in low-temperature grown GaAs as measured by time-resolved terahertz spectroscopy. *J. Appl. Phys.*, 90(12):5915, 2001.

[140] Samuel P. Mickan, Kwang-Su Lee, Toh-Ming Lu, Jesper Munch, Derek Abbott, and X. C. Zhang. Double modulated differential THz-TDS for thin film dielectric characterization. *MICROELECTR. J.*, 33(12):1033 – 1042, 2002.

[141] Samuel Peter Mickan, Regina Shvartsman, Jesper Munch, Xi-Cheng Zhang, and Derek Abbott. Low noise laser-based T-ray spectroscopy of liquids using double-modulated differential time-domain spectroscopy. *J. OPT. B-QUANTUM S. O.*, 6(8):S786, 2004.

[142] Jegathisvaran Balakrishnan, Bernd M. Fischer, and Derek Abbott. Low noise spinning wheel technique for THz material parameter extraction. *Opt. Commun.*, 283(10):2301 – 2307, 2010.

[143] Jared H. Strait, Paul A. George, Mark Levendorf, Martin Blood-Forsythe, Farhan Rana, and Jiwoong Park. Measurements of the carrier dynamics and terahertz response of oriented germanium nanowires using optical-pump terahertz-probe spectroscopy. *Nano Lett.*, 9(8):2967–2972, 2009. PMID: 19594164.

[144] M. S. Tyagi and R. Van Overstraeten. Minority carrier recombination in heavily-doped silicon. *Solid-State Electron.*, 26(6):577 – 597, 1983.

[145] D. E. Aspnes and A. A. Studna. Dielectric functions and optical parameters of Si, Ge, GaP, GaAs, GaSb, InP, InAs, and InSb from 1.5 to 6.0 ev. *Phys. Rev. B*, 27(2):985, Jan 1983.

[146] Kenneth Levenberg. Method for the solution of certain non-linear problems in least-squares. *Quarterly of Applied Mathematics*, 2(2):164, 1944.

[147] Casper Larsen, David G. Cooke, and Peter Uhd Jepsen. Finite-difference time-domain analysis of time-resolved terahertz spectroscopy experiments. *J. Opt. Soc. Am. B*, 28(5):1308–1316, May 2011.

[148] D. Golde, M. Wagner, D. Stehr, H. Schneider, M. Helm, A. M. Andrews, T. Roch, G. Strasser, M. Kira, and S. W. Koch. Fano signatures in the intersubband terahertz response of optically excited semiconductor quantum wells. *Phys. Rev. Lett.*, 102(12):127403, Mar 2009.

[149] G. Gallot, S. P. Jamison, R. W. McGowan, and D. Grischkowsky. Terahertz waveguides. *J. Opt. Soc. Am. B*, 17(5):851–863, May 2000.

[150] R. Mendis and D. Grischkowsky. Undistorted guided-wave propagation of subpicosecond terahertz pulses. *Opt. Lett.*, 26(11):846–848, June 2001.

[151] Rajind Mendis and Daniel M. Mittleman. Comparison of the lowest-order transverse-electric (TE1) and transverse-magnetic (TEM) modes of the parallel-plate waveguide for terahertz pulse applications. *Opt. Express*, 17(17):14839–14850, August 2009.

[152] Rajind Mendis and Daniel M. Mittleman. An investigation of the lowest-order transverse-electric (TE1) mode of the parallel-plate waveguide for thz pulse propagation. *J. Opt. Soc. Am. B*, 26(9):A6–A13, September 2009.

[153] R. Mendis and D. Grischkowsky. THz interconnect with low-loss and low-group velocity dispersion. *Microwave and Wireless Components Letters, IEEE*, 11(11):444–446, 2001.

[154] Joseph S. Melinger, N. Laman, S. Sree Harsha, ShuFan Cheng, and D. Grischkowsky. High-resolution waveguide terahertz spectroscopy of partially oriented organic polycrystalline films. *The Journal of Physical Chemistry A*, 111(43):10977–10987, 2007.

[155] Mark I. Stockman. Nanofocusing of optical energy in tapered plasmonic waveguides. *Phys. Rev. Lett.*, 93(13):137404, Sep 2004.

[156] Anastasia Rusina, Maxim Durach, Keith A. Nelson, and Mark I. Stockman. Nanoconcentration of terahertz radiation in plasmonic waveguides. *Opt. Express*, 16(23):18576–18589, November 2008.

[157] Hui Zhan, Rajind Mendis, and Daniel M. Mittleman. Superfocusing terahertz waves below $\lambda/250$ using plasmonic parallel-plate waveguides. *Opt. Express*, 18(9):9643–9650, April 2010.

[158] Hui Zhan, Rajind Mendis, and Daniel M. Mittleman. Characterization of the terahertz near-field output of parallel-plate waveguides. *J. Opt. Soc. Am. B*, 28(3):558–566, March 2011.

[159] M. Schnell, P. Alonso-Gonzalez, L. Arzubiaga, F. Casanova, L. E. Hueso, A. Chuvilin, and R. Hillenbrand. Nanofocusing of mid-infrared energy with tapered transmission lines. *Nat Photon*, 5(5):283–287, MAY 2011.

[160] Jingbo Liu, Rajind Mendis, and Daniel M. Mittleman. The transition from a TEM-like mode to a plasmonic mode in parallel-plate waveguides. *Appl. Phys. Lett.*, 98(23):231113–3, June 2011.

[161] Rajind Mendis, Victoria Astley, Jingbo Liu, and Daniel M. Mittleman. Terahertz microfluidic sensor based on a parallel-plate waveguide resonant cavity. *Appl. Phys. Lett.*, 95(17):171113, 2009.

[162] Michael J Fitch and Robert Osiander. Terahertz waves for communications and sensing. *Most*, 25(4):348355, 2004.

[163] M. M. Awad and R. A. Cheville. Transmission terahertz waveguide-based imaging below the diffraction limit. *Appl. Phys. Lett.*, 86(22):221107, 2005.

[164] Kanglin Wang and Daniel M. Mittleman. Metal wires for terahertz wave guiding. *Nature*, 432(7015):376–379, November 2004.

[165] Hua Cao and Ajay Nahata. Coupling of terahertz pulses onto a single metal wire waveguide using milled grooves. *Opt. Express*, 13(18):7028–7034, Sep 2005.

[166] Victoria Astley, Rajind Mendis, and Daniel M. Mittleman. Characterization of terahertz field confinement at the end of a tapered metal wire waveguide. *Appl. Phys. Lett.*, 95(3):031104, 2009. journal article.

[167] Marx Mbonye, Rajind Mendis, and Daniel M. Mittleman. A terahertz two-wire waveguide with low bending loss. *Appl. Phys. Lett.*, 95(23):233506, 2009.

[168] R. W. McGowan, G. Gallot, and D. Grischkowsky. Propagation of ultrawideband short pulses of terahertz radiation through submillimeter-diameter circular waveguides. *Opt. Lett.*, 24(20):1431–1433, Oct 1999.

[169] Jen-Tang Lu, Yu-Chun Hsueh, Yu-Ru Huang, Yuh-Jing Hwang, and Chi-Kuang Sun. Bending loss of terahertz pipe waveguides. *Opt. Express*, 18(25):26332–26338, December 2010.

[170] Markus Wachter, Michael Nagel, and Heinrich Kurz. Metallic slit waveguide for dispersion-free low-loss terahertz signal transmission. *Appl. Phys. Lett.*, 90(6):061111, 2007.

[171] Tae-In Jeon and D. Grischkowsky. THz Zenneck surface wave (THz surface plasmon) propagation on a metal sheet. *Appl. Phys. Lett.*, 88(6):061113–3, February 2006.

[172] Mufei Gong, Tae-In Jeon, and D. Grischkowsky. THz surface wave collapse on coated metal surfaces. *Opt. Express*, 17(19):17088–17101, September 2009.

[173] S. P. Jamison, R. W. McGowan, and D. Grischkowsky. Single-mode waveguide propagation and reshaping of sub-ps terahertz pulses in sapphire fibers. *Appl. Phys. Lett.*, 76(15):1987–1989, 2000.

[174] H. Han, H. Park, M. Cho, and J. Kim. Terahertz pulse propagation in a plastic photonic crystal fiber. *Appl. Phys. Lett.*, 80(15):2634–2636, 2002.

[175] Masahiro Goto, Alex Quema, Hiroshi Takahashi, Shingo Ono, and Nobuhiko Sarukura. Teflon photonic crystal fiber as terahertz waveguide. *Jpn. J. Appl. Phys.*, 43(2B):L317–L319, 2004.

[176] Kristian Nielsen, Henrik K. Rasmussen, Peter Uhd Jepsen, and Ole Bang. Broadband terahertz fiber directional coupler. *Opt. Lett.*, 35(17):2879–2881, September 2010.

[177] Kristian Nielsen, Henrik K. Rasmussen, Peter Uhd Jepsen, and Ole Bang. Porous-core honeycomb bandgap THz fiber. *Opt. Lett.*, 36(5):666–668, Mar 2011.

[178] Maksim Skorobogatiy and Alexandre Dupuis. Ferroelectric all-polymer hollow Bragg fibers for terahertz guidance. *Appl. Phys. Lett.*, 90(11):113514, 2007.

[179] Shaghik Atakaramians, Shahraam Afshar V., Heike Ebendorff-Heidepriem, Michael Nagel, Bernd M. Fischer, Derek Abbott, and Tanya M. Monro. THz porous fibers: design, fabrication and experimental characterization. *Opt. Express*, 17(16):14053–15062, Aug 2009.

[180] R. Mendis and D. Grischkowsky. Plastic ribbon thz waveguides. *J. Appl. Phys.*, 88(7):4449–4451, 2000.

[181] Rajind Mendis. Nature of subpicosecond terahertz pulse propagation in practical dielectric-filled parallel-plate waveguides. *Opt. Lett.*, 31(17):2643–2645, Sep 2006.

[182] D. G. Cooke and P. U. Jepsen. Optical modulation of terahertz pulses in a parallel plate waveguide. *Opt. Express*, 16(19):15123–15129, Sep 2008.

[183] Rajind Mendis. THz transmission characteristics of dielectric-filled parallel-plate waveguides. *J. Appl. Phys.*, 101(8):083115, 2007.

[184] N. Marcuvitz. *Waveguide handbook*. Peregrinus, London, 1986.

[185] C.A. Balanis. *Advanced engineering electromagnetics*. Wiley, 1989.

[186] Xiaofei Lu, Nicholas Karpowicz, and X.-C. Zhang. Broadband terahertz detection with selected gases. *J. Opt. Soc. Am. B*, 26(9):A66–A73, Sep 2009.

[187] Raymond A. Serway. *Principles of Physics (2nd ed.)*. Saunders College, Fort Worth, Texas; London, 1998.

[188] S. Coleman and D. Grischkowsky. A THz transverse electromagnetic mode two-dimensional interconnect layer incorporating quasi-optics. *Appl. Phys. Lett.*, 83(18):3656–3658, 2003.

[189] S. Ramo, J. R. Whinnery, and T. V. Duzer. *Field and Waves in Communications, Third Edition*. Wiley, 1993.

[190] Rudiger Paschotta. *Encyclopedia of Laser Physics and Technology*. Wiley, 2008.

[191] R. A. Cheville and D. Grischkowsky. Time domain terahertz impulse ranging studies. *Appl. Phys. Lett.*, 67(14):1960–1962, 1995.

[192] R.A. Cheville, R.W. McGowan, and D.R. Grischkowsky. Late-time target response measured with terahertz impulse ranging. *Antennas and Propagation, IEEE Transactions on*, 45(10):1518–1524, oct 1997.

[193] X.J. Zhong, T.J. Cui, Z. Li, Y.B. Tao, and H. Lin. Terahertz-wave scattering by perfectly electrical conducting objects. *J. ELECTROMAGNET. WAVE.*, 21(15):2331–2340, 2007.

[194] Jeremy Pearce and Daniel M Mittleman. Scale model experimentation: using terahertz pulses to study light scattering. *Physics in Medicine and Biology*, 47(21):3823, 2002.

[195] Jeremy Pearce and Daniel M Mittleman. Using terahertz pulses to study light scattering. *Physica B: Condensed Matter*, 338(1-4):92 – 96, 2003. Proceedings of the Sixth International Conference on Electrical Transport and Optical Properties of Inhomogeneous Media.

[196] J. Waldman, H. R. Fetterman, P. E. Duffy, T. G. Bryant, and Tannenwald P. E. Submillimeter model measurements and their applications to millimeter radar systems. *Proceedings of the Fourth International Conference on Infrared and Near-Millimeter Waves*, pages 49 – 50, 1979.

[197] K. McClatchey, M. T. Reiten, and R. A. Cheville. Time resolved synthetic aperture terahertz impulse imaging. *Appl. Phys. Lett.*, 79(27):4485–4487, 2001.

[198] M. J. Coulombe, T. Horgan, J. Waldman, G. Szatkowski, and Nixon W. A 524 GHz polarimetric compact range for scale model rcs measurements. *Proc. Antenna Meas. Tech. Assoc.*, 1999.

[199] J. Waldman T. M. Goyette, J. C. Dickinson and W. E. Nixon. A 1.56 THz compact radar range for W-band imagery of scale-model tactical targets. *Proc. SPIE, Algorithms for Synthetic Aperture Radar Imagery VII*, 4053:615, 2000.

[200] Andriy A. Danylov, Thomas M. Goyette, Jerry Waldman, Michael J. Coulombe, Andrew J. Gatesman, Robert H. Giles, Xifeng Qian, Neelima Chandrayan, Shivashankar Vangala, Krongtip Termkoa, William D. Goodhue, and William E. Nixon. Terahertz inverse synthetic aperture radar (ISAR) imaging with a quantum cascade laser transmitter. *Opt. Express*, 18(15):16264–16272, Jul 2010.

[201] E. F. Knott. *Radar cross section measurements*. Van Nostrand Reinhold, New York, 1993.

[202] D. L. Mensa. *High resolution radar cross-section imaging*. Artech House, 1991.

[203] Gustav Mie. Beitrage zur optik truber medien, speziell kolloidaler metallosungen. *Annalen der Physik*, 330(3):377–445, 1908.

[204] M. Born and E. Wolf. *"Diffraction by a Conducting Sphere; Theory of Mie." Chapter 13.5 in Principles of Optics: Electromagnetic Theory of Propagation, Interference, and Diffraction of Light, 7th ed.* Cambridge University Press, Cambridge, England, 1999.

[205] Herman T. Gabor. *Fundamentals of Computerized Tomography.* Springer, 2nd edition, 2010.

[206] A. C. Kak and Malcolm Slaney. *Principles of Computerized Tomographic Imaging.* IEEE Press, 1988.

[207] Bradley Ferguson, Shaohong Wang, Doug Gray, Derek Abbot, and X.-C. Zhang. T-ray computed tomography. *Opt. Lett.*, 27(15):1312–1314, Aug 2002.

[208] Takashi Yasuda, Takeshi Yasui, Tsutomu Araki, and Emmanuel Abraham. Real-time two-dimensional terahertz tomography of moving objects. *Opt. Commun.*, 267(1):128–136, November 2006.

[209] A. Brahm, M. Kunz, S. Riehemann, G. Notni, and A. Tannermann. Volumetric spectral analysis of materials using terahertz-tomography techniques. *Appl. Phys. B: Lasers Opt.*, 100(1):151–158, 2010.

[210] S Wang and X-C Zhang. Pulsed terahertz tomography. *J. Phys. D: Appl. Phys.*, 37(4):R1, 2004.

[211] B. Recur, A. Younus, S. Salort, P. Mounaix, B. Chassagne, P. Desbarats, J.-P. Caumes, and E. Abraham. Investigation on reconstruction methods applied to 3D terahertz computed tomography. *Opt. Express*, 19(6):5105, March 2011.

[212] Jeremy Pearce, Hyeokho Choi, Daniel M. Mittleman, Jeff White, and David Zimdars. Terahertz wide aperture reflection tomography. *Opt. Lett.*, 30(13):1653–1655, July 2005.

[213] D. A. Bryan, Robert Gerson, and H. E. Tomaschke. Increased optical damage resistance in lithium niobate. *Appl. Phys. Lett.*, 44(9):847–849, 1984.

[214] Dmitry Turchinovich and Jaap I. Dijkhuis. Performance of combined ¡100¿-¡110¿ ZnTe crystals in an amplified THz time-domain spectrometer. *Opt. Commun.*, 270(1):96 – 99, 2007.

[215] Guozhong Zhao, Maarten ter Mors, Tom Wenckebach, and Paul C. M. Planken. Terahertz dielectric properties of polystyrene foam. *J. Opt. Soc. Am. B*, 19(6):1476–1479, Jun 2002.

[216] R. Bracewell. *The Hilbert Transform The Fourier Transform and its Applications, 3rd ed.* McGrawHill, 1999.

[217] Viktor G Veselago. The electrodynamics of substances with simultaneously negative values of ϵ and μ. *Soviet Physics Uspekhi*, 10(4):509, 1968.

[218] J. B. Pendry. Negative refraction makes a perfect lens. *Phys. Rev. Lett.*, 85:3966–3969, Oct 2000.

[219] Nicholas Fang, Hyesog Lee, Cheng Sun, and Xiang Zhang. Subdiffraction-limited optical imaging with a silver superlens. *Science*, 308(5721):534–537, 2005.

[220] D. Schurig, J. J. Mock, B. J. Justice, S. A. Cummer, J. B. Pendry, A. F. Starr, and D. R. Smith. Metamaterial electromagnetic cloak at microwave frequencies. *Science*, 314(5801):977–980, 2006.

[221] W. J. Padilla, M. T. Aronsson, C. Highstrete, Mark Lee, A. J. Taylor, and R. D. Averitt. Electrically resonant terahertz metamaterials: Theoretical and experimental investigations. *Phys. Rev. B*, 75:041102, Jan 2007.

[222] R. D. Averitt, W. J. Padilla, H. T. Chen, J. F. O'Hara, A. J. Taylor, C. Highstrete, M. Lee, J. M. O. Zide, S. R. Bank, and A. C. Gossard. Terahertz metamaterial devices. *Proceedings of SPIE*, 6772(1):677209, 2007.

[223] Hou-Tong Chen, John F. O'Hara, Antoinette J. Taylor, Richard D. Averitt, Clark Highstrete, Mark Lee, and Willie J. Padilla. Complementary planar terahertz metamaterials. *Opt. Express*, 15(3):1084–1095, Feb 2007.

[224] Hou-Tong Chen, John F. O'Hara, Abul K. Azad, Antoinette J. Taylor, Richard D. Averitt, David B. Shrekenhamer, and Willie J. Padilla. Experimental demonstration of frequency-agile terahertz metamaterials. *Nat Photon*, 2(5):295–298, May 2008.

[225] N. I. Landy, S. Sajuyigbe, J. J. Mock, D. R. Smith, and W. J. Padilla. Perfect metamaterial absorber. *Phys. Rev. Lett.*, 100:207402, May 2008.

[226] Hu Tao, Nathan I. Landy, Christopher M. Bingham, Xin Zhang, Richard D. Averitt, and Willie J. Padilla. A metamaterial absorber for the terahertz regime: design, fabrication and characterization. *Opt. Express*, 16(10):7181–7188, May 2008.

[227] Hu Tao, A C Strikwerda, K Fan, C M Bingham, W J Padilla, Xin Zhang, and R D Averitt. Terahertz metamaterials on free-standing highly-flexible polyimide substrates. *J. Phys. D: Appl. Phys.*, 41(23):232004, 2008.

[228] ShengXi Li, ZhenYu Yang, Jing Wang, and Ming Zhao. Broadband terahertz circular polarizers with single- and double-helical array metamaterials. *J. Opt. Soc. Am. A*, 28(1):19–23, Jan 2011.

[229] W. J. Padilla, A. J. Taylor, C. Highstrete, Mark Lee, and R. D. Averitt. Dynamical electric and magnetic metamaterial response at terahertz frequencies. *Phys. Rev. Lett.*, 96:107401, Mar 2006.

[230] Hou-Tong Chen, Willie J. Padilla, Joshua M. O. Zide, Arthur C. Gossard, Antoinette J. Taylor, and Richard D. Averitt. Active terahertz metamaterial devices. *Nature*, 444(7119):597–600, November 2006.

[231] Hou-Tong Chen, Willie J. Padilla, Joshua M. O. Zide, Seth R. Bank, Arthur C. Gossard, Antoinette J. Taylor, and Richard D. Averitt. Ultrafast optical switching of terahertz metamaterials fabricated on eras/gaas nanoisland superlattices. *Opt. Lett.*, 32(12):1620–1622, Jun 2007.

[232] John F. O'Hara, Ranjan Singh, Igal Brener, Evgenya Smirnova, Jiaguang Han, Antoinette J. Taylor, and Weili Zhang. Thin-film sensing with planar terahertz metamaterials: sensitivity and limitations. *Opt. Express*, 16(3):1786–1795, Feb 2008.

[233] Hu Tao, C. M. Bingham, A. C. Strikwerda, D. Pilon, D. Shrekenhamer, N. I. Landy, K. Fan, X. Zhang, W. J. Padilla, and R. D. Averitt. Highly flexible wide angle of incidence terahertz metamaterial absorber: Design, fabrication, and characterization. *Phys. Rev. B*, 78:241103, Dec 2008.

[234] Frank Baumann, Jr. William A. Bailey, Ahmer Naweed, William D. Goodhue, and Andrew J. Gatesman. Wet-etch optimization of free-standing terahertz frequency-selective structures. *Opt. Lett.*, 28(11):938–940, Jun 2003.

[235] D.J. Shelton, J.W. Cleary, J.C. Ginn, S.L. Wadsworth, R.E. Peale, D.K. Kotter, and G.D. Boreman. Gangbuster frequency selective surface metamaterials in terahertz band. *Electronics Letters*, 44(22):1288 –1289, 23 2008.

[236] M. A. Ordal, L. L. Long, R. J. Bell, S. E. Bell, R. R. Bell, Jr. R. W. Alexander, and C. A. Ward. Optical properties of the metals Al, Co, Cu, Au, Fe, Pb, Ni, Pd, Pt, Ag, Ti, and W in the infrared and far infrared. *Appl. Opt.*, 22(7):1099–1119, Apr 1983.

[237] AbulK. Azad and Weili Zhang. Resonant terahertz transmission in subwavelength metallic hole arrays of sub-skin-depth thickness. *Opt. Lett.*, 30(21):2945–2947, Nov 2005.

[238] Ranjan Singh, Carsten Rockstuhl, Falk Lederer, and Weili Zhang. The impact of nearest neighbor interaction on the resonances in terahertz metamaterials. *Appl. Phys. Lett.*, 94(2):021116, 2009.

[239] Qi-Ye Wen, Huai-Wu Zhang, Yun-Song Xie, Qing-Hui Yang, and Ying-Li Liu. Dual band terahertz metamaterial absorber: Design, fabrication, and characterization. *Appl. Phys. Lett.*, 95(24):241111, 2009.

[240] Hu Tao, C M Bingham, D Pilon, Kebin Fan, A C Strikwerda, D Shrekenhamer, W J Padilla, Xin Zhang, and R D Averitt. A dual band terahertz metamaterial absorber. *J. Phys. D: Appl. Phys.*, 43(22):225102, 2010.

[241] H. Wen, M. Wiczer, and A. M. Lindenberg. Ultrafast electron cascades in semiconductors driven by intense femtosecond terahertz pulses. *Phys. Rev. B*, 78:125203, Sep 2008.

[242] Matthias C. Hoffmann, János Hebling, Harold Y. Hwang, Ka-Lo Yeh, and Keith A. Nelson. THz-pump/THz-probe spectroscopy of semiconductors at high field strengths. *J. Opt. Soc. Am. B*, 26(9):A29–A34, Sep 2009.

[243] I-Chen Ho and X.-C. Zhang. Driving intervalley scattering and impact ionization in inas with intense terahertz pulses. *Appl. Phys. Lett.*, 98(24):241908, 2011.

[244] Kenan Gundogdu, Katherine W. Stone, Daniel B. Turner, and Keith A. Nelson. Multidimensional coherent spectroscopy made easy. *Chem. Phys.*, 341(1-3):89 – 94, 2007. Ultrafast Dynamics of Molecules in the Condensed Phase: Photon Echoes and Coupled Excitations - A Tribute to Douwe A. Wiersma.

[245] Paul A. Tipler and Ralph A. Llewellyn. *Modern Physics, 3rd Ed.* W.H. Freeman, 1999.

ISBN: 978-87-93089-23-5

Published by:
DTU Fotonik
Department of Photonic Engineering
Technical University of Denmark
Ørsteds Plads, building 343
DK-2800 Kgs. Lyngby

Krzysztof Iwaszczuk was born in Bialystok, Poland in 1984. He graduated from the I Liceum Ogolnoksztalcace im. Adama Mickiewicza w Bialymstoku in 2003. In July 2008 he received title of Master of Science in Engineering in applied physics at the Warsaw University of Technology and in December 2008 he defended Bachelor of Science degree in the field of mathematics at Warsaw University of Technology. In 2011 he received Ph.D. degree from Technical University of Denmark for thesis titled "Terahertz Technology for Defense and Security-Related Applications".

Krzysztof Iwaszczuk won a bronze medal in the International Physics Olympiad, Taipei, Taiwan, 2003. During his studies he was a recipient of several prizes and scholarships (Ministry of Education Scholarship, Kanton Scholarship, M. Krol prize, and other). His research interests include ultrafast optics, optoelectronics, terahertz technology, optical sensing and solid state physics.

After graduation Krzysztof Iwaszczuk is going to continue his scientific journey as a postdoc researcher at Technical University of Denmark.